Structural and Biochemical Characterization of Proteins Relevant to Human Disease

by

Ryan Boyd

A Dissertation Presented in Partial Fulfillment
of the Requirements for the Degree
Doctor of Philosophy

Approved October 2021 by the
Graduate Supervisory Committee:

Petra Fromme, Chair
Po-Lin Chiu
Wei Liu

ARIZONA STATE UNIVERSITY

December 2021

ABSTRACT

This work comprises a cumulative effort to provide analysis of proteins relevant to understanding and treating human disease. This dissertation focuses on two main protein complexes: the structure of the Chimp adenovirus Y25 capsid assembly, as used in the SARS-CoV-2 vaccine, Vaxzveria, and the Dbl family RhoGEF (guanosine exchange factor) Syx and its associated small G protein, RhoA. The course of research was influenced heavily by the onset of the Covid-19 pandemic and associated lockdown, which pushed anyone with the means to do meaningful research to shift priorities towards addressing the greatest public health crisis since the 1918 flu pandemic.

Analysis of the Syx-RhoA complex for the purposes of structurally guided drug design was initially the focus of heavy optimization efforts to overcome the numerous challenges associated with expression, purification, and handling of this protein. By analyzing *E. Coli* derived protein new important knowledge was gained about this protein's biophysical characteristics which contribute to its behavior and may inform drug design efforts. Expression in SF9 insect cells resulted in promising conditions for production of homogeneous and monodispersed protein. Homology modeling and molecular dynamics simulation of this protein support hypotheses about its interactions with both RhoA as well as regions of the cytoplasmic leaflet of the cell membrane.

Structural characterization of ChAdOx1, the adenoviral vector used in the AstraZeneca Covid-19 vaccine, Vaxzveria resulted in the highest resolution adenovirus structure ever solved (3.07Å). Subsequent biochemical analysis and computational simulations of PF4 with the ChAdOx1 capsid reveal interactions with important implications for vaccine induced thrombocytic throbocytopenia syndrome, a disorder observed in approximately 0.000024% of patients who receive Vaxzveria.

DEDICATION

I dedicate this work to my family. I could never hope to count the ways you have loved and supported me throughout my life up to this point. I would have never made it without you.

Mom; your intelligence and love have inspired me to be the best version of myself and carried me through the hardest moments. Over and over you have reminded me that I am loved and valued even when I can't see it for myself.

Dad; You are the best role model I could ever hope for. The devotion and warmth you have always shown in loving and providing for our family is something that I will always strive for. I hope I can live up to your incredible work ethic and endless love for us all.

Justin; having a brother like you has always inspired me to push myself to new heights and at the same time reminded me to find the joy in daily life in ways that I often neglect. Thank you for all of the times you have reminded me to stop and smell the roses.

Thank you all so much for being there for me every step of the way and helping me get back up, over and over again, when I stumble.

Megumi and Nattö Satkowski; Your love and support defined the best parts of my time in Arizona. Some of the happiest moments I have ever known have been the three of us together and I will always carry those warm memories with me, wherever I go.

ACKNOWLEDGMENTS

First, I would like to acknowledge my advisor Dr. Petra Fromme for always having an infectious passion for discovery and a vast depth of knowledge in the field of crystallography and membrane proteins that always helped me find a path forward, even when nothing was working. She has taught me that a successful structural biologist is more about coming to work every day with a smile and an exciting new idea then it is about getting things right the first time. The support of her lab members, especially Debra Hansen, Jim Zook, Nirupa Nagaratnam, and Bobby Baravati always helped keep me moving forward.

I would especially like to express gratitude to Tien Olson, the one quietly acting behind the scenes in the Fromme lab to keep things running smoothly. She was an unbeatable mentor for all of the hands-on things. Her extensive experience with all of the details that people often forget about in the lab sometimes goes unappreciated, but I always knew that if I re-ran my failed experiments with her buffers, 9 times out of 10, things would start working again.

I would also like to acknowledge DeWight Williams, who had patience beyond all reason as he did his best to teach me the ins and outs of Cryo-EM despite it not being his job to advise students. He was there with me in the weeds day in and day out as I sloughed my way towards a functional understanding of how to use an electron microscope. I will always appreciate his advice and commentary on the field of Cryo-EM and on life working in science.

I am extremely grateful to my committee member Po-Lin Chiu for giving me a world class education in the theory and practical aspects of single particle analysis and fielding my endless questions and for letting me take up a truly unreasonable amount of time and space on his computers.

My deepest gratitude to Abhisheck Singharoy for his endless energy and his lab

members, especially John Vant as well as Chitrak Gupta, Eric Wilson, and Jon Nguyen for their patience helping me run molecular dynamics simulations, figure out errors, and for discussing my crazy ideas with me.

I would like to acknowledge Chris Gisriel for taking me under his wing and helping me grow as a crystallographer and scientist when I needed mentorship, and for getting me involved in exciting new projects. His attitude towards leadership and getting things done is something that I always hope to emulate.

Thank you to Alex Baker for being someone equally passionate about science that I can always share my ideas with, and for giving me the opportunity to be a co-author with you on a project that I feel extremely lucky to be a part of. I hope we get the opportunity to prove that we are not crackpots someday.

Thank you to Daniel Friedman and Kara Brugman for endless intellectual discussions and for your edits and kind words when I needed them most.

Finally, thank you to the rest of the Fromme lab for making our lab an entertaining place to work and grow as a scientist.

TABLE OF CONTENTS

CHAPTER Page

CHAPTER Page

CHAPTER Page

CHAPTER Page

LIST OF TABLES

LIST OF FIGURES

Figure Page

Figure Page

Figure Page

Chapter 1

INTRODUCTION AND SIGNIFICANCE

1.1 Background of the Adenovirus Vaccine Vector ChAdOx1

1.1.1 Adenovirus Background and Its Use as a Vaccine Vector

Adenovirus vaccine vectors utilize the same core technology as gene therapy vectors to express transgenes, however their own inherent immunogenicity and tendency for liver tropism when delivered intravenously rendered them less favorable as gene therapy vectors. This same immunogenicity is an advantage for immune stimulating applications like vaccination and immuno-oncology applications. The earliest vaccines were simple attenuated pathogens or proteins derived from pathogens that were introduced into the host to promote an immune response. However quite frequently proteins which may be used in a vaccine to stimulate a neutralizing immune response are difficult to produce or are unstable in formulations suitable for clinical use. In addition, when used in vaccination, proteins may have highly variable immunogenicity and therefore require extensive testing to prove that they are both safe and efficacious. Adenovirus vectors have a significant advantage as, due to their double stranded DNA genome and non-enveloped capsid, they are extremely stable and therefore overcome formulation shortcomings that typically hamper other vaccination strategies like delicate proteins. The viruses ability to remain stable in the environment until they infect the host's cells, where they "hijack" host ribosomes to produce the proteins contained in their genome avoids issues commonly seen with protein production. In addition, all steps of vaccine development with this method are predictable and tractable in a short time frame. Adenoviral particles carrying the gene for an immunologically active protein are straightforward to produce because

adenoviruses are extremely well studied; their behavior and safety profile in humans has been established and manipulation of their genomes is relatively simple compared to other vector platforms. There are also established methods of mass production approved by regulatory authorities like the FDA. These advantages have led to their widespread use as vaccine vectors, especially in circumstances where their rapid development time and proven safety track record is an advantage, such as during an outbreak response [1–5].

1.1.2 Adenovirus Structure

Adenoviruses (Ads) consists of a liniar double stranded genome approximately 35kb long and codes for approximately 38 proteins depending on the species of adenovirus [6]. The genome is separated into early transcription units E1A, E1B, E2A, E2B, E3, and E4 (Figure 1.2); which are transcribed into mRNA and proteins early in the viral replication cycle to modulate viral DNA production and host immune response, and late transcription units L1-L5, which share the same promoter sequence and are transcribed later in the viral reproductive cycle [6–8]. Late transcription units code for proteins involved in viral capsid assembly. The genome is contained within an icosahedral capsid consisting of 3 major proteins; the hexon, the penton, and the fiber, as well as 4 other proteins (Figure 1.1). The hexon makes up the majority of the capsid which contains 120 hexon trimers arranged in 20 facets of the icosahedron. The outermost portion of the hexon is made up of loops projecting outwards from the capsid, dubbed the hyper variable region (HVR), which vary greatly from species to species. The penton protein is a pentameric protein residing at the 12 vertices of the icosahedral capsid(Figure 1.1). The penton acts as a base for the N-terminus fiber protein which consists of a long trimeric protein shaft, with different virus types containing variable numbers of pseudo repeats projecting out on the five-fold symmetry axis of the icosahedral capsid. This fiber shaft is flexible and terminates in the globular fiber knob domain at its outermost C-terminal end. The knob domain consists of a β-barrel consisting

of 10 strands with variable loops between each strand (Figure 1.1) [9, 10].

Minor coat proteins include pIIIa, pVI, pVIII, and pIX. Proteins pIIIa and pVII weave in between the spaces between hexons and pentons, towards the internal base of these major capsid proteins to stabilize the interactions holding together the capsid. Protein VI also resides on the interior face of the capsid and is involved in capsid endosomal escape and capsid processing. Protein IX has 240 copies per capsid arranged in a triskelion formation on the capsid exterior to, presumably to further stabilize the capsid [9].

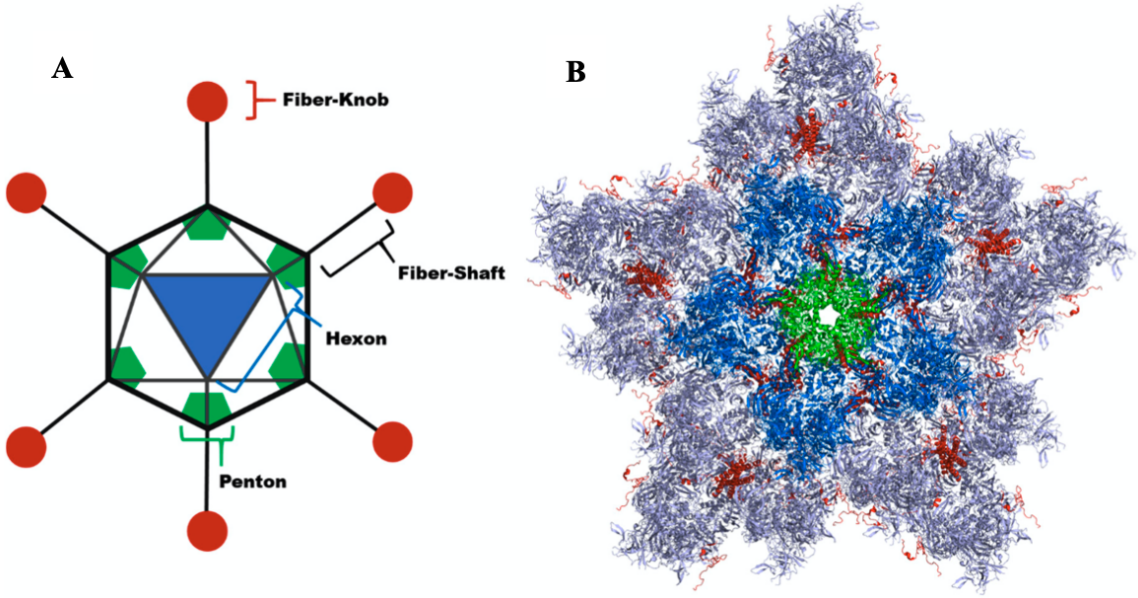

Figure 1.1: (A) Cartoon view of adenovirus, highlighting the major capsid proteins as labelled. (B) Structural view of an adenovirus vertex modelled from CryoEM structure (PDB: 6B1T) showing penton (green) with hexons (dark and light blue) and minor capsid proteins (red) [10].

1.1.3 Adenoviruses as Non-replicating Vaccine Vectors

A typical protocol for creating an adenoviral vaccine vector involves relatively simple genetic manipulation of the virus to remove the E1A and E3 protein in order to create a replication incompetent virus(Figure 1.2). The E1 gene is then introduced into the genome

of the cell line that the virus will be grown in to allow for replication. Then a transgene such as an immunologically active protein may be inserted into the E1 position, to be expressed when the replication incompetent virus infects the host cells. While advances on this basic protocol exist, such as E2/E4 deletions and ”gutless” vectors which contain almost no original adenovirus genetic material at all and can fit large 36 kb transgenes, these are outside the scope of this dissertation [1, 11].

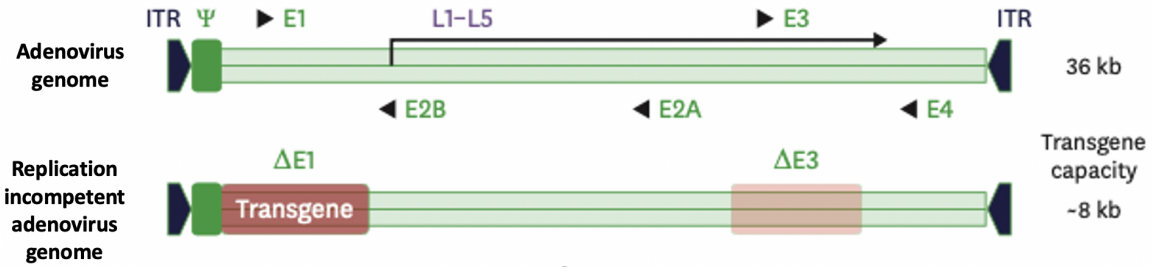

Figure 1.2: The adenovirus genome contains transcription units E1A, E1B, E2A, E2B, E3, and E4 that get transcribed early in the virus infection cycle. Genome modification by removal of the E1 and E3 site produces a replication incompetent virus that may reproduce only in cells engineered to express the E1 genes. The E1 site may also be used to introduce transgene payloads such as the SARS-CoV-2 spike protein [1].

1.1.4 Adenovirus Species Diversity and Revalence of Neutralizing Immunity Towards Adenoviral Vectors

More than 88 types of adenoviruses which infect humans exist, subdivided into species A through G [12]. Among these, several species may cause human disease and most may be opportunistic pathogens(Table 1.1) [13, 14]. Most adenovirus infections do not require medical intervention as they are neutralized by the host immune system.

The canonical infection process for most adenoviruses typically starts with respiratory or fecal-oral transmission, and is initiated through the adenovirus fiber knob binding to the coxsackie-adenovirus receptor (CAR), which is found broadly on epithelial and endothelial cells. However it should also be noted that species B1 adenoviruses bind

Group	Type	Associated Disease or Infection
A	12, 18, 31, 61	gastrointestinal, respiratory, urinary, cryptic enteric infection, linked to obesity, meningoencephalitis
B	**3**, **7**, 11, **14**, 16, 21, 34, 35, 50, **55**, 66	conjunctivitis, gastrointestinal, respiratory, urinary, pneumonia, meningoencephalitis, cystitis
C	1, **2**, 5, 6, 57	respiratory, gastrointestinal, obesity, pneumonia, hepatitis
D	**8**–10, 13, 15, 17, 19, 20, 22–30, 32, 33, 36–39, 42–49, 51, **53**, 54, **56**, 58-60, 63-67	conjunctivitis, gastrointestinal, respiratory disease, linked to obesity, meningoencephalitis
E	**4**	conjunctivitis, respiratory, pneumonia
F	40, 41	gastrointestinal, infantile diarrhea
G	52	gastrointestinal

Table 1.1: Human adenoviruses are is classified into seven groups (A–F). There are more than 88 types, and approximately 67 types (1–67) are known to be pathogenic in humans. Types 2, 3, 4, 7, 8, 14, 53, 55 and 56 are the most commonly linked to outbreaks and instances of hospitalization (shown in bold). [13–20]

CD46 in liu of CAR, and species B2 adenoviruses bind Desmoglin, while species D adenoviruses are capable of binding both sialic acid and CAR [21–28]. Initial fiber knob binding starts the internalization process and simultaneously brings the virus within range of integrins that can then bind the adenovirus RGD motif on the penton protein and trigger endocytosis via clatherin-coated vessicles(Figure 1.3, steps 1-6) [29]. As vessicles containing viral particles are moved into the endosomal system the fiber and penton proteins are shed from the virion and the penton-integrin interaction triggers activation of PI3 kinase and Rab GTPases to facilitate mechanisms of endosomal internalization and trafficking [30–32]. At the same time, the virus is recognized by several pathogen-associated molecular pattern (PAMP) receptors and mucosal-associated-invariant T (MAIT) cells which likely contribute to immunological activation that may support the formation of long lasting immunological memory.

Critically, the presence of unmethylated CG base pairs in double stranded DNA(CpG) are detected by cytoplasmic DNA sensor cyclic GMP-AMP synthase (cGAS) and toll-like receptor 9 (TLR9) and induce potent proinflamitory cytokines and interferons like IFN-γ. To counteract this, the essential adenoviral E1A protein binds to stimulator of interferon genes (STING) and inhibits DNA sensing to facilitate infection and virus replication [33–38]. This immunological activation is an advantage of adenovirus vaccine vectors over protein based vaccination methods because many pathogen surface proteins have evolved to have the lowest immunological signature possible and therefore require enhancement through adjuvants or other forms of immune stimulation, while a virus vaccine may stimulate the immune system without any adjuvant.

In the endosome, after the penton and fiber have been shed, exposing protein pVI, the ampiphalic helix of protein PVI disrupts the endosomal membrane and allows the virus to enter the cytosol(Figure 1.3, steps 7-8) [39–45]. Upon entering the cytosol, virion hexons are readily bound by dynein subunits of the dynein-dynactin microtubule motor complexs and transported towards the centrosome and the nucleus (Figure 1.3, steps 8-9) [46–53]. When the virion reaches the nuclear pore complex (NPC) it interacts with NPC proteins Crm1, Nup214, and Nup358; and recruits uncoating motor kinesin-1 (Kif5C) [54]. The combined interactions with NPC proteins, Kif5C, and the microtubules of the cytoskeleton exert a pulling force on the capsid that ruptures the capsid and releases the adenovirus genome which is still bound by several hundered adenovirus pVII proteins(Figure 1.3, steps 10-11). Nuclear transport receptors such as Imp7 and histone H1 bind the pVII proteins and shuttle the adenovirus genome through nuclear pore protein Nup62 and into nucleus where transcription and translation of the viral genome can begin [55–57].

Moreover, because of the presence of endemic adenovirus infections occurring in human populations, quite often people have developed cross-reactive immune responses against human adenoviruses which may neutralize a broad spectrum of adenovirus

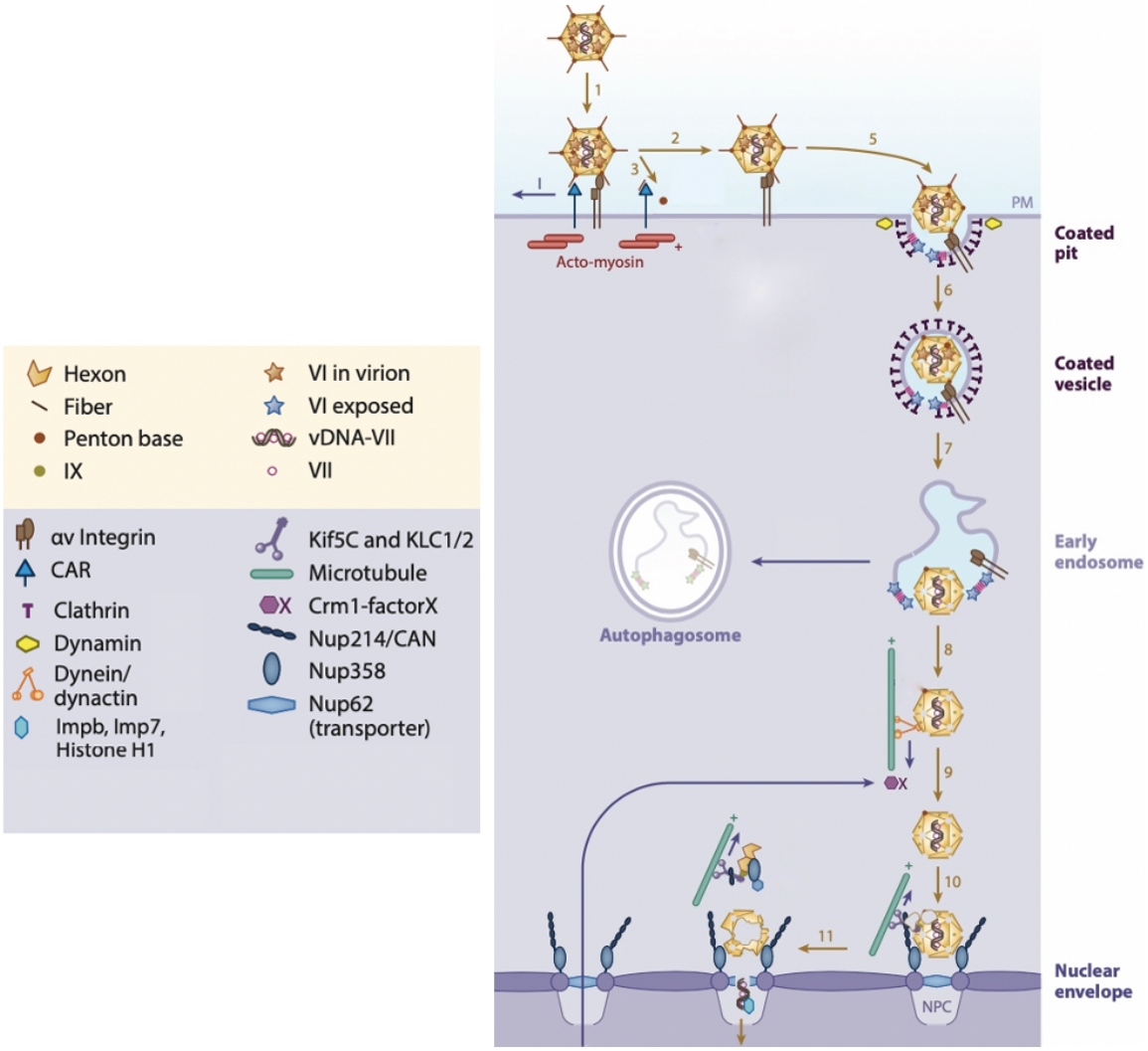

Figure 1.3: The cycle begins when adenovirus fiber knob protein interacts with the CAR receptor, placing the penton RGD loop in range of integrin(1). Integrin interactions stimulate viral entry into clathrin coated pits(5) which are trafficked to erly endosomes(6). Removal of the penton exposes protein pVI, which penetrates the membrane of the vessicle and facilitated viral escape(7). The capsid hexon protein is bound by dynein and trafficked along microtubules to the nucleus of the cell(8). Interactions with various nuclear pore complex proteins facilitate capsid release from microtubules and interaction with the nuclear pore(9-10). The capsid is physically ruptured and the virus genome is pulled through the nulear pore and into the nucleus(11) where genome transcription begins [58].

subspecies. Among the 88 adenovirus types, infection with one adenovirus type will generate antibodies which neutralize several other closely related types. In the case of

Ad5 and Ad26, some of the more commonly used human adenoviral vectors, multiple studies have shown seroprevalence of neutralizing antibodies to be present in human populations at high levels. In the case of Ad5, select populations have been measured with nearly 90% positive neutralizing antibodies against this vector with about 50% prevalence of neutralizing antibodies in western populations [59–63].

Multiple clinical trials and mechanistic studies have shown that the presence of neutralizing antibodies in host sera can nullify an adenovirus's therapeutic value [64]. Most neutralizing antibodies against adenovirus bind to the hyper variable regions (HVR) of the hexon protein [65], and experimentally mutations or chimeras which affect this region have been shown to improve transfection and vaccination characteristics [66]. These data can be misleading because populations in different geographic locations have very different levels of pre-existing immunity against endemic serotypes, and clinical trials using vectors such as Ad5 may show successful results in one location but not in another due to differences in local exposure to that serotype of adenovirus. In addition, adenovirus specific T cells and activated NK cells contribute to the immune response against adenoviruses that infect humans. It is important to note that because T cell and NK cell responses were historically not experimentally quantified when characterizing vaccine responses, and these responses occur in conjunction with the production of neutralizing antibodies, neutralizing antibody responses are often used as a proxy for total neutralizing immune response.

The consequence of this effect has been observed on a massive scale during the SARS-CoV-2 pandemic, as several commonly used human adenovirus strains such as adenovirus 5 (Ad5) and adenovirus 26 (Ad26) are currently also being employed as vaccine vectors against Covid-19 with varying degrees of success [67–70]. It shouls be noted that while Ad26 has a relatively low seroprevalence and therefore has shown acceptable efficacy in clinical trials [68], vaccination strategies which make use of Ad5 based platforms have been

criticized for their low efficacy, suggesting that the higher seroprevalence of neutralizing antibodies against Ad5 may be contributing to these poor results [63, 67].

1.1.5 ChAdOx1 Is a Simian Adenovirus with Low Human Seroprevalence

ChAdOx1 is a non-replicating adenoviral vaccine vector developed from Chimpanzee adenovirus Y25 by the Jenner Institute at Oxford and was promoted as a vector for rapid vaccine development in the case of an epidemic [2, 71, 72]. While there is debate over definitions of species type outside of human adenoviruses, ChAdOx most resembles a species E adenovirus. The viral vector was engineered by λ red recombineering with galactokinase selection to manipulate a bacterial artifical chromasome containing Y25 viral genome [73]. The E1 and E3 regions of the viral genome were removed and the E1 site was replaced by a attR1 attR2 Gateway cassette containing the galactokinase selection gene. Replication incompetent adenoviruses rely on the E1 genes being expressed by their host cells for replication and therefore can not replicate outside of host cell lines engineered to express the E1A gene products. Additionally, it was found that the Y25 did not have a favorable growth rate and yeild in HEK293A cells. This is because HEK293A cells were generated to express E1 gene products derived from Ad5. Open reading frames(ORF) orf3, orf4, orf6, and orf6/7 from the E4 region of the Y25 chimpanzee virus produce proteins that do not interact as strongly with Ad5 E1 proteins E1A and E1B 55K. E1B and E4orf6 protein form a complex that binds and degrades host cell p53 proteins, blocking p53 mediated apoptosis of the infected cell, therefore efficient interaction is essential for viral replication. To remedy the lack of E4orf6 binding in HEK-293 cells expressing Ad5 E1 genes, the E4 region of the Y25 virus was swapped out with the E4 region of Ad5 to improve growth and yeild when being grown in HEK293 cell lines [11, 71].

The primary reason this virus was selected as a vaccine platform was because of very

low pre-existing immune seroprevalence to chimpanzee adenoviruses. Multiple studies have compared the seroprevalence of common vaccine platforms Ad5 and Ad26 with several simian adenoviruses including Y25 and found almost no seroprevalence of neutralizing antibodies against simian adenoviruses in the human population [71, 74, 75]. Because of this low immune seroprevalence, and because this virus binds the CAR receptor which is nearly completely homologous between humans and Chimpanzees, Y25 was an ideal candidate to develop into a vaccine platform which circumvents issues seen in clinical trials with human adenoviruses that are neutralized by cross-reactive antibodies from past adenovirus infections.

1.1.6 The Onset of the SARS-CoV-2 Pandemic Prompted ChAdOx1 Adoption as a Leading Covid-19 Vaccine Candidate

The global impact of SARS-CoV-2 can not be overstated. Since its first detection in December 2019, 239 million Covid-19 cases have resulted in 4.88 million deaths worldwide as of October 2021, along with massive economic impacts influencing nearly every person on earth [76, 77]. Before the Covid-19 pandemic, ChAdOx1 had already shown promise in several clinical trials against a variety of emerging pathogens [1, 2, 11]. Most significantly, the platform had demonstrated efficacy and safety as a MERS vaccine. The vector, expressing the MERS spike protein as a transgene, had shown safety in phase I clinical trials and effectiveness in producing neutralizing protection against MERS infection in non human primates [78]. Because of this, with the onset of the Covid-19 pandemic, the ChAdOx1 vector was quickly adapted for use with the SARS-CoV-2 spike protein in place of the MERS spike protein transgene. After successful clinical trials, over 3 billion doses of the vaccine have been ordered, far more than any other vaccine, with 318.9 million doses administered as of Febuary 2021 through the COVAX (COVID-19 Vaccines Global Access) program to countries in need (Figure 1.4). This accounts for

more than 99% of all of the doses distributed by COVAX around the world thus far [79]. Despite this massive investment in development, its receptor tropism and structure of critical domains which determine host-virus interaction had not been published.

1.1.7 PF4 and Its Role in Thrombocytic Thrombocytopenia

platelent factor 4 (PF4) is a homotetrameric protein consisting of four 70 amino acid (7kD) chains that contain no methionine, tryptophan, or phenylalanine [81, 82]. PF4 belongs to the CXC chemokine family and is secreted from the α-granules of activated platelets to promote blood coagulation and attract neutrophils, monocytes, and fibroblasts to sites of injury [83]. PF4 functions to promote thrombosis by binding heparin or cellular glycosaminoglycans (GAGs) and therefore inhibiting the activity of coagulation cascade inhibitor antithrobin. A syndrome known as heparin-induced thrombocytopenia is associated with patients who produce rare autoantibodies that bind the PF4-heparin complex [84]. The administration of heparin to prevent blood clotting is commonplace during various cardiovascular interventions. Upon administration of heparin these patients have dangerous paradoxical thrombosis and throbocytopenia [85]. The disorder is caused when IgG binds to PF4-heparin and then the Fc domain of IgG is recognized by FcγRIIa receptors on the surface of platelets [86]. This causes platelet activation and formation of platelet microparticles leading to thrombosis and thrombocytopenia (Figure 1.5) [87].

1.1.8 A Synopses of Cryo-Electron Microscopy

Cryo-EM or more specifically CryoTEM (transmission electron microscopy) with subsequent SPA (single particle analysis) is a method which is revolutionizing the field of structural biology and has been extensively reviewed previously [88, 89]. Exciting advances in electron detector and energy filter technology have been rapidly transforming this discipline, once termed ”blob-ology”, into a contender as the premier technique for

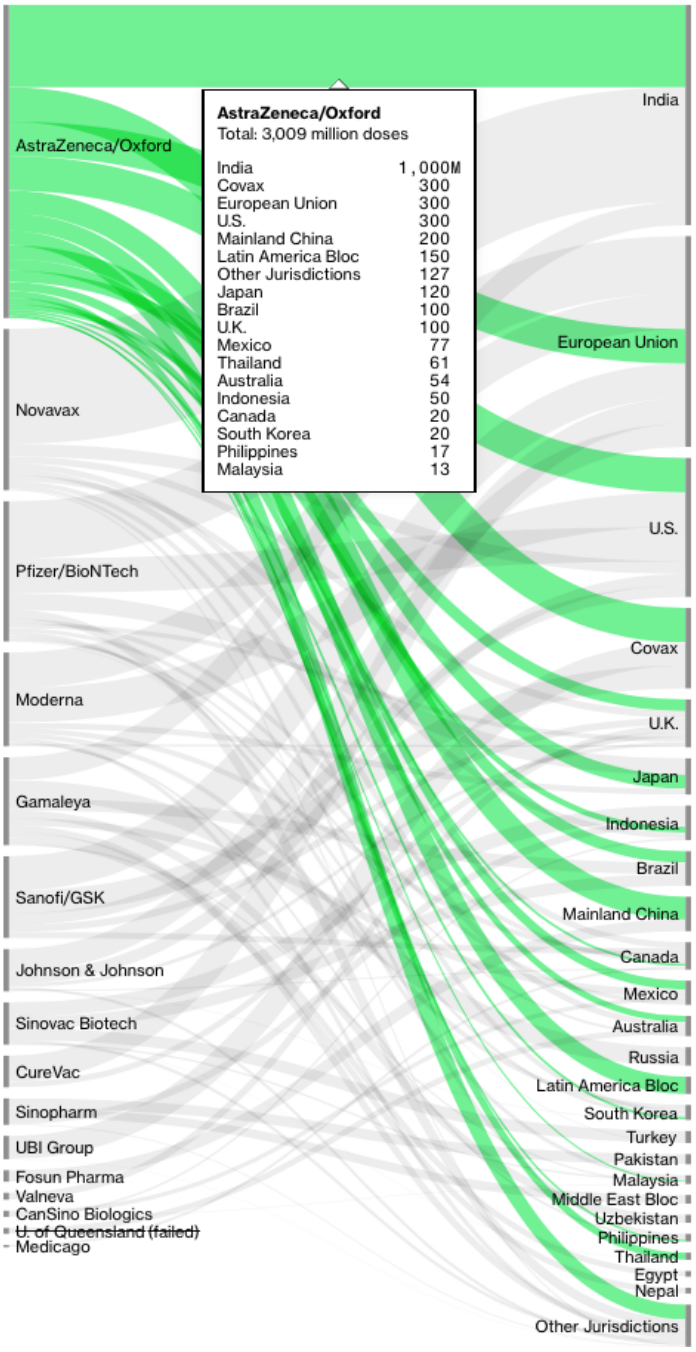

Figure 1.4: As of March 9, 2021, there were pre-purchase agreements for over three billion doses of AstraZeneca/Oxford's vaccine. This vaccine is by far the most sought after COVID-19 vaccine around the world, especially due to its ability to be stored at normal refrigerator temperatures, while other vaccines might need ultra cold storage [80].

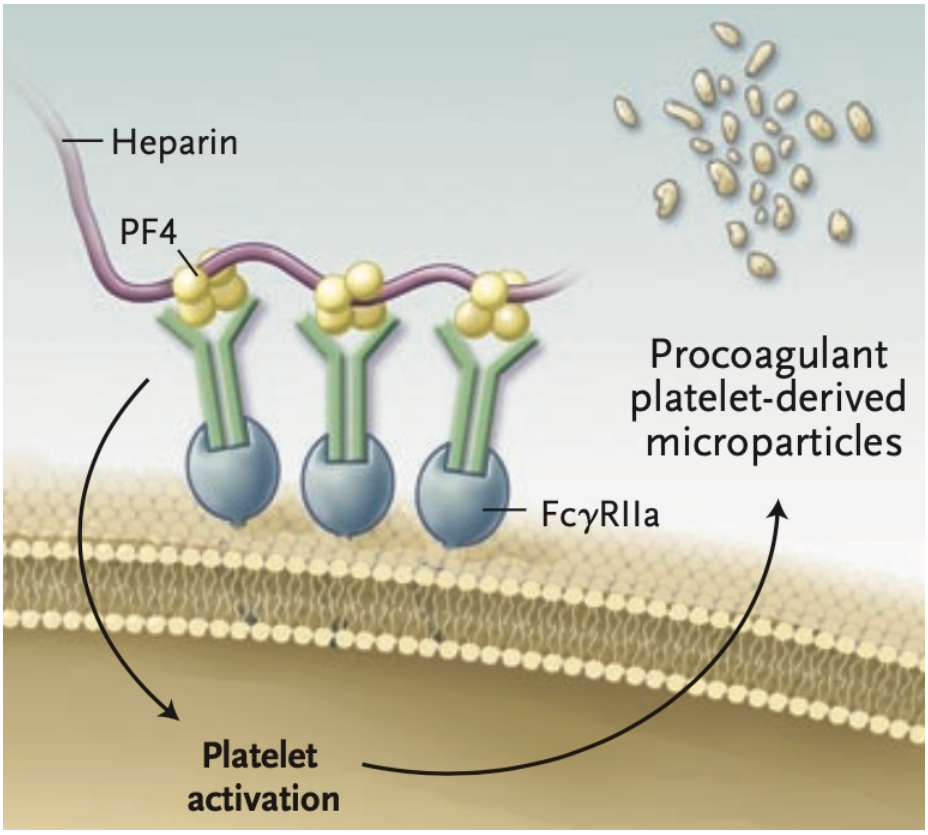

Figure 1.5: PF4 strongly binds heparin. In patients with heparin-induced thrombocytopenia, this complex is recognized by IgGs. IgG subsequently is bound by FcγRIIa receptors, which cluster and cause hyper activation of platelets, leading to thrombosis and subsequent thrombocytopenia [87].

resolving the structure of proteins.

In brief, the technique begins with purified protein being applied to a grid, and then flash frozen in liquid ethane in order to preserve the sample in vitrified non crystalline ice. Blotting, grid application, and freezing conditions are carefully controlled to optimize the ice thickness and sample distribution for each sample. The grid is kept at liquid nitrogen temperatures in order to reduce beam induced radiation damage during imaging (Figure 1.6F, ”Sample preparation”). Electrons from the microscope pass from the field emission gun (FEG), through several lenses and apertures to produce a controlled beam of electrons that pass through the grid and absorb or elastically scatter upon interaction with the

sample, capturing information about the sample in the form of differential contrast in the image recorded by the microscopes detector. Electrons are used because their small wavelength allows images to be captured at a resolution much higher than that of light, which is necessary to observe the structure of biomacromolecules on a molecular scale [89]. The resulting contrast information is collected in the form of movies that need to be motion corrected in order to account for beam induced motion of the grid and sample particles within the ice. After motion correction, the contrast transfer function is solved for each image in order to correct for artifacts in the imaging process such as defocus and spherical aberrations which may blur the image and reduce resolution. Once images have been sufficiently processed, single particle analysis begins with picking the coordinates of particles in each image. Particles must be sufficiently homogenous and well centered or subsequent classification and reconstruction may be negatively affected. Particle positions are then used to extract sub-images of each particle and then 2D classification is used to asses dataset quality and homogeneity. Bad particles are removed by iterative rounds of 2D classification to ensure that the dataset consists of particles that will be useful in 3D reconstruction. At this stage an initial 3D model or density map of a similar structure is procured in order to seed 3D classification, and any symmetry operations are applied to the seed and the dataset. Several rounds of 3D classification are used to further ensure that the dataset contains high-quality images suitable for reconstruction. At this stage 3D classification also allows for the differentiation of classes that may represent different dynamic states of the protein, so various 3D classes in differing conformations may be separated for out later processing (Figure 1.6F, ”Single particle analysis”) [88, 90]. Refinement begins by seeding the refinement with a low resolution shape in order to initiate projection alignment in Fourier space by the common lines method. The projection-slice theorem states that a 2D projection of a 3D object in real space is equivalent to taking a 2D slice of the fourier transform of a 3D object, therefore using

projection matching in fourier space one may reconstruct the orientation of each projection. To achieve this, theoretical reference projections of the seed shape are generated and experimental data is matched to the theoretical references to determine the likely orientation (Figure 1.6A-E) [90]. Upon reverse transform the 3D shape is updated and then the resolution of the resulting shape is calculated with the use of a mask to separate data from background noise using the gold standard FSC method [91]. This process is iterated over many times using starting refinement data and masks from the previous iteration to improve image alignments and optimize resolution estimates during post processing (Figure 1.6A-E). At this stage particle polishing and CTF refinement may be used to further improve image quality. These methods for improving data quality may further improve high resolution reconstruction during subsequent iterations of refinement. After resolution improvements from refinement have plateaued, the map is sharpened based on signal to noise parameters present in the data to produce an optimal map for model fitting (Figure 1.6, ”Single particle analysis”) [90, 92, 93]. Finally, software such as MDFF or Phenix may be used to fit a homology model of the target protein into the cryo-EM map. The map to model fit is iteratively improved based on model metrics from EM-ringer, either automatically with MDFF or Phenix or manually fit by utilities such as Coot or Isolde [94–97].

1.1.9 A Brief History of Adenovirus Structural Biology

A seminal paper in 1984 led by Jacques Dubochet at EMBL titled ”Cryo-Electron Microscopy of viruses” first showed the potential of CryoEM by imaging adenovirus in vitrified ice. This was considered the first ”Cryo-EM” paper, and demonstrates the tractability of imaging viruses by this technique [99]. The first human adenovirus (Ad5) structure was solved in 2010 by x-ray crystallography in Glen Nemerow’s lab at scripps [100]. The next time an adenoviral structure was solved it was in the lab of Nemerow’s

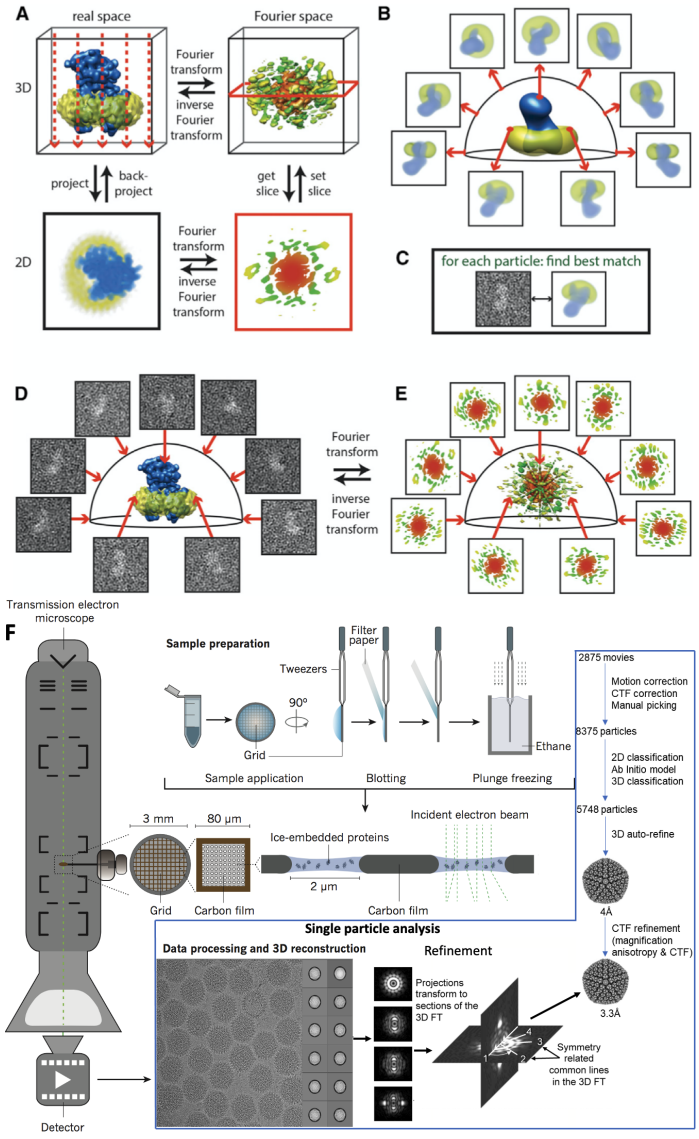

Figure 1.6: (A) the projection-slice theorem states that a projection of a 3D object can be represented as a slice through the Fourier transform of that object. (B-E) Projection mapping is a refinement method that uses the projection slice theorem to attempt to fit back calculated Fourier transforms of a starting 3D shape with the Fourier transform of 2D data in order to determine the orientations of each projection, and reconstruct the 3D object in real space. By iteratively improving the structure, alignments in real space get better and resolution improves with each refinement round as optimal projection orientations are found. (F) Cryo electron microscopy begins with sample preparation. Flash freezing samples in liquid ethane preserves their structure in vitrified ice and cools them to the liquid nitrogen temperatures needed for data collection. Subsequent single particle analysis involves image processing to produce optimal images, followed by 2D classification and 3D classification to improve the homogeneity of the dataset. After the date is sufficiently homogeneous, iterative rounds of refinement and post processing produce 3D density maps with improved resolution as image alignments improve [90, 98].

student Vijay Reddy, who solved the structure 5TX1 of human adenovirus D 26 by Cryo-EM to a resolution of 3.7Å in 2017 [101]. Finally, the highest resolution structure of an adenovirus currently in the PDB to date is the 3.2Å 6B1T structure of adenovirus type 5, solved by Cryo-EM also in 2017 in Hong Zhou's lab at UCLA [102]. These structures represent a critical leap forward in understanding and engineering adenovirus based vectors for the benefits of human health and disease prevention.

1.1.10 Advantages and Challenges of Adenovirus Cryo-em

Cryo-EM excels at imaging large, rigid protein assemblies with a high degree of symmetry and homogeneity such as a viral capsid. As such, adenoviruses represent an ideal target for high resolution Cryo-EM. The advantages of a large particle stem from the fact that in TEM the contrast is derived from the amount of elastically scattered electrons which reach the detector and form an image. In the case of large particles, many electrons are scattered and therefore the signal produced by the particle is much larger than the background noise, thus leading to particle images with very well defined features that are easily classified and aligned during SPA. The advantages of symmetry reflect the fact that images in a cryo-EM data set are a 2D projection of a 3D object in a distribution. Therefore in order to reconstruct the 3D shape, the Fourier transform of the images is computed and the image orientations are first determined using the common lines algorithm to determine the precise amplitude and phase orientations of all projections within the 3D shape. The amount of data or "slices" to produce that shape is a limiting factor to the resolution that can be obtained. When an object has icosahedral symmetry, this data can be multiplied across every asymmetric unit and also the only orientations for which "slices" of data are needed correspond to the asymmetric unit of the viral capsid. Because each particle contains 60 asymmetric units, all in varying orientations, this means that the dataset can essentially be multiplied by 60 to produce the real number of useful

particles used for reconstruction [6]. These advantages mean that high resolution structures of adenovirus are highly tractable and readily achievable from a relatively small number of particles. These factors make adenoviruses an ideal candidate for high resolution Cryo-EM, however the adenovirus's large size can also be a limitation. This is because of the fact that the the projection theorem used to reconstruct the virus incorrectly assumes that EM images are true projections and does not take into account the fact that the image contains artifacts from electron interactions with the curved radius of the 3D particle. The Ewald sphere describes the constellation of data points that represents a 3D shape in Fourier space, in this case as it regards the Fourier transform performed during reconstruction for the purpose of projection matching in refinement (This is similar to the structure factors in a crystallographic dataset, which also represent the Fourier transform of a 3D object in space as observed during diffraction) (Figure 1.6A). For small particles with less depth and at lower resolution this effect is small, but for large particles like adenoviruses the effects of assuming projections contain no artifacts from the 3D shape of the object observed can produce significant aberrations that limit the resolution of the reconstruction. Recently, methods for Ewald sphere correction have been implemented in Relion that reliably improve the maximum resolution of large particle reconstruction [103]. The details of this algorithm are outside the scope of this dissertation, however a brief overview can be given as follows: the correction algorithm referred to as `Prec` in the Bsoft and EMAN packages calculates the images' 2D fourier transforms, applies contrast transfer function (CTF) correction, and then calculates the Z coordinate for each Fourier coefficient, thus correcting for the missing information about the Ewald sphere, before adding the corrected coefficients to the corresponding points on the 3D reconstruction Fourier transform[104, 105]. Therefore, upon amplitude weighting and reverse Fourier transform into real space, the map has been corrected for Ewald sphere aberrations [103]. Other limitations of adenovirus SPA stem from the fact that large images must be used for

refinement, meaning that during image processing massive amounts of computational memory are required. Due to the nyquist limit, usually stated as half of the sampling rate of a given signal, the maximum achievable resolution in an EM image is twice the pixel size. An adenovirus particle must be processed with a pixel size of 1.3Å/pixel to reasonably achieve map resolutions below 3Å. To reach this nyquist limit a very large box size is needed. For perspective, an un binned adenovirus box size is on the order of 1400 pixels collected with an approximate 1.2Å/pixel size, meaning that the memory requirements for refinement of a hypothetical 5000 particle data set are as follows:

$$\text{Memory} = \frac{number of particles * box\_size * box\_size * 4}{(1024 * 1024 * 1024)} = 36.5Gb$$

Considering that this calculation does not account for a further 20% increase in dynamic memory use depending on the function running in Relion, this estimate is well beyond the on board memory of most GPUs and means that these data sets must be processed using CPU cores, increasing processing times by orders of magnitude when compared with normal data sets [92].

1.2 The RhoGEF Syx is Associated with Glioblastoma Tumor Invasion

1.2.1 Small GTPases and GEF Function

Rho GTPases make up a branch of the Ras-superfamily of small GTPases that contains 154 known proteins that typically function as signaling nodes [106]. Hyper activation of Rho GTPases can result in aberrant changes in cell proliferation and survival, angiogenesis, cell-cell interactions, cell migration, and cell shape and polarity [107–110]. Here we focus heavily on cell migration, which is characterized by the formation of an

apical edge of a cell, attachment of cellular protrusions to the surrounding extracellular matrix, and contraction of actin filaments within the cell to pull it towards the leading edge. All of these stages are directly linked to pathways modulated by Rho GTPase signaling through kinase cascades propagated from downstream effectors. RhoA in particular has been shown to be indispensable for modulating stress fiber production, cell chemotaxis, and movement at the leading edge of cells, and to a lesser degree, cell proliferation signals through it's downstream effector proteins ROCK and Dia (Figure 1.7) [109–111].

Each member of the Ras-superfaimily contains a conserved 20 kDa G-domain comprised of a mixed six-stranded β-sheet surrounded by five helices, which is responsible for guanosine nucleotide binding and hydrolysis [106, 112]. These proteins are often likened to a switch, however this simple "on" or "off" analogy is an over simplification with respect to the signaling effects in the cell. It is more useful to think about the behavior of a local population of GTPases functioning together. For this analogy, a potentiometer controlled by a logic gate would be a more apt comparison given that Ras family GTPases convey dynamic levels of signal propagation and integrate inputs from a multitude of pathways to mediate a tightly controlled level of activation and inactivation by upstream control proteins called GEFs and GAPs which are themselves under spatiotemporal control (Figure 1.7). The mechanism by which these pathways are regulated is based on conformational changes in the protein caused by guanosine nucleoside binding [113]. When GDP is bound, the small GTPase is in its inactive state; when GTP is bound, the small GTPase is in its active state and will interact with, and activate, proteins downstream of it, promoting a signaling cascade until GTPase activity hydrolyzes the GTP gamma phosphate, rendering RhoA back into its inactive GDP bound state. RhoA and most other small GTPases are membrane-associated proteins that are spatially targeted to different membrane locations within the cell based on the variable

sequences at their C-terminus (Figure 1.7) [114]. In the case of RhoA, a cysteine is modified by the addition of a gerynylgerynyl group by gerynylgerynyl transferase before the protein is exported out of the ER and sent to the membrane surface [112, 115, 116].

The level of signal propagated through small GTPases is dynamically modulated by two classes of proteins that mediate its activation or inactivation. GTPase Activating Proteins or GAPs are inhibitory to signal proliferation. GAPs bind to small GTPases and accelerate the hydrolysis of GTP to GDP thereby turning them off and inhibiting the corresponding signaling cascade. Conversely, GEFs or Guanosine Exchange Factors bind to the GTPases and distort the active site, facilitating the removal of GDP. GTP, found in high concentrations in the cytosol, is subsequently bound to the GTPase, switching it to its active form, releasing the GEF to continue catalyzing the activation of other Rho GTPases (Figure 1.7) [107].

The Rho GTPase interactions with GEFs and GAPs are tightly regulated via spatiotemporal mechanisms. In humans there are 83 known GEFs. The diffuse b-cell lymphoma (Dbl) homologous class of GEFs possesses a 200 residue Dbl homology (DH) domain that catalyzes the exchange of GDP for GTP, and an adjacent 100 residue pleckstrin homology (PH) domain which can either enhance catalysis of nucleotide exchange or inhibit it based on whether it is bound to the correct binding partner (Figure 1.7) [107, 112, 117, 118]. The PH domain is generally associated with binding the negatively charged phosphorylated head group of phosphoinositol lipids which facilitate spatial targeting and activation throughout the cell [119, 120]. In addition to these domains, GEFs invariably have several other auto-inhibitory domains that are spatially targeted to various locations in the cell, most notably receptor complexes where they reside until the correct factors are in place to activate their cognate Rho GTPase, thus propagating a signaling cascade [107, 112].

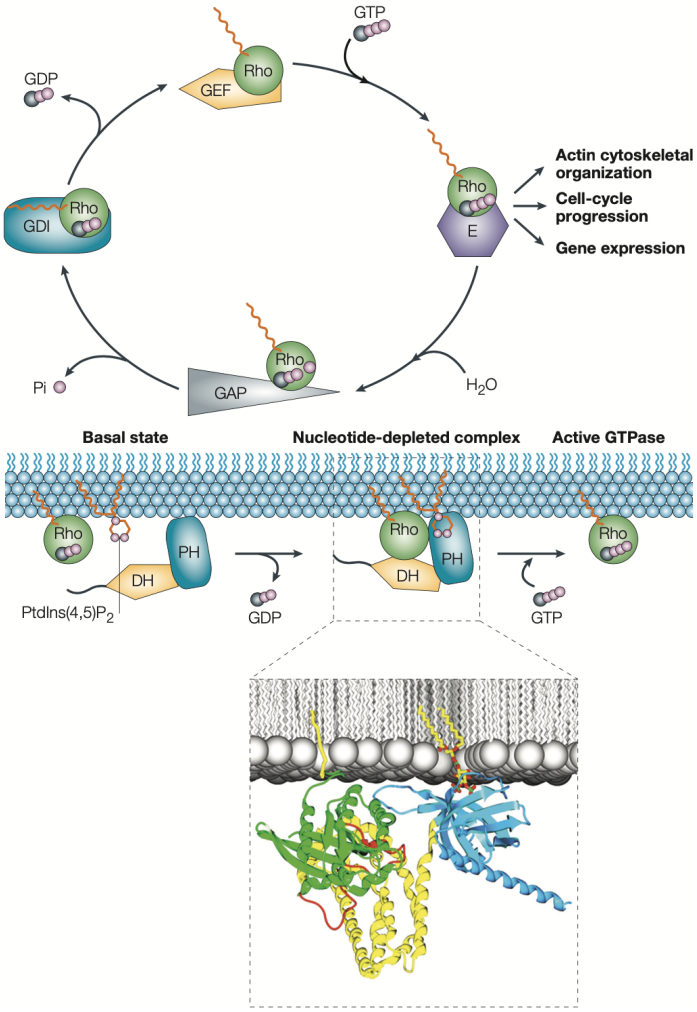

Figure 1.7: The Rho GTPase cycle of activation and inactivation is dynamically regulated by spatiotemporally targeted GEFs and GAPs to produce a tightly controlled downstream signal in the form of a kinase cascade. Rho GTPases and RhoGEFs are spatially targeted to the membrane where they function in conjunction with trans membrane receptor complexes and scaffold proteins bound to multiple regulatory factors which may be influenced by lipid phoshorylation dynamics to regulate multiple cell functions [107].

1.2.2 Glioblastoma Epidemiology and Inadequacies with Current Treatment Strategies

Currently, patients diagnosed with glioblastoma multiforme (GBM) face a dismal prognosis. Most patients with this form of brain cancer survive approximately one year, with only 5% of patients surviving longer than five years [121]. Challenges to successful treatment are due to the diffuse nature of these tumors, making eradication of all tumor cells with surgery and radiotherapy difficult. There is currently no standard of treatment for recurrent GBM. Aggressive growth and tumor invasion into the surrounding tissue means that without effective targeted drug therapies, post-surgical outcomes are unlikely to improve.

Tumor invasion and development of drug resistance are two of the greatest challenges for the successful treatment of glioblastoma multiforme (GBM). GBM is the most common and most aggressive form of brain cancer. Approximately 10,000 people in the United States are diagnosed with GBM every year and mean survival times after aggressive intervention are only 15 months due to rapid tumor growth and invasion of the surrounding tissue. Current treatments for GBM require surgery followed by radiotherapy and chemotherapy with temozolomide (TMZ) and subsequent treatment with the VEGF targeting anti-angiogenic antibody Bevacizumab (Avastin) [122]. The heterogeneity and diffuse nature of these tumors often makes traditional interventions like surgical removal and radiotherapy very difficult [123]. Furthermore, the blood–brain barrier drastically limits the effective absorption of chemotherapy agents and other drugs that might otherwise be effective treatments. The resulting effects of these challenges is a fast growing cancer with a high metastatic potential that often cannot be effectively removed from the body, leaving many cells that can potentially develop resistance to chemotherapy and cause recurrence of cancer. For recurrent GBM there is currently no effective standard treatment when first line treatments fail [123].

1.2.3 Syx Biology and Glioblastoma

Syx is a 1073 residue protein that is associated with promoting cell-cell junction stability, and is known to bind to membrane associated NG2 bound poly PDZ domain protein MUPP1 via its PDZ binding motif where it regulates tight junction maintenance and cell polarity [124]. Syx GEF activity is inhibited by PKD-mediated phosphorylation-dependent inhibitory binding of 14-3-3 proteins [125]. Syx shares approximately 20% sequence homology with PDZRhoGEF, P115-RhoGEF, and Leukemia Associated RhoGEF (LARG). Each of these proteins has been successfully co-crystalized with RhoA [126–130]. In the case of LARG, computational drug design resulted in a selective inhibitor Y16, which binds the hinge region between the DH and PH domains. This hinge region and PH domain sequences are divergent among RhoGEFs, indicating their potential to be selectively targeted by structurally guided drug design.

Syx has been extensively characterized by our collaborators the Anastasiadis lab at the Mayo Clinic in Jacksonville [109, 125, 131–133]. They have conclusively shown that the Syx is highly expressed in human gliomas and may play an important role in RhoA based GBM proliferation and tumor invasion.

In 2013, Dachsel et al. showed that shRNA based knockdown of Syx in U251 cells, a classic cellular model of human GBM, and resulted in dysregulation of microtubules, focal adhesions, and static cell polarity (Figure 1.8) [131]. This manifested as an inability to form an apical leading edge, resulting in inhibition of cell movement, as well as a striking change in cell morphology from a typical cell shape to a “fried egg” phenotype during scratch assays and trans well migration assays (Figure 1.8). In addition, they showed that removing the C-terminal PDZ binding domain, shown to bind to members of the Crumbs polarity complex and the proteoglycan NG2 at the inner cell membrane, will also result in inhibition of chemotactic movement and characteristic “fried egg” phenotype seen in Syx

knockdown experiments (Figure 1.8). This work suggests that inhibition of Syx could be a powerful treatment to improve the survival of patients with glioblastoma.

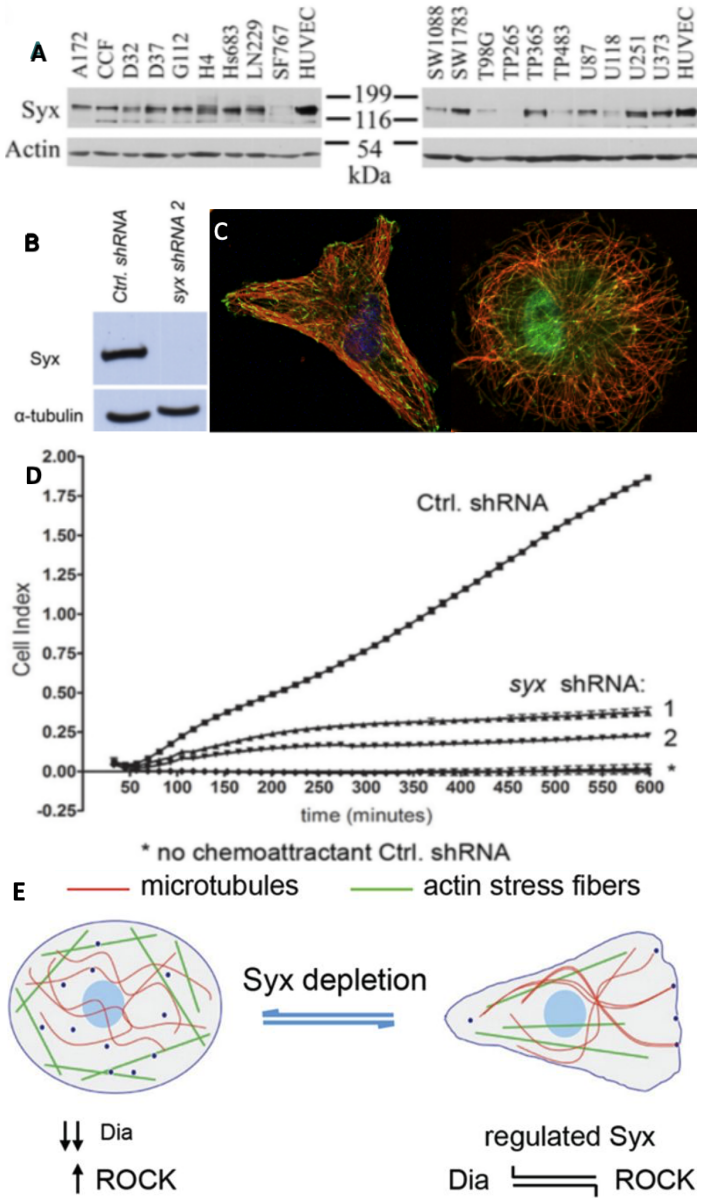

Figure 1.8: A) Western blot shows presence of Syx in several different glioblastoma cell lines. HUVEC is used as a positive control. B) Western blot of Syx expression in U251 cells with and without Syx targeted shRNA inhibition. C) Knockdown of Syx with shRNA results in a morphological shift from normal cell shape with apical protrusions, to a round "fried egg" morphology. D) Cell motility measured with and without shRNA Syx inhibition. E) Cartoon for Syx behavior in the cell, where Syx depletion causes a reduction in Dia mediated microtubule capture and bundling and an increase in ROCK activation [131].

Chapter 2

CHADOX1 INTERACTS WITH CAR AND PF4 WITH IMPLICATIONS FOR THROMBOSIS WITH THROMBOCYTOPENIA SYNDROME

Alexander T. Baker†, **Ryan J. Boyd**†, Daipayan Sarkar‡, Alicia Teijeira-Crespo‡, Chun Kit Chan‡, Emily Bates, Kasim Waraich, John Vant, Eric Wilson, Chloe D. Truong, Magdalena Lipka-Lloyd, Petra Fromme, Josh Vermaas, Dewight Williams, LeeAnn Machiesky, Meike Heurich, Bolni M. Nagalo, Lynda Coughlan, Scott Umlauf, Po-Lin Chiu, Pierre J. Rizkallah, Taylor S. Cohen, Alan L. Parker, Abhishek Singharoy, and Mitesh J. Borad

†,‡ authors contributed equally to this work

2.1 Abstract

Vaccines derived from chimpanzee adenovirus Y25 (ChAdOx1), human adenovirus type 26 (HAdV-D26), and human adenovirus type 5 (Ad5) are critical in combatting the SARS-CoV-2 pandemic. As part of the largest vaccination campaign in history, ultra-rare side effects not seen in Phase-III trials, including thrombosis with thrombocytopenia syndrome (TTS), a rare condition resembling Heparin induced Thrombocytopenia (HIT), have been observed. This study demonstrates that all three adenoviruses deployed as vaccination vectors versus SARS-CoV-2 bind to platelet factor 4 (PF4), a protein implicated in the pathogenesis of HIT. We have determined the structure of the ChAdOx1 viral vector and utilised it in state-of-the-art computational simulations to demonstrate an electrostatic interaction mechanism with PF4, which was confirmed experimentally by surface plasmon resonance. These data confirm PF4 is capable of forming stable complexes with clinically relevant adenoviruses, an important step in unraveling the mechanisms underlying TTS.

2.2 Introduction

The ChAdOx1 viral vector, adapted from chimpanzee adenovirus Y25 (ChAd-Y25), is the basis for the ChAdOx1 nCoV-19 vaccine (AZD1222/Vaxzevria) [71]. ChAdOx1 nCoV-19 induces robust immunity against the severe acute respiratory coronavirus 2 (SARS-CoV-2), protecting against severe symptoms requiring hospitalization, in 100% of clinical trial recipients, and infection of any severity, in approximately 70% [69, 134]. A potentially life-threatening clotting disorder, thrombosis thrombocytopenia syndrome (TTS), which presents similarly to heparin induced thrombocytopenia (HIT) has been observed in a minority of AZD1222 recipients following the first dose, but not the second [135–138]. Similar observations have been made in recipients of the Janssen Ad26.COV2.S vaccine, derived from the species D human adenovirus type 26 (HAdV-D26)[137, 139]. The pathological mechanism underpinning this condition, termed thrombosis with thrombocytopenia syndrome (TTS), is unknown, although recent reports highlight a probable role for platelet factor 4 (PF4)[140, 141]. Detailed mechanistic understanding of the virus/host interactions of adenovirus-derived vectors has facilitated their advancement to the clinic. Previous work has shown that the presence of pre-existing neutralizing antibodies targeting an adenoviral vector can limit therapeutic efficacy, neutralizing the vector before it has therapeutic effect [66, 142]. Following intravenous (IV) administration of Ad5, studies uncovered important in vivo interactions including high-affinity interactions with coagulation factor X (FX), and/or platelets. These interactions contribute to vector degradation, and consequently to reduced therapeutic index [143–145]. Collectively, this knowledge drove the field to develop adenoviral vectors with low seroprevalence, including ChAdOx1 and Ad26, and engineering of capsid proteins to overcome these issues[10]. It is critical to investigate the vector-host interactions of ChAdOx1 to determine how it may contribute to rare adverse

events like TTS. Here, we characterized the capsid structure of ChAdOx1 and the primary receptor binding fiber-knob protein. We used this structural information to investigate its ability to interact with potential partners, including CD46, coxsackie and adenovirus receptor (CAR), and PF4. We confirmed our observations in vitro using cell based experiments, and surface plasmon resonance (SPR). These data clarify our understanding of whether ChAdOx1 interacts with host proteins thought to be involved in immunogenicity, HIT, and TTS.

2.3 Materials and Methods

2.3.1 Propagation of ChAdOx1 Virus

10 x T225 CellBind™ cell culture flasks (Corning) were seeded with approximately 5x106 HEK-293 T-Rex cells (Invitrogen) each. Cells were cultured in DMEM (Gibco) supplemented with 10% heat inactivated fetal bovine serum and 1% penicillin/streptomycin (Gibco) until 80% confluent. Cells were infected with ChAdOx1.eGFP, provided by the Coughlan Lab (University of Maryland), at a multiplicity of infection of 0.01. Cells were then monitored for cytopathic effect (CPE). When culture media turned yellow media was replaced. Once CPE became evident, but the cells were not ready to be collected, yellowed media was supplemented with sodium bicarbonate buffer (pH7.4, Gibco) until it reddened. This was done to retain the virus released into the media. Once CPE was observed in >80% of the cell monolayer the cells (5-8 days post infection) were dissociated from the flask by knocking. The supernatant and cells were separated by centrifugation at 300g for 5mins, both were stored at -80C until ready for purification.

2.3.2 ChAdOx1 Purification

ChAdOx1 containing media was clarified by centrifugation at 4000RPM for 10mins in a bench top centrifuge. Supernatant was then loaded into 38ml Ultraclear tubes compatible with the SW28 rotor (Beckman-Coulter) and centrifuged at 100,000g for 1hr in a Beckman-Coulter Optima XPN-100 ultracentrifuge. Supernatant was discarded and the pellet, which was slightly yellow and sticky, was resuspended in 5ml PBS (pH7.4, Gibco). This 5ml of PBS containing the ChAdOx1 from the supernatant was used to resuspend the infected HEK-293 T-Rex pellet. This solution was then mixed in a 1:1 ratio with tetrachloroethylene (TCE, Sigma-Aldrich) and shaken violently to ensure thorough mixing. The virus, PBS, TCE mixture was then centrifuged at 2000RPM in a benchtop centrifuge for 20minutes. The aqueous top layer of the solution was removed by pipetting and placed into a new tube. A second TCE extraction was then performed by adding a further 5ml of TCE to the aqueous layer, shaking, and centrifuging, as before. This is performed to ensure maximum removal cell debris. Previous purifications which excluded this second extraction showed fatty deposits when analysed by negative stain transmission electron microscopy and resulted in viral aggregation. Next, the top, aqueous, layer was extracted again and the remainder of the purification was performed using the 2 step CsCl gradient method, as previous described[146], except for the following modification: during the final extraction of the virus containing band, which should have a crisp white appearance, the band was not removed using a needle through the side of the tube, but by pipetting. A P1000 pipette was used to slowly withdraw fluid from the tube, taking from the meniscus, careful not to disrupt the band. As much fluid was removed above the band as possible, then a new pipette tip was used to withdraw the band from the meniscus in as little volume as possible. This band was loaded into a 0.5mL Slide-A-Lyzer cassette with a 100,000 MWCO (ThermoFisher) and dialysed against 1L of plunge freezing buffer

(150mM NaCl, 1mM MgCl2, 20mM Tris, pH7.4). This solution was used to prepare grids for CryoEM.

2.3.3 Cryo-EM Grid Preparation

An UltrAuFoil grid (688-300-AU, Ted Pella Inc.) was glow-discharged on a PELCO easiGlow (Ted Pella Inc.) for 30 seconds. A Vitribot Mark IV automated plunge freezer (ThermoFisher) was used for blotting and freezing grids in liquid ethane using the following protocol: the sample chamber was set to 25˚C and 100% humidity, 2.5 µl of sample was applied onto both sides of the grid, and a blot force of 1 and a draining time of 3 second were used for plunge freezing. The frozen grid was transferred to cryo-boxes under liquid nitrogen for storage.

2.3.4 CryoEM Data Collection

The vitrified specimen was images using an FEI Titan Krios transmission electron microscope (TEM, ThermoFisher) operating at an accelerating voltage of 300 keV with a Gatan K2 Summit direct electron detector (DED) camera (Pleasanton, CA) at a nominal magnification of 37,313 X, corresponding to a pixel size of 1.34 Å/pixel at the specimen level. 2,875 movies, each consisting of 40 frames over the course of 8 seconds, were collected in super-resolution mode with a sub-pixel size of 0.67 Å/pixel. Defocus setting was cycled from -0.5 to -1.6 µm for each exposure. The dose rate was adjusted to 2.59 e-/pixel/second with 1.18 e-/Å2 per movie frame. Data were recorded and packed as a 4-bit and LZW-compressed TIFF format.

2.3.5 CryoEM Image Processing and Structure Determination

Datasets were processed using RELION (version 3.1.1) [92] on a workstation with an Intel I7-6800K 3.4 GHz processor, 800Gb of memory, a 1Tb SSD drive, and 4 NVIDIA

GTX 1080 GPUs. A large swap partition was set to 512 Gb. Motion correction was performed using RELION with a binning factor of 2 and removing the first three frames. CTF estimation was performed using CTFFIND (version 4.1). 8375 particles were picked manually. Particles were extracted with a box size of 1,440 pixels and then Fourier cropped to 512 pixels for particle curation and initial model building. Iterative 2D image classification was used to curate the data and poorly aligned particles were removed from the final image stack. An Ab initio model was generated using stochastic gradient descent method without imposing any symmetry. The model was then aligned with its phase origin with an icosahedral symmetry using `relion_align_symmetry` program before being used as a reference map for 3D classification. The selected 3D class was selected for further refinement. The refined particle images were re-extracted without rescaling and were curated using 2D classification without alignment. The final model was refined against the selected 5,748 particles supplying with a mask to remove the pixels within the inner sphere of a radius of 285 Å. The resolution was determined at 4.17 Å using gold-standard Fourier-shell correlation criteria [91]. Particles were re-extracted at a 1260 pixel box size to reduce Nyquist limitations. Refinement at this box size could not be run with GPU acceleration due to limitations in video card memory and therefore took careful consideration of memory requirements. Each iteration of refinement took approximately 3 days to finish while running on 9 MPI cores. Particles underwent CTF refinement with magnification anisotropy which resulted in a 3.50Å map after refinement. This was followed by further CTF correction which improved the map resolution to approximately 3.32Å. Bayesian polishing resulted in negligible improvements. Finally, The Ewald sphere curvature was corrected to yield a final map with an average resolution of 3.07Å as determined by RELION's implementation of gold standard FSC[147] or 3.04Å as determined by Phenix's `phenix.mtriage` function. The resulting map was sharpened with DeepEMhancer using `highRes`, `tightTarget`, and `wideTarget` training models

and required 2.5 days to run on 4 Nvidia V100 GPUs.

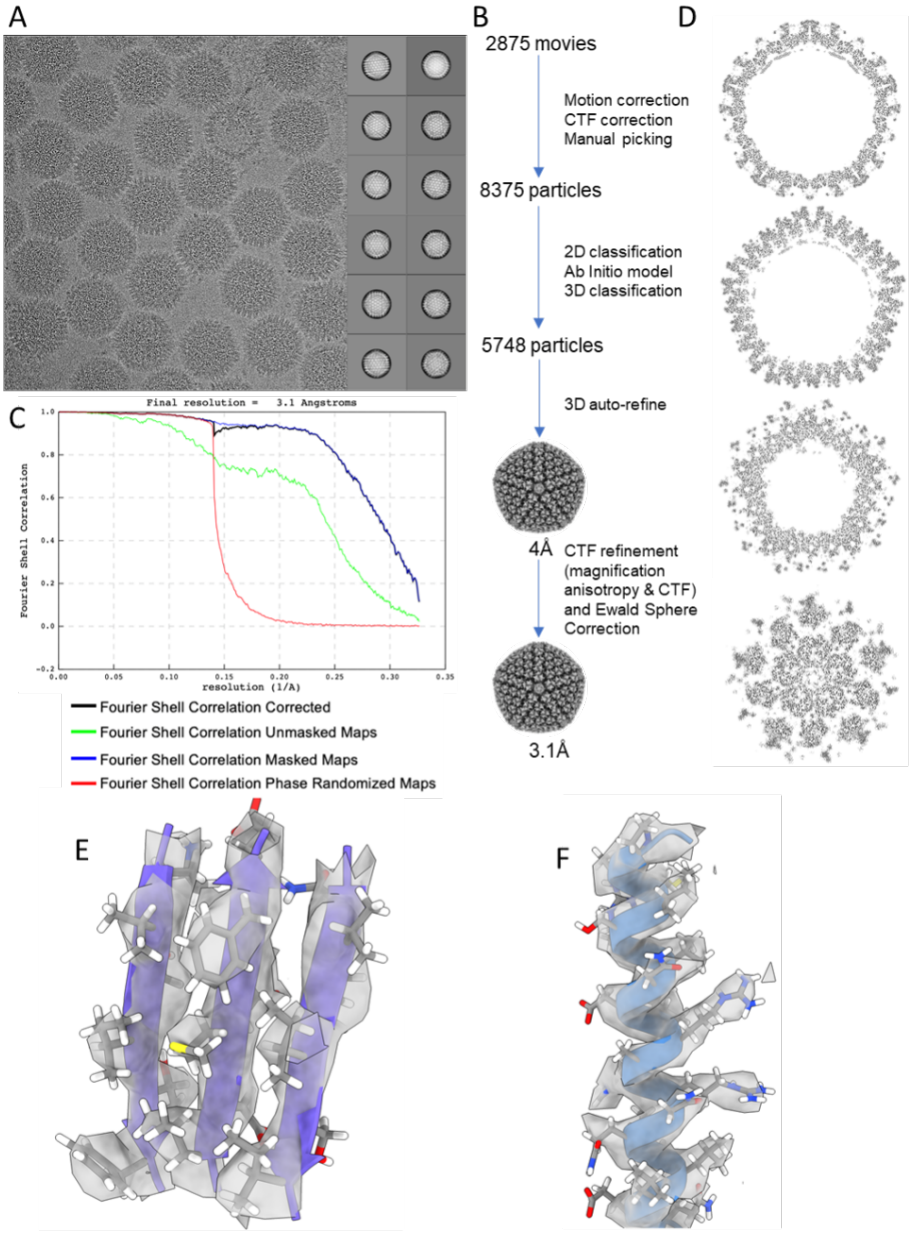

Figure 2.1: **Validation statistics for CryoEM ChAdOx1 structure.** Particles were hand picked from micrographs and 2D classified (A). After classification and refinement (B) a 3.3A volume was generated with acceptable Fourier shell correlation (C). Slices through the ChAdOx1 CryoEM volume show the localized resolution at the capsid interior has higher resolution information than the exterior which contains more flexible regions. An equatorial slice shows greater detail on the capsid interior, revealed in more detail by slices at points further along the 5-fold axis (D). The map enabled fitting of an atomic model (E, F).

ChAdOx1 capsid model building

The amino acid sequence of the ChAdOx1 virus capsid proteins are described in the genome sequence of the source chimpanzee adenovirus type Y25 (ChAdV-Y25) used to develop the ChAdOx1 vector (NC_017825.1). There are no differences between ChAdOx1 and Y25 in the capsid proteins. The I-TASSER webserver[148] or SWISS-MODEL[149](48) was used to build homology models of the various ChAdOx1 capsid proteins. Initially, the atomic models obtained from the web-server were rigid body fitted to the capsid density map using ChimeraX[150], first by manual placement and then using the fit in map algorithm, beginning with the hexons, then the penton, pVIII, pIX, pIIIa, respectively, until a full asymmetric unit had been assembled. After initial placement of the atomic model inside the density map, the model was fitted using the method molecular dynamics flexible fitting (MDFF) in explicit solvent[97, 151]. To avoid fitting of atomic models into adjacent density, additional protein models were added surrounding the asymmetric unit to occupy those regions of the density map. This 'buffered' asymmetric unit was then subjected to another round of MDFF in explicit solvent to improve the quality of fit to the density map, while accounting for protein-protein interactions between protein sub-units. Models were then inspected and loop regions with low-resolution density were manually modelled using ISOLDE(52). The model was further refined using symmetry restrained MDFF to address clashes between asymmetric units and further improve the local fits at the asymmetric unit edge[152]. All MDFF simulations were performed in NAMD 2.14[153] using the CHARMM36[154] force field for protein, water and ions at 300 K. The initial system for every MDFF simulation was prepared using the software Visual Molecular Dynamics, VMD 1.9.3[155]. The potential energy function (UEM), obtained by converting from the EM density map was applied to the protein backbone during flexible fitting with a g-scale

of 0.3. During flexible fitting, standard restraints were applied to maintain secondary structure, cis-peptide and chirality in protein structures[156]. The model was then further refined using ISOLDE as implemented in ChimeraX. Finally, residues for which there was no signal were deleted from the model.

2.3.6 Crystallization and Structure Determination of the ChAdOx1 Fiber-knob Protein

Production and purification of ChAdOx1 fiber-knob protein

The method used to purify ChAdOx1 fiber-knob protein is identical to that described for HAdV-D26 and HAdV-D48, previously. To summarise, SG13009 E. coli containing the pREP-4 plasmid were transfected with pQE-30 expression vector containing the ChAdOx1 fiber-knob transgene, located C-terminal to the 6His tag site, consisting of the 13 residues preceding the TLW motif to the terminal residue. These E. coli were selected in 100µg/mL of Ampicillin and 50µg/mL of Kanamycin. They were cultured in 25ml LB broth with 100µg/ml ampicillin and 50µg/ml kanamycin overnight from glycerol stocks. 2L of Terrific Broth (Terrific broth, modified, Sigma-Aldrich) containing 100µg/ml ampicillin and 50µg/ml kanamycin were inoculated with the overnight culture and incubated at 37°C for 4 hrs until it reached an optical density (OD) of 0.6 at λ570nm. Once it reached the OD0.6 IPTG at a final concentration of 0.5mM was added and the culture was incubated for 18hrs at 21°C. Cells were harvested by centrifugation at 3,000xg for 10 mins at 4□C, resuspended in lysis buffer (50mM Tris, pH8.0, 300mM NaCl, 1% (v/v) NP40, 1mg/ml Lysozyme, 1mM β-Mercaptoethanol, 10mM Imidazole), and incubated for 15min shaking at room temperature. Lysate was then centrifuged at 30,000xg for 20 min at 4°C and filtrated through 0.22µm syringe filter (Milipore, Abingdon, UK). The filtered lysate was then loaded to 5ml HisTrap FF nickel affinity chromatography column (GE Life Science) at 2.0ml/min and washed with 15ml into

elution buffer A (50mM Tris-HCl or-Base pH8.0, 300mM NaCl, 1mM β-Mercaptoethanol). Elution was done using a gradient rate of 20min/ml from of buffer B (50mM Tris pH8.0, 300mM NaCl, 1mM β-Mercaptoethanol, 400mM imidazole). Collected fractions were concentrated by centrifugation using a Vivaspin 10,000 MWCO column (Sartorious, Goettingen, Germany) and analyzed by a SDS-PAGE gel stained with Coomassie Blue (correct bands are approximately 25kDa). A second round of purification was performed using a GE 10/300 GL Increase Superdex 200 (GE Life Science) size exclusion chromatography at 0.5 ml/min and washed with 50ml of Baker Buffer (50mM NaCl, 10mM Tris pH 7.6). Fractions were then analysed using an SDS-PAGE gel stained with Coomassie Blue to check purity and molecular weight.

Crystallization conditions

Final protein concentration was 13.5 mg/ml. For crystallization The BCS and PACT Premier commercial crystallization screens (Molecular Dimensions) were used. Crystals were grown at 20°C in sitting drops containing 1:1 (v/v) ratio of protein to mother liquor. Microseeding was required for optimal crystal growth. Microseeding experiment was set-up using Mosquito crystallization robot. Crystals appeared between 5-14 days. Crystallization condition for solved structure was 0.1 M Calcium chloride dihydrate, 0.1 M Magnesium chloride hexahydrate, 0.1 M PIPES pH7.0, 22.5% v/v PEG Smear Medium and 0.2 M Calcium chloride dihydrate, 0.1 M Tris pH8.0, 20% w/v PEG 6000.

Structure determination

Diffraction data were recorded on DIAMOND beamline DLS-I03, using GDA to control data collection. Automatic data reduction was completed with XDS and DIALS, and equivalents scaled and merged with AIMLESS and TRUNCATE[157]. The unique data set was used in PHASER to solve the structure with Molecular Replacement, using a

search model prepared by SWISS-MODEL based on the structure of Adenovirus C5 fiber knob protein, PDB entry 1KNB[158]. Repeated cycles of graphics sessions in COOT[159] and refinement in REFMAC5 resulted in the final model presented in this manuscript. It became clear that the data set suffered from twinning, which was automatically determined in REFMAC5 as 1 twin law, with a fraction of 0.15. Details of data collection and refinement statistics are included in supplamental figure 2.9A. Final coordinates are deposited in the wwPDB as entry 7OP2.

2.3.7 Modelling of Fiber-knob CAR Interfaces

The pre-existing structure of the HAdV-D37 fiber-knob in complex with CAR D1 (PDB 2J12)[160] was used as a template by which to fit other fiber-knob proteins, as previously described. The pre-existing structure of HAdV-C5 (PDB 1KNB)[158] and HAdV-B35 (PDB 2QLK)[161] were aligned to the HAdV-D37 fiber knob in PyMOL using the 'cealign' command, as was the fiber-knob structure of ChAdOx1[162]. New models were saved containing the three CAR chains and one of the fitted chimeric fiber-knob trimers. These homology models underwent 10,000 steps of energy minimization using a conjugate gradient and line search algorithm native to NAMD[153] and equilibrated by a short 2ns molecular dynamics simulation. These models, seen in A-C figure 2.3, A-C and extended figure 2.13 and binding interaction between the all three fiber-knob and CAR protein-protein interfaces were scored at each frame of the MD trajectory using the Rosetta InterfaceAnalyzer tool[163, 164].

2.3.8 Determination of Relative IC50 Values of CAR and CD46 Binding for Fiber-knob Proteins

Antibody binding inhibition assays were performed as previously described[165]. CHO-CAR and CHO-BC1 cells were harvested and 40,000 cells per well were transferred

to a 96-well V-bottomed plate (NuncTM; 249662). Cells were washed with cold PBS prior to seeding and kept on ice. Serial dilutions of recombinant soluble knob protein were made up in serum-free RPMI-1640 to give a final concentration range of 0.00001–100µg/105 cells. Recombinant fiber knob protein dilutions were added in triplicate to the cells and incubated on ice for 30 minutes. Unbound fiber knob protein was removed by washing twice in cold PBS and primary CAR RmcB (Millipore; 05-644) or primary CD46 MEM-258 (ThermoFisher; MA1-82140) antibody was added to bind the appropriate receptor. Primary antibody was removed after 1h incubation on ice and cells were washed twice further in PBS and incubated on ice for 30 minutes with Alexa-488 labelled goat anti-mouse secondary antibody (ThermoFisher; A-11001). Antibodies were diluted to a concentration of 2µg/mL in PBS. Cells were washed and fixed using 4% paraformaldehyde and staining detected using BD Accuri™ C6 cytometer (BD Bioscience). Analysis was performed using FlowJo v10 (FlowJo, LLC) by sequential gating on cell population, singlets and Alexa-488 positive cells compared to an unstained control. Total fluorescence intensity (TFI) was determined as the Alexa-488 positive single cell population multiplied by median fluorescence intensity (MFI) and IC50 curves were fitted by non-linear regression using GraphPad Prism software to determine the IC50 concentrations.

2.3.9 SPR Binding Assays

For Fiber-knob receptors

Binding analysis was performed using a BIAcore T200™ equipped with a CM5 sensor chip. Approximately 2000RU of CAR, DSG2 and CD46, was attached to the CM5 sensor chip, using amine coupling, at a slow flow-rate of 10µl/min. A blank flow cell was used as a negative control surface on flow cell 1. All measurements were performed at 25°C in

PBS buffer (Sigma, UK) with 0.001% added P20 surfactant (GE Healthcare) at 30µl/min. For binding analysis, the HAdV-C5, HAdV-B35 and ChAdOX fiber knob proteins were purified and flown over each sensor chip surface at a concentration of 0.5□M to confirm binding. To determine binding kinetics (on rate, ka (1/Ms); off rate, kd (1/s)) and affinity (KD (nM)), 1:2 serial dilutions were prepared for HAdV-C5K, HAdV-B35K and ChAdOX fiber knob proteins and injected over CAR, DSG2 and CD46 immobilised on each sensor chip surface. The equilibrium binding constant (KD) and kinetic values were calculated assuming a 1:1 interaction using the BIAevaluation software.

For PF4 interactions

Assays were performed using a BIAcore T200TM, Cytiva (formerly GE Healthcare). The assay immobilization buffer was HBS-EP+ (10mM HEPES, 150mM NaCl, 3mM EDTA and 0.05% v/v Surfactant P20). Virus at 1x1011VP/ml was diluted 1:5 in acetate 4.5 buffer and immobilized to a C1 sensor chip using a standard amine coupling protocol and a 15 min sample injection time. Typically, 400-500 RU (response units) of virus was immobilized. A reference sensor surface was created using the same amine coupling protocol but without the virus. Samples were injected with an association time of 60-120 sec and a dissociation time of 60-120 sec at a flow rate of 50uL/min. The surface was regenerated with a 30 second injection of 25mM NaOH at a flow rate of 50ul/min. All sensorgram plots were subtracted from the reference flow cell and a buffer cycle to remove the non-specific responses, bulk refractive index changes and systematic instrument noise For the salt gradient experiments, PF4 protein was diluted to 2000nM in HBS-EP+ with 1% BSA with various NaCl concentrations for the NaCl gradient experiments. For binding affinity measurements, PF4 was diluted to 3000nM in PBS+0.5% BSA. Two independent concentration series of PF4 was prepare using 1:3 dilutions. PF4 binding data was fit using the Biacore T200 Evaluation software using the

steady state affinity model. For heparin competition injections. PF4 was prepared to 2000nM and heparin was prepared to 200,000nM in PBS+1% BSA. Samples were prepared as described: heparin alone (1:1 mix heparin stock + buffer), PF4 alone (1:1 mix of PF4 + buffer) and heparin + PF4 (1:1 mix of heparin stock and PF4 stock to a final molar ratio of 100:1).

2.3.10 Sequence Alignments

Sequence alignments were performed using the Clustal Omega algorithm as implemented in Expasy[166].

2.3.11 Electrostatic Surface Calculations

The electrostatic effect from the icosahedral facet of ChAdOx1 on any point $r = (x, y, z)$ of its surrounding environment is quantified by its electrostatic potential at r, which is denoted as $V(r)$. This potential V was determined using the code, Adaptative Poisson-Boltzmann Solver (APBS)(66). APBS computed V using the charge distribution of ChAdOx1, the ion concentration of the environment surrounding ChAdOx1, and the permittivity of the environment. The computed V thus took into account the presence of counter ions in and the polarizability of the environment, which was a bulk of water molecules in our study. As the sign, + or -, of $V\ (r)$ is highly correlated with the number of positive or negative charges around r, the potential for platelet factor 4 (PF4) was also computed to visualize the overall charge distribution of PF4 upon its binding to ChAdOx1. The starting model for PF4 and PF4 in complex with fondaparinux was PDB 1RHP and 4R9W, respectively.

2.3.12 Brownian Dynamics Simulation of the Icosahedral Facet in Solution with PF4

Multi-replica Brownian dynamics (BD) simulations were performed using the code, Atomic Resolution Brownian Dynamics (ARBD)[167]. During the simulations, copies of PF4 were treated as rigid bodies diffusing in the neighborhood of the icosahedral facet of ChAdOx1 in solution. The equation of motion (EOM) obeyed by each copy of PF4 for its diffusion in BD simulations is the over-damped Langevin dynamics. This EOM requires knowledge of the forces from the environment on PF4 as well as its damping coefficients with the environment. These coefficients, translational damping coefficients and rotational damping coefficients, were determined using the code, Hydropro[168]. The forces from the environment on PF4 consisted of 2 parts. The 1st part consisted of the random forces from thermal fluctuations. These random forces were automatically generated by ARBD during simulations based on the system temperature T, which is 310K here. The 2nd part consisted of the electrostatic force and the Van der Waals (VdW) force on PF4 from the icosahedral facet. The electrostatic force on PF4 with its center of mass (COM) at any point r was computed by ARBD automatically using the electrostatic potential V of the icosahedral facet and the charge distributions of PF4 around r. Similarly, we specify the VdW force between the icosahedral facet and PF4 using a potential, the Lennard-Jones (LJ) potential, denoted as U here. This potential U was computed using the code, Visual Molecular Dynamics (VMD)[155]. LJ parameters needed for this computation were adopted from the Charmm36m force field[169]. The various potentials for the icosahedral facet and the damping coefficients for PF4 were feed into ARBD for multi-replica BD simulations. Our work employed 16 replicas of simulations in parallel. Each replica lasted for a simulation time of 2μs and simulated 25 copies of PF4 diffusing around the icosahedral facet. During the simulations, these 25 copies of PF4 were only allowed to interact with the icosahedral facet and did not interact

with one another. Thus, together, we performed 400 independent diffusion simulations with PF4. During each of these simulations, PF4 was allowed to bind to, or unbind, from the icosahedral facet. It is important to note that the residence time for each of these binding events is usually 2-3 order of magnitudes different compared with the real binding time. This is because the post-binding conformational changes of PF4, which often stabilize the interaction, are not sampled. Further, the simulations are performed in an implicit solvent environment, which is known to accelerate protein dynamics and diffusion, even in MD. Flexibility was simulated by applying a 3-dimensional normal distribution with a standard deviation of 2Å on each axis to each atom.

2.4 Results

2.4.1 The Structure of the ChAdOx1/ChAd-Y25 Viral Capsid

Determined at 3.07Å resolution, ChAdOx1 possesses the quintessential icosahedral adenovirus capsid structure (Fig. 2.2A). As in other adenovirus structures solved by single particle cryo-EM, local resolution is higher on the more ordered interior of the capsid while the flexible components on the capsids' exterior result in less resolved signal (Fig. 2.1). The asymmetric unit contains the expected penton monomer, one peripentonal, two secondary, and one tertiary hexon trimers, one peripentonal and one secondary copy of pVIII, and partial density for the pIIIa protein (Fig. 2.2B, C). The pentameric penton protein, located at the twelve 5-fold icosahedral vertices, had weaker signal (Fig. 2.2B, C), which could indicate a less well-ordered, or less stably interacting, protein than those observed in previous cryo-EM structures of HAdV-D26 and HAdV-C5. As in other reported structures, the penton RGD loop (residues 305-335), which, is responsible for binding to integrins following attachment to the cell surface via the fiber-knob protein, was left unmodelled due to a lack of signal, indicative of its flexibility. pVIII (Fig. 2.2C)

was well resolved, barring residues 103-163, for which we observed no signal (Fig. 2.2E), in line with the observations of other groups[101, 102]. Partial density was observed for pIIIa, concentrated near the base of the penton (Fig. 2.2C). We observed partial densities for twelve copies of pVI in the base of the hexons which adopted two conformations, either wrapping around the hexon interior before extending into the capsid core, or extending directly out of the base of the hexon to wrap over the top of pVIII (Fig. 2.2C). Hexon was well resolved, including the hypervariable regions (HVRs) on the exterior (Fig. 2.2C), enabling a complete reconstruction. Reconstruction of the full capsid atomic model results in minimal clashes between asymmetric units and reconstructs a full icosahedral capsid (Fig. 2.2D). The trimeric fiber protein, consisting of a long flexible shaft terminating in the globular knob domain, was not modelled as only some poorly resolved portions of the shaft were visible, likely due to its flexibility (Fig. 2.1). Instead, the fiber-knob was solved by crystallography.

2.4.2 CAR is a High Affinity ChAdOx1 Fiber-knob Receptor

Adenovirus fiber-knob is responsible for the primary virus-cell interaction during infection. To investigate primary ChAdOx1 receptors we solved the structure of the ChAdOx1 fiber-knob receptor (Fig. 2.3A). Data from one crystal were used for the final structure analysis (Fig. 2.9A), showing P1 symmetry with cell dimensions a=98.427Å, b=112.26Å, c=98.605Å, β=92.6°. Diffraction data were scaled and merged at 1.59Å resolution. The fiber-knob shows the expected three monomers assembling into a homotrimer with 3-fold symmetry (Fig. 2.3A), packed into an asymmetric unit containing 4 trimeric copies (Fig. 2.10B). The electron density map was of sufficient quality to determine side chain conformations throughout most of the structure (Fig. 2.9C-D). Super-positioning of the previously reported structure of HAdV-C5 fiber-knob and our structure of the ChAdOx1 fiber-knob protein show that fold homology is high, despite

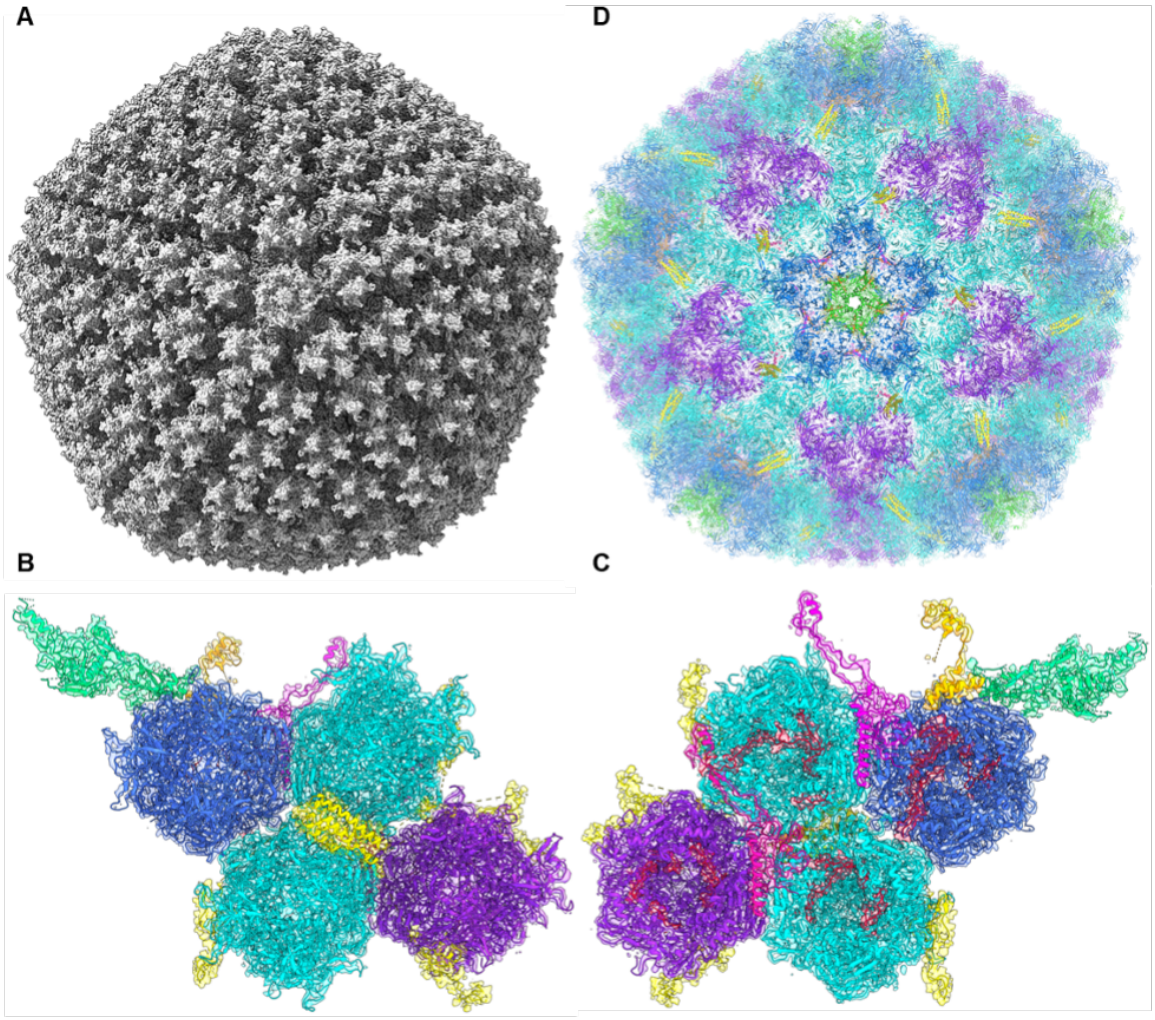

Figure 2.2: **Capsid structure of the ChAdOx1 viral vector.** CryoEM volume data for ChAdOx1 shows an archetypical adenovirus icosahedron (A) This volume resolved to show an asymmetric unit containing one penton copy (green), one trimeric peripentonal hexon (blue), two 2' hexons (cyan), one 3' hexon (purple), a 4-helix bundle corresponding to four copies of pIX (yellow), a peripentonal pVIII (magenta), a 2' pVIII (pink), partial density for a pIIIa protein (orange), and 6 copies of pVI (red), seen from the capsid exterior (B) and interior (C) in their associated volume. Repeating these asymmetric units with T25 icosahedral symmetry enables the reconstruction of a full ChAdOx1 capsid model (D).

only 64.86% amino acid sequence homology, including in the loops, with a root mean square deviation of 1.4Å (Fig. 2.3B). There is much lower homology between ChAdOx1 and HAdV-B35 fiber knob. The core fold is similar, but the loops are divergent (Fig.

2.3C). Using the structure of HAdV-D37 fiber-knob in complex with CAR as a template, we generated models of the ChAdOx1, HAdV-C5 (a CAR interacting adenovirus), and HAdV-B35 (a CD46 interacting adenovirus, which does not bind CAR) fiber-knobs, in complex with CAR (Fig. 2.10A-C). ChAdOx1 and HAdV-C5 were both predicted to form numerous polar contacts with CAR (Fig. 2.3D-E), with HAdV-B35 forming very few (Fig. 2.3F). Rosetta interface energy calculations supported these observations, suggesting the strongest CAR interaction was formed by HAdV-C5, followed by ChAdOx1, then HAdV-B35 fiber-knob (Fig. 2.3G). These calculations are in line with previous observations[165]. Mapping interacting residues back to the ChAdOx1 sequence shows several predicted CAR binding residues are shared with HAdV-D26 and HAdV-C5 fiber knobs (Fig. 2.3H). To validate these predicted CAR interactions, we performed surface plasmon resonance of ChAdOx1, HAdV-C5, and HAdV-B35 fiber-knob proteins binding CAR or CD46. This confirmed HAdV-C5 and ChAdOx1 fiber-knobs bind strongly to CAR, but not CD46. HAdV-B35 binds strongly to CD46. HAdV-C5 remains the strongest known CAR binding adenovirus with a KD of 0.06nM, with ChAdOx1 binding at 7.16nM; not as strong as HAdV-C5 due to a slower Ka. These results are summarized in figure 3A. Surface Plasmon Resonance traces are in extended figure 4A-C. We assessed if these three fiber-knobs bind CD46 and desmoglein 2 (DSG2). ChAdOx1 formed a weak interaction with CD46 with very fast on (ka) and off (kd) kinetics (Fig. 2.11E). We observed a weak interaction between HAdV-B35 and CAR, likely indicative of non-specific incidental interactions (Fig. 2.11F). We validated these finding in a cellular context using antibody inhibition assays in CHO-CAR cells, which express CAR but are negative for other known primary adenovirus receptors. HAdV-C5 showed the strongest CAR binding affinity (lowest IC50) followed by ChAdOx1.HAdV-B35 demonstrated weak CAR binding affinity (IC50 >1000X higher) (Fig. 2.4B). It is possible that very high HAdV-B35 fiber-knob protein concentrations give a false signal via non-specific CAR

interactions in both this, and the SPR experiments. A similar analysis in CHO-BC1 cells, expressing CD46-BC1 isoform but no other known primary adenovirus receptors, determined that HAdV-B35, had a strong CD46 interaction, while HAdV-C5and ChAdOx1 fiber-knobs did not have a measurable ability to prevent anti-CD46 antibody binding (Fig. 2.4C). These experiments, summarized in figure 3D, are robust evidence that ChAdOx1 uses CAR as a primary receptor, not CD46 or DSG2.

2.4.3 Charge Complementarity Facilitates a ChAdOx1 Complex with Platelet Factor 4

Recent reports indicate that ChAdOx1 may interact with PF4, which is involved in HIT which has a similar clinical presentation to TTS [140]. We used SPR to investigate whether PF4 can interact with highly pure preparations of adenovirus derived vaccine vectors Ad26, Ad5, ChAdOx1, or to the vaccine preparation of ChAdOx1, AZD1222. ChAdOx1, Ad5, and Ad26, were observed to bind to PF4 with affinities of 661nM, 789nM, and 301nM, respectively (Fig. 2.5). AZD1222 was observed to have a similar affinity to PF4 as the purified virus counterpart, with an affinity of 514nM (Fig. 2.6) Specificity of PF4 binding was confirmed by anti-PF4 antibody binding to the ChAdOx1/PF4 complex on the chip (Fig. 2.6A). This demonstrates the ability of antibodies to bind to PF4 while it remains in complex with ChAdOx1. We repeated the SPR experiments using different salt concentrations and observed a reduced PF4 binding with increasing salt, suggesting an electrostatic interaction (Fig. 2.6B). Continuum electrostatic surface potential calculations show the capsid of ChAdOx1 has an electronegative surface potential of <-1.5kBT across approximately 90% of its surface, interrupted in inter-hexon spaces occupied by pIX, where the surface potential rises to >-0.5KBT (Fig. 2.5C,13A). We compared the surface potential to that of HAdV-D26, which is also implicated in TTS. HAdV-D26 has an overall electronegative surface potential, but less strong than ChAdOx1 at <-1.0kBT. In contrast to ChAdOx1, we

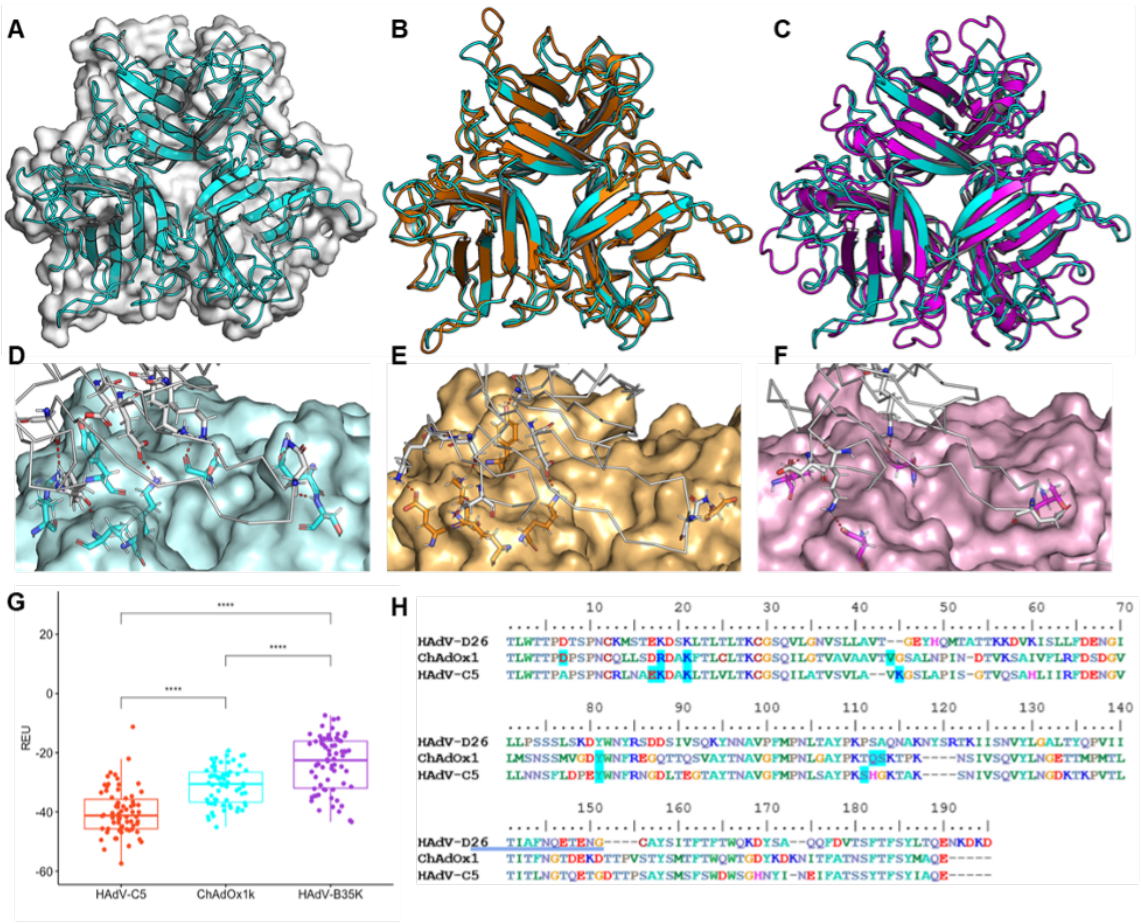

Figure 2.3: **ChAdOx1 and HAdV-C5 have tight homology and form CAR contacts.** The crystallographic structure of the ChAdOx1 fiber-knob (Cyan) shows the archetypical homotrimer (A) and aligns closely to the HAdV-C5 fiber-knob (orange) with an RMSD of 1.4Å (B), but does not closely align to the HAdV-B35 fiber-knob (purple, C). Homology models equilibrated by molecular dynamics show ChAdOx1 (D) and HAdV-C5 fiber knobs (E) form numerous polar contacts (red dashes) with CAR (white ribbon), though HAdV-B35 (F) forms few. Free energy calculations in Rosetta shows HAdV-C5 forms the strongest predicted interaction with CAR, followed by ChAdOx1, then HAdVoB35 (G). Mapping the predicted contact residues (blue highlight) in HAdV-C5 and ChAdOx1 to the clustalω aligned sequences shows similar contact residues are conserved in HAdV-D26 (H). ****<0.001

observe regions of positive potential, up to >+1.5kBT, recessed in the inter-hexon spaces (Fig. 2.6D, 2.13B). In both viruses the positive potential is driven by apical regions of

A

Analyte	Ligand	K_D (nM)	k_a (1/Ms)	K_d (1/s)
HAdV-C5	CAR	0.06±0.02	1.56±1.07x10^6	1.09±0.7x10^{-4}
HADV-B35	CD46	4.38±1.95	2.91±0.73x10^5	9.94±1.16x10^{-4}
ChAdOx1	CAR	7.16±1.92	3.03±0.13x10^4	1.8±0.41x10^{-4}

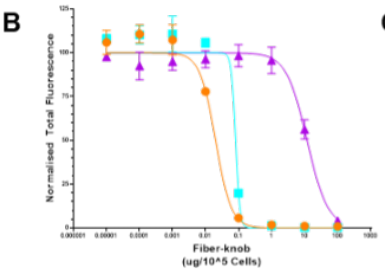

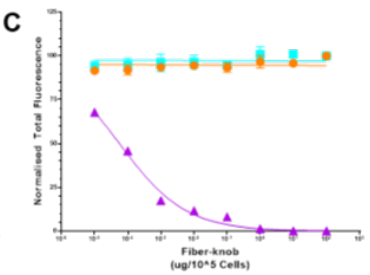

D

Adenovirus fiber knob species	CAR IC_{50} in CHO-CAR (μg/10^5 cells)	CD46 IC_{50} in CHO-BC1 (μg/10^5 cells)
HAdV-C5	0.01	NULL
HAdV-B35	11.86	5.56x10^{-5}
ChAdV-Y25/ChAdOX1	0.08	NULL

Figure 2.4: **hAdOx1 fiber-knob binds to CAR as a high affinity receptor.** Surface Plasmon resonance (SPR) experiments demonstrated HAdV-C5 and ChAdOx1 form high affinity interactions with coxsackie and adenovirus receptor (CAR), and HAdV-B35 forms high affinity interactions with CD46 (A). Antibody inhibition experiments on CHO-CAR (B) and (CD46-BC1 isoform expressing) CHO-BC1 (C) cells show HAdV-C5 (orange) and ChAdOx1 (cyan) bind CAR with high affinity but not CD46, while HAdV-B35 (purple) binds to CAR with very weak affinity and CD46 with high affinity (D).

adenovirus' major capsid protein, hexon, which we calculated to be most negative in ChAdOx1, followed by HAdV-C5, then HAdV-D26 (Fig. 2.13C). We also observed that PF4 has a strong electropositive surface potential (Fig. 2.6D). These observations are consistent with an electrostatic mechanism of interaction between ChAdOx1 and PF4.

2.4.4 PF4 Binds to ChAdOx1 in the Inter-hexon Space

To investigate a potential binding mechanism, we performed Brownian Dynamics simulations of PF4 with the ChAdOx1 or HAdV-D26 capsid structure. Results show freely diffusing PF4 frequently contacts the capsid surface of ChAdOx1 between the hexons, most commonly at the interfaces of 3 hexons where negative charge is concentrated, and the inter-hexon space is maximized (Fig. 2.7A). HAdV-D26 also forms contacts with PF4, but less frequently (Fig. 2.7B). These simulations represent possible

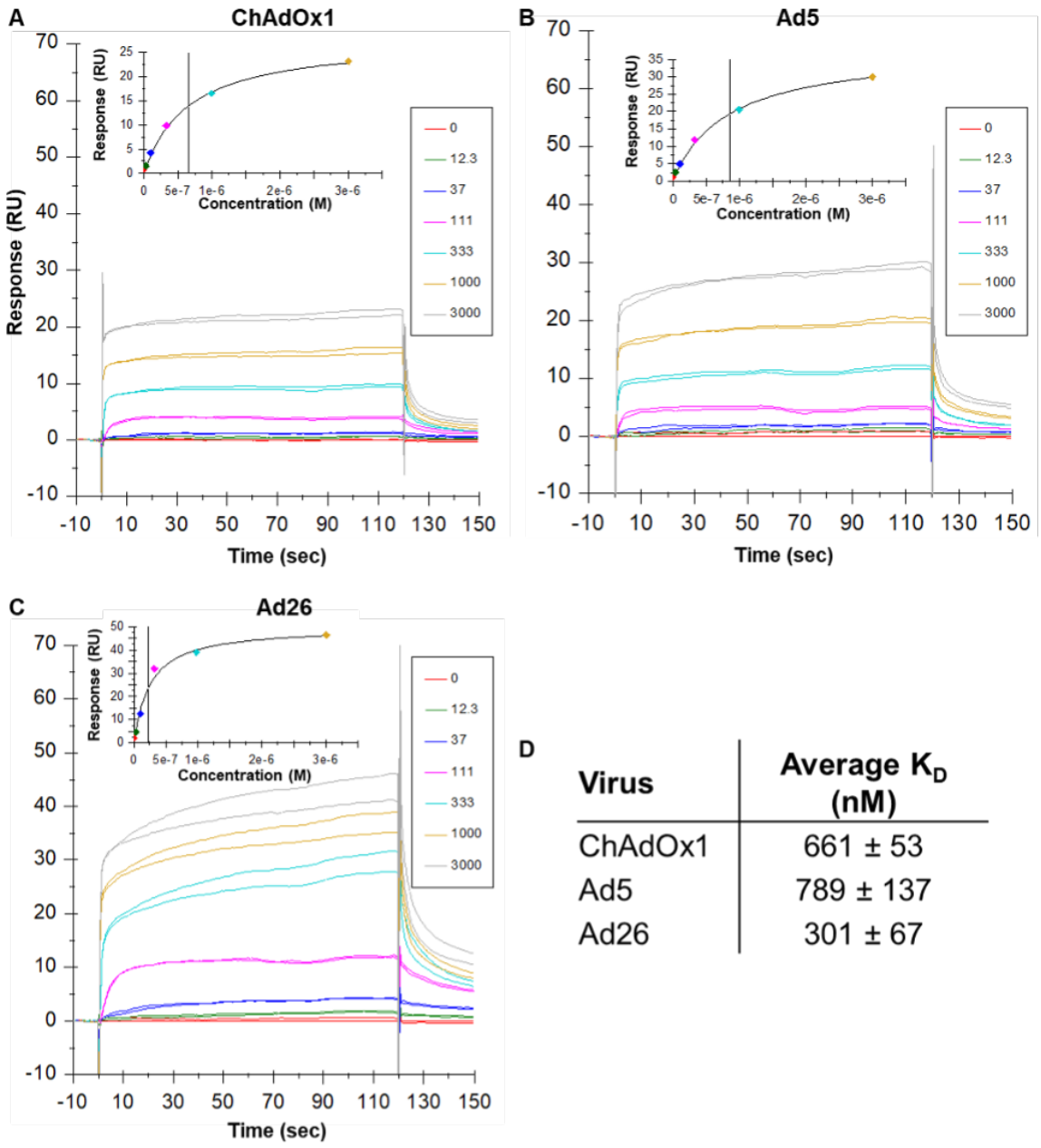

D

Virus	Average K_D (nM)
ChAdOx1	661 ± 53
Ad5	789 ± 137
Ad26	301 ± 67

Figure 2.5: **Clinical adenoviruses bind to PF4 with nM affinity.** Single injection SPR experiments show ChAdOx1 (A) Ad5 (B) and Ad26 (C) form stable, reproducible, interactions with PF4. Affinity was calculated using the steady state model (D) and the curve showed close fit to the tested concentrations (inset figures).

binding initiation events should not be used to interpret relative affinity of interactions. Analysis of an exemplar ChAdOx1/PF4 binding event at the 3-fold hexon interface shows

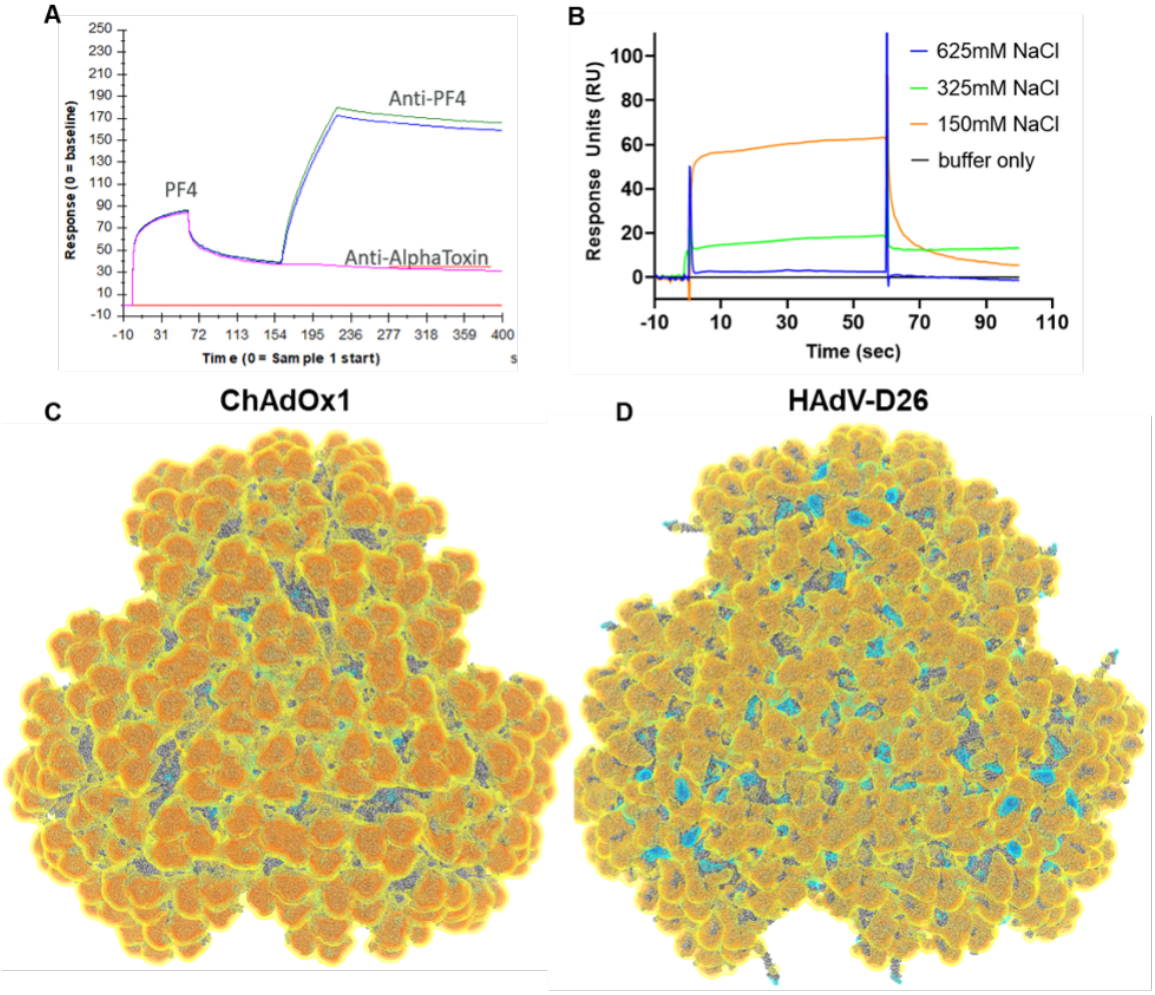

Figure 2.6: **ChAdOx1 creates a stable complex with PF4 and is highly electronegative.** A two injection SPR experiment showed that following PF4 binding to the ChAdOx1 capsid a polyclonal αPF4 was able to bind to the surface of the chip indicating a ChAdOx1/PF4/antibody complex (A). Similar SPR experiments show decreasing PF4 binding at increasing concentrations of NaCl (B). Visualization of the capsid (3-vertices shown) of ChAdOx1 (C) and Ad26 (D) show the electrostatic potential at -0.5KBT (yellow), -1.0KBT (orange), -1.5KBT (red), 0.5KBT (cyan), 1.0KBT (blue), and 1.5KBT (dark blue). Electronegative potential is focused at the apex of the hexons. ChAdOx1 is more electronegative than HAdV-D26 with negative charge extending into the inter-hexon spaces, while in HAdV-D26 has electropositive charge in these regions. A more detailed capsid view is available in extended figure 6.

the electropositive faces of PF4, occurring along its longest axis, oriented to face the electronegative potential of the surrounding hexons (Fig. 2.7C). To assess whether this orientation was a requirement for binding we performed a clustering analysis of the contacts in our simulation. The analysis indicates PF4 is similarly orientated to the example in Figure 6C in all contact instances (Fig. 2.7D). This common binding pose supports the idea that the ChAdOx1/PF4 interaction has specific determinants. To identify amino acids which are potentially important for the ChAdOx1/PF4 interaction we calculated the frequency of contacts between PF4 and the ChAdOx1 hexons in Brownian Dynamics simulations. These indicate PF4 contacts residues in the hypervariable regions (HVRs) of ChAdOx1 (Fig. 2.7E-F). The HVRs face into the space between the hexons and are highly flexible, creating a fluctuating volume in the inter-hexon space (Fig. 2.7A-B).

2.4.5 ChAdOx1/PF4 Complex Formation is Inhibited by Heparin

Heparin is also a key component in the mechanism for HIT, binding to multiple copies of PF4 and forming aggregates with anti-PF4 antibodies which stimulate platelet activation via FcγRIIa. We performed SPR and brownian dynamics experiments to test what effect heparin binding to PF4 has on the ability of PF4 to bind ChAdOx1. In Brownian dynamics experiments we observed that PF4 in complex with fondaparinux, an anticoagulant drug composed of the PF4 binding heparin pentasaccharide, significantly reduced the number of binding initiation events with the ChAdOx1 capsid surface (Fig. 2.15A-C). In purified ChAdOx1, and the AZD1222 vaccine preparation, we observed PF4 binding to ChAdOx1 was strongly inhibited by pre-incubation with heparin (Fig. 2.8A, Fig. 2.14D). Continuum electrostatic calculations of PF4 and PF4 in complex with fondaparinux show the electronegative potential of PF4 is ablated in the presence of fondaparinux (Fig. 2.8B-C). We infer that this weakened electropositive potential may

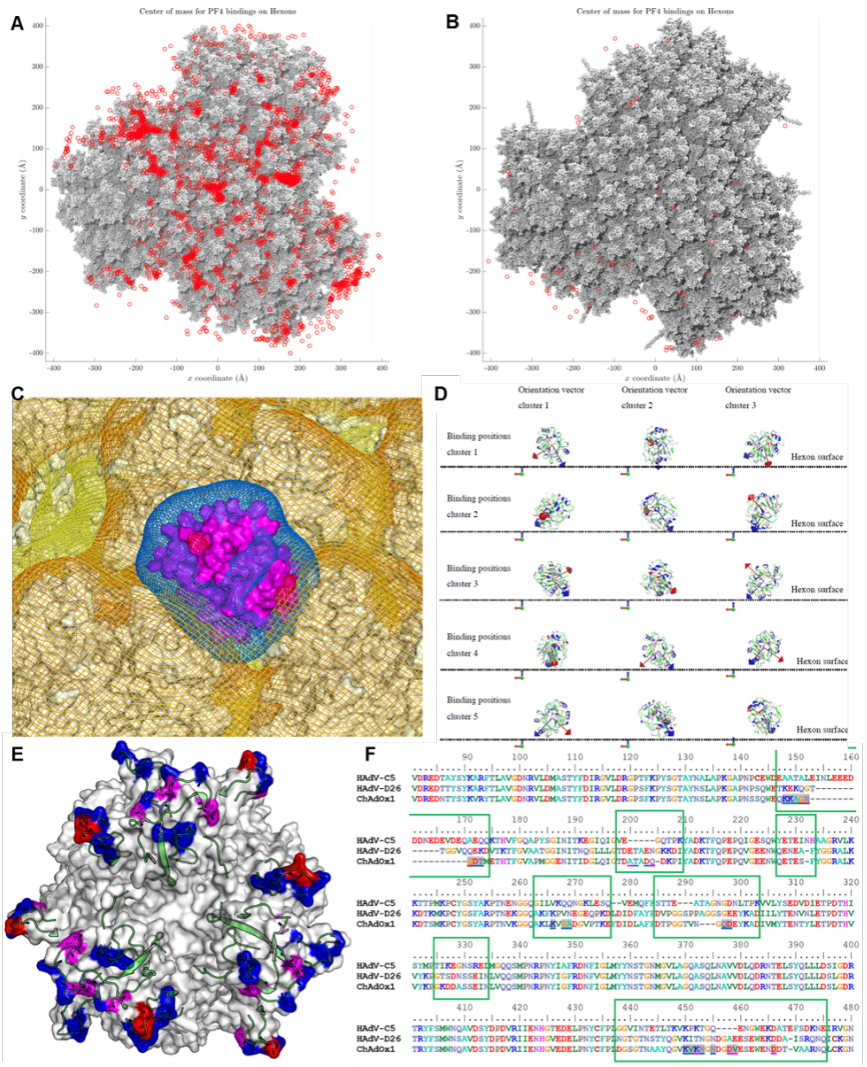

Figure 2.7: **PF4 binds to ChAdOx1 in the inter-hexon spaces more frequently than it binds to Ad26.** Brownian dynamics simulations of PF4 in solution with the facet show the locations at which PF4 makes contact with the facet (red spots) of ChAdOx1 (A) and Ad26 (B) showing the most common interaction locus is the space between 3 hexons, where the PF4 (purple) is observed to sink into the space between hexons exposing electropositive regions to the electronegative hexons (C). Analysis of PF4 binding events shows PF4 always forms contacts with ChAdOx1 oriented with its longest axis most normal to the plane of the hexon (D). Certain hexon residues are more commonly involved in the PF4 interaction (E), red residues interact >50% of the time, magenta >20%, blue 20-1%. All these residues are within the HVR loops (green cartoon). These residues are underlined in the sequence alignment with Ad26 and Ad5 contained in the green boxes indicating the HVR sequences (F). Charge map coloring is the same as figure 5.

reduce the ability of PF4 for form an electrostatic association with ChAdOx1.

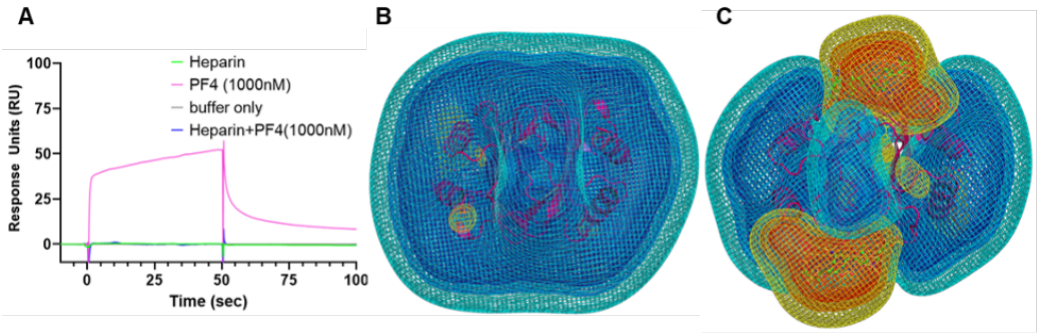

Figure 2.8: **The ChAdOx1/PF4 complex is inhibited by the presence of heparin.** SPR showed that preincubation of PF4 with heparin inhibits ability of PF4 to bind to ChAdOx1 (A). Calculations show that the highly electropositive charge on PF4 (purple, B), is disrupted in the presence of heparin as shown by the increase in electronegative potential when PF4 is complexed by fondaparinux, a heparin derived pentasaccharide (C). Charge map coloring is the same as figure 5.

2.5 Discussion

We have resolved the capsid structure of the ChAdOx1 viral vaccine vector to a resolution of 3.07Å, the highest reported resolution of an adenovirus capsid to date. We have characterized its primary cell attachment protein, the fiber-knob (Fig. 2.2-2.3) and show that ChAdOx1, a simian adenovirus, shares significant structural homology with human adenoviruses. We utilized our structural understanding and computational models to predict interactions between ChAdOx1 and host proteins. CAR is implicated in the transduction of host cells and is likely to be important for vaccine function. The other, PF4, contributes to pathogenesis in HIT and is hypothesized to be involved in TTS. We confirm CAR is a high-affinity receptor for ChAdOx1 fiber-knob protein (Fig. 2.3-2.4). Given the established ability of ChAdOx1 to infect human and chimpanzee cells, it follows that it uses a receptor which is conserved between these species. CAR is an example of this, as Human and Chimpanzee CAR proteins have identical amino acid sequences (Fig. 2.169)(1). To the best of our knowledge this is the first, verified, example of human and primate adenoviruses sharing a common adenovirus receptor protein, though cross species utilization of CAR has been observed previously, as human and canine adenoviruses both use CAR as a high-affinity cell entry receptor[160].

We demonstrate ChAdOx1 fiber-knob does not bind CD46 or DSG2 (Fig3, S4). However, this does not preclude additional receptors. For example, HAdV-D37 and HAdV-D26 fiber-knob proteins bind to both CAR and sialic acid bearing glycans[24, 170]. Conceivably, there could be other mechanisms of direct interaction between the cell and capsid surface, such as the hexon-CD46 interaction recently suggested for HAdV-D56, though it is unclear if this putative interaction would be sufficient for a productive infection in vivo[171]. CAR, predominantly expressed in epithelial tissues, is involved in junctional adhesion[172, 173]. It has also been observed

on the surface of human platelets, especially platelet aggregates, and erythrocytes[174, 175]. Therefore, it may be tempting to try to link the affinity of ChAdOx1 for CAR with platelet aggregation and TTS. However, previous studies demonstrate that adenovirus-platelet aggregates are rapidly trafficked to the liver where they are sequestered by Kupffer cells and degraded[176]. While it was possible to induce thrombocytopenia in mice following an intravenous dose of 1011VP/ml replication deficient adenoviral particles[143] (a dose 7,500X higher than that given, intramuscularly, in the ChAdOx1 nCoV-19 vaccine, assuming a 20g mouse, and a 75Kg human), this did not result in any thrombotic events. Another study in Rhesus Macaques observed the opposite effect, longer clotting times, presumably as a result of the diminished platelet count and/or depletion of circulating FX [177, 178]. Therefore, we believe it is unlikely that direct association between ChAdOx1 and platelets drives thrombotic events, regardless of their CAR expression status, in TTS. This study demonstrates binding between PF4 and ChAdOx1 under in vitro conditions, an interaction first suggested by Greinacher et al, and presents a mechanism by which it could occur [179]. SPR experiments demonstrate PF4 binds, with nM affinity, to highly pure CsCl gradient preparations of ChAdOx1 and the commercial ChAdOx1 nCoV-19 vaccine, AZD1222/Vaxzevria (Fig. 2.6,2.12). This confirms that the association between Vaxzevria and PF4 is an interaction between the PF4 and ChAdOx1, rather than any cell-line derived proteins remaining in the vaccine following manufacture. We demonstrate that this interaction is not specific to ChAdOx1 and that PF4 forms interactions with Ad5 and Ad26 with similar affinity (Fig. 2.6). We also observed that heparin reduces the ability of PF4 to associate with ChAdOx1, suggesting this interaction is not stimulated by PF4/polyanion complexes (Fig. 2.7,2.15), which is concomitant with the finding that patients have not been treated with heparin prior to developing TTS[136]. Exploring the mechanism of this interaction, we demonstrate that PF4 frequently contacts

the surface of ChAdOx1 when allowed to diffuse freely in Brownian dynamics simulations (BD sims, Fig. 2.8A) and that these interactions are facilitated by electrostatic complementarity between the electropositive PF4 and electronegative ChAdOx1 capsid, matched with a shape complementarity that enables PF4 to enter the space between hexons (Fig. 2.6,7,13). The electrostatic nature of this interaction was further supported by SPR experiments in the presence of increasing salt concentrations (Fig. 2.6B). Amino acid contacts are most frequent in the HVR loops (Fig. 2.8E-F). Presently, it is unclear if the contacts represent a specific amino acid interaction or are a function of the flexible HVRs entering the inter-hexon space where PF4 most commonly binds (Fig. 2.15). Ad26 has also been implicated in TTS at a similar frequency to ChAdOx1 on a per dose basis [138, 180]. Using a previously published model of Ad26 [101] we performed simulations as for ChAdOx1 and observed PF4 contacted Ad26 less frequently than ChAdOx1 (Fig. 2.7A-B). However, it is important to acknowledge that Brownian dynamics does not account for flexibility of the proteins following the initial interaction and operates on an accelerated timescale. Therefore, no inferences can be made regarding the protein's residency times and whether a stable complex is formed. This should be explored in future molecular dynamics simulations. Current evidence indicates that TTS presents similarly to heparin-induced thrombocytopenia (HIT), a condition where patients present with blood clots following administration of the thromboprophylactic drug, heparin[85]. This condition appears to be driven by anti-PF4 auto-antibodies of sufficient affinity to cluster PF4 and create a multivalent, presumably higher avidity, interaction between the antibody Fc-domains and FcγRIIa on the platelet surface, stimulating the platelet to release additional PF4. In the context of heparin, PF4 undergoes a conformational change facilitating the binding of more common, lower affinity antibodies specific to the PF4-polyanion complex. This creates a positive feedback loop as antibodies bind to increasing copies of PF4, stimulating further platelet activation, culminating in the

activation of the clotting cascade. This mechanism is described in detail by Nguyen et al[181]. To further summarize: whether anti-PF4 auto-antibodies induce thrombosis, or not, is a function of concentration and antibody affinity for PF4. Recent case reports show that most patients presenting with TTS (>90%) tested positive for αPF4 antibodies, however incomplete medical history limits understanding of predisposing factors[136]. Unlike those observed in HIT, anti-PF4 antibodies observed in TTS patients were predominantly of the sub-group which could bind to PF4 alone, rather than the PF4-heparin complex[179]. A ChAdOx1/PF4 complex could induce anti-PF4 auto-antibodies. In this potential mechanism, small quantities of ChAdOx1 enter the blood through minor capillary injuries caused by the intramuscular injection, as has previously been observed[182]. A ChAdOx1/PF4 complex could then form (Fig. 2.6-2.8), either independently or in association with platelets [183], and travel to the lymphatic system, transported by monocytes. Alternatively, PF4 released at the site of injection may complex the vector and drain directly to the lymphatic system. These virus/PF4 complexes may stimulate pre-existing anti-PF4 memory B-cells to differentiate into plasma cells, secreting anti-PF4 antibodies, which generally takes 4-8 days[184].

It is notable that TTS is much less frequently observed following the second dose of ChAdOx1, suggesting that, as in HIT, αPF4 IgG is not long lasting, and that any plausible mechanism should be prominent in the first but not second dose [138, 185]. Studies are needed to confirm whether adenovirus/PF4 complexes can induce thrombosis in the presence of anti-PF4 antibodies in vivo. This proposal goes some way towards explaining why TTS is so rare, requiring a series of low frequency stochastic interactions, first between small numbers of adenovirus particles entering the blood/lymph, then monocytes and/or B-cells, in rare patients predisposed towards the generation of anti-PF4 antibodies. In contrast to a previous proposal, we do not suggest EDTA, or residual HEK293 proteins, in the vaccine formulation contribute to TTS[135]. EDTA is a component of the

ChAdOx1 nCoV-19 vaccine formulation, but is not present in the Ad26.SARS2.S vaccine, following which TTS has also been reported[135, 137, 139, 186]. We note TTS symptoms manifest 5-24 days following vaccination, corresponding to the timeline for a secondary antibody response[135]. If large immune complexes formed directly with components of the vaccine formulation it seems more likely they would lead to platelet activation and clot formation immediately following vaccination, rather than >5 days later. The discussion surrounding potential mechanisms for TTS has recently been reviewed[141]. Current World Health Organisation clinical guidance advises against the use of heparin in the treatment of TTS, presumably based upon the similar clinical presentation of TTS and HIT[187]. Though our data suggest that heparin may inhibit the proposed interaction between ChAdOx1 and PF4 it does not provide any insights as to the effect of heparin on patients after they develop symptoms or its behavior in the wider biological context. Therefore, it is important to continue to adhere to current clinical guidance pending further studies of the role of heparin in TTS. The ChAdOx1/PF4 interaction described in this study suggests potential mechanisms by which safer viral vectors might be engineered by ablating this interaction. 'HVR swaps' have been performed with the goal of reducing recognition of adenovirus vector by neutralizing antibodies[66, 188]. Similar rational capsid engineering could eliminate electronegative residues in the HVRs, although a threshold below which the electronegative charge needs to be reduced has yet to be determined. Alternatively, upon determining key binding residues, a more specific approach could be envisaged where critical amino acids forming contacts with PF4 are removed or substituted. Therefore, modification of the ChAdOx1 hexon HVRs to reduce their electronegativity may solve two problems simultaneously: reduce the propensity to cause TTS and reduce the levels of anti-vector immunity, thus helping to maximize the opportunity to induce robust immune responses. Further exploration of adenovirus phylogenetic diversity may yield novel vectors with lower PF4

binding propensity and altered safety profiles. No currently proposed mechanism for TTS following vaccination is consistent with all the observed data. This is partly due to an incomplete clinical picture, a consequence of its rarity, consequently weak statistical data from which to draw inferences, and a lack of understanding about this novel interaction. Future work will focus upon clarifying if the adenovirus/PF4 complex is inherently thrombogenic and, if so, what downstream interactions lead to this.

2.6 Personal Contributions

The work described above was a collaborative effort between 7 different institutions across several countries. I was directly responsible for working closely with my co-author in order to conceptualize experiments to solve the structure of ChAdOx1 and biochemically characterize PF4 interactions. I assisted in growing and purifying virus and was responsible for freezing grids and all downstream processing leading up to EM data collection. I also was in charge of processing all of the data and performed all tasks and troubleshooting in Relion associated with generating the EM map of the virus. I also worked closely with my co-author and members of the Singharoy lab as we iteratively improved the model and map through MDFF and altered mask parameters and map sharpening procedures. I also validated map and model quality in order to ensure that we have extracted the maximum amount of information from this dataset. I was initially also involved in MST and SPR experiments to characterize the protein interactions between PF4 and the ChAdOx1 virus capsid until AstraZeneca began collaborating with us and assumed those responsibilities. Finally, I assisted my co-author with writing and editing the manuscript and generating figures.

2.7 Outlook

2.7.1 Future Improvements to Structural Understanding of Adenoviruses

Symmetry missmatch and visible density corresponding to the fiber shaft

Because of the generous mask used to process data we always aired on the side of maximizing the data retained in the structural map instead of cutting out regions to drive resolution improvements. In doing so we observed a great deal of density which corresponds to the protruding virus fiber and knob structures. These components of the capsid structure have never before been solved by cryo-EM as a complete adenovirus assembly. While these densities are not well resolved enough to produce high resolution structural data, with more advanced processing, and especially in conjunction with MDFF protocols, techniques such as local refinement may overcome symmetry miss match issues caused by the trimer-pentamer interface between the fiber and the adenoviral penton protein, as seen in Abrishami et al. 2021 [189]. A structure which clearly resolves these regions could provide valuable insight into the interface between the penton and the fiber shaft and advance our understanding of poorly understood aspects of the adenoviral capsid structure.

2.7.2 Conclusions and Further Validation of Vaccine Induced TTS Mechanisms

While the mechanisms of vaccine induced TTS remain to be conclusively proven, we have elucidated a likely mechanism for the devastating symptoms observed in vaccine induced thrombocytic thrombocytopenia. We have solved the structure of ChAdOx1 (Chimpanzee adenovirus Y25) to the highest currently recorded resolution for an adenovirus in order to clarify the structurally significant capsid proteins, including hexon hyper-variable loops that contribute to the immunological advantages of this vector. We

have also conclusively shown PF4 binding to the adenovirus capsid and used computational simulations to predict likely hot-spots of PF4 interaction. While more research is needed to confirm this mechanism, our hypotheses are currently undergoing further testing to ascertain if potential solutions are readily available in order to produce an adenoviral vector with a more optimal safety profile. We are also interested in initiating collaborations with researchers that may be able to provide biological validation to our mechanism using a HIT mouse model [190, 191]. With these experiments the mechanisms we propose may be incorrect. Even so, our experiments revealed many other new questions about the promiscuity of interactions with the adenoviral capsid, which warrant further study and may be generally applicable to vectors used in vaccination and genetic engineering. In addition, the structural study of this capsid has opened up new methodological avenues of research, as computational methods used to build models into structures of this size have improved significantly. Protocols used in this study that robustly automate model building using MDFF and alchemical methods are currently under development for widespread use that will improve model quality of large multi-meric structures such as viral capsid dramatically, and overcome challenges like edge effects commonly observed when building models into asymmetric units of large, highly symmetric density maps.

2.8 Supporting Information

A

PDB Entry	7OP2
Data Collection	
Diamond Beamline	DLS-I03
Date	2021-04-24
Wavelength	0.97626
Crystal Data (figures in brackets refer to outer resolution shell)	
Crystallization Conditions	0.2 M CaCl2, 0.1 M Tris, pH 8.0, 20 % w/v PEG 6000
a,b,c (Å)	98.427, 112.26, 98.605
α=β=γ (°)	90.0, 92.61, 90.0
Space group	P 1 2$_1$ 1
Resolution (Å)	1.59 – 74.03
Outer shell	1.59-1.62
R-merge (%)	27.3 (365.2)
R-pim (%)	8.0 (103.1)
R-meas (%)	28.5 (379.7)
CC1/2	0.996 (0.334)
I / σ(I)	5.5 (0.4)
Completeness (%)	100 (100)
Multiplicity	12.7 (13.5)
Total Measurements	3,364,401 (193,086)
Unique Reflections	286,462 (14,263)
Wilson B-factor(Å^2)	14.6
Refinement Statistics	
Refined atoms	18,792
Protein atoms	17,316
Non-protein atoms	4
Water molecules	585
R-work reflections	271,539
R-free reflections	14,210
R-work/R-free (%)	22.4 / 24.4
rms deviations (target in brackets)	
Bond lengths (Å)	0.012 (0.013)
Bond Angles (°)	1.498 (1.656)
[1]Coordinate error	0.136
Mean B value (Å^2)	24.8
Ramachandran Statistics (PDB Validation)	
Favoured/allowed/Outliers	2143 / 84 / 4
%	96.0 / 4.0 / 0

* One crystal was used for determining each structure.
[1] Coordinate Estimated Standard Uncertainty in (Å), calculated based on maximum likelihood statistics.

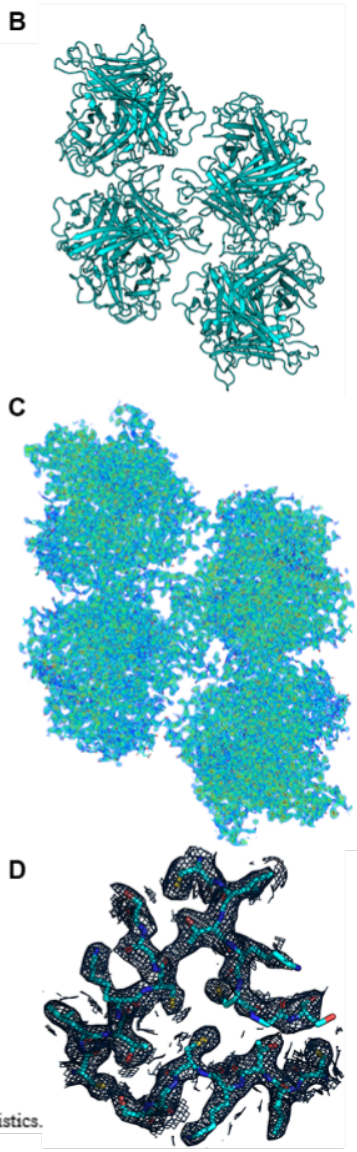

Figure 2.9: **Crystallization of ChAdOx1 fiber-knob protein results in 4 copies of the expected trimer per asymmetric unit and reveals side-chain locations.** Acceptable refinement statistics were achieved for the fiber-knob protein of ChAdOx1 (A). The crystal structure was solved with 12 copies of the monomer in the asymmetric unit, packing to form 3 trimeric biological assemblies (B). Density was sufficient to provide a complete structure in all copies (C, volume rendered in 0.5σ steps from red, 3.0σ, to dark blue), and was able to resolve side chain orientations reliably throughout the core fold (D, mesh shown at σ=1.0).

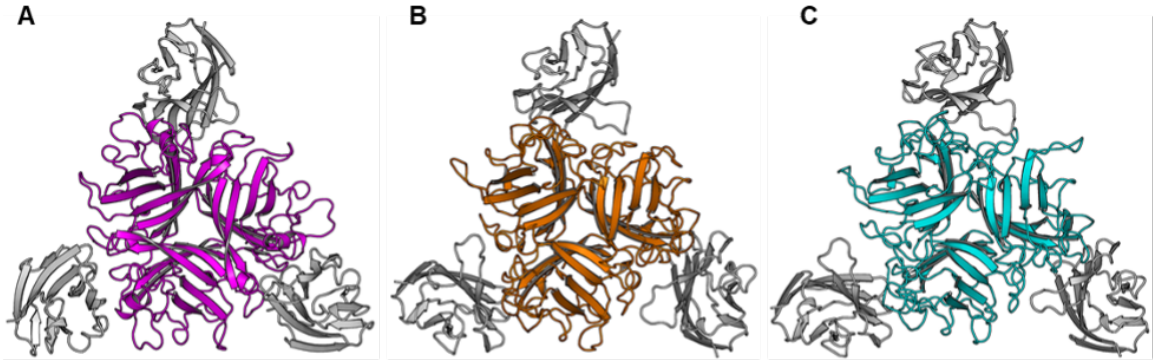

Figure 2.10: **Homology models of adenovirus fiber-knobs with CAR.** Using PDB 2J12 as a template the fiber-knob structures of HAdV-B35 (A, purple), HAdV-C5 (B, orange), and ChAdOx1 (C, cyan) were aligned with CAR (grey) in a potential binding pose and equilibrated by molecular dynamics.

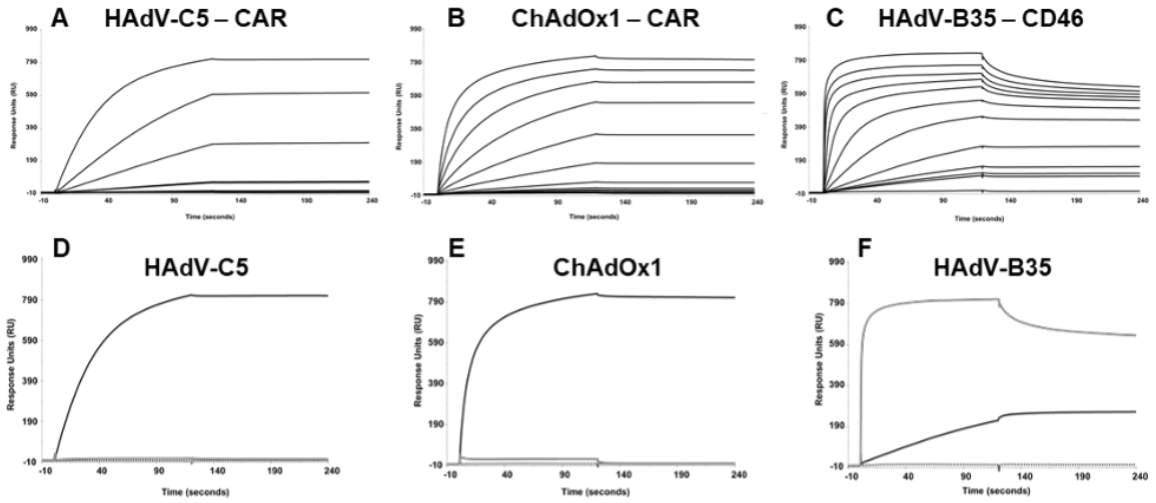

Figure 2.11: **Surface plasmon resonance traces show ChAdOx1 fiber-knob binds to CAR with high affinity but not CD46 or desmoglein 2.** Traces are shown as resonance units (RU) over time (seconds). Serial titration SPR shows HAdV-C5 (Titration=2.5-160nM) binds to CAR (KD=0.06±0.02nM, A) as does ChAdOx1 (Titration=2.5-2560nM, KD=7.16±1.92nM, B). HAdV-B35 (Titration=2.5-2560nM) binds to CD46 (KD=4.38±1.95nM, C). Further SPR experiments show HAdV-C5K (160nM) binds CAR (black), but not DSG2 (black, dashed) nor CD46 (grey, D). ChAdOX (2560nM) binds CAR (black), but not to DSG2 (black, dashed) and weakly interacts with CD46 (grey, E). HAdV-B35K (2560nM) binds CD46 (grey) and to a lesser degree to CAR (black) but not DSG2 (black dashed, F).

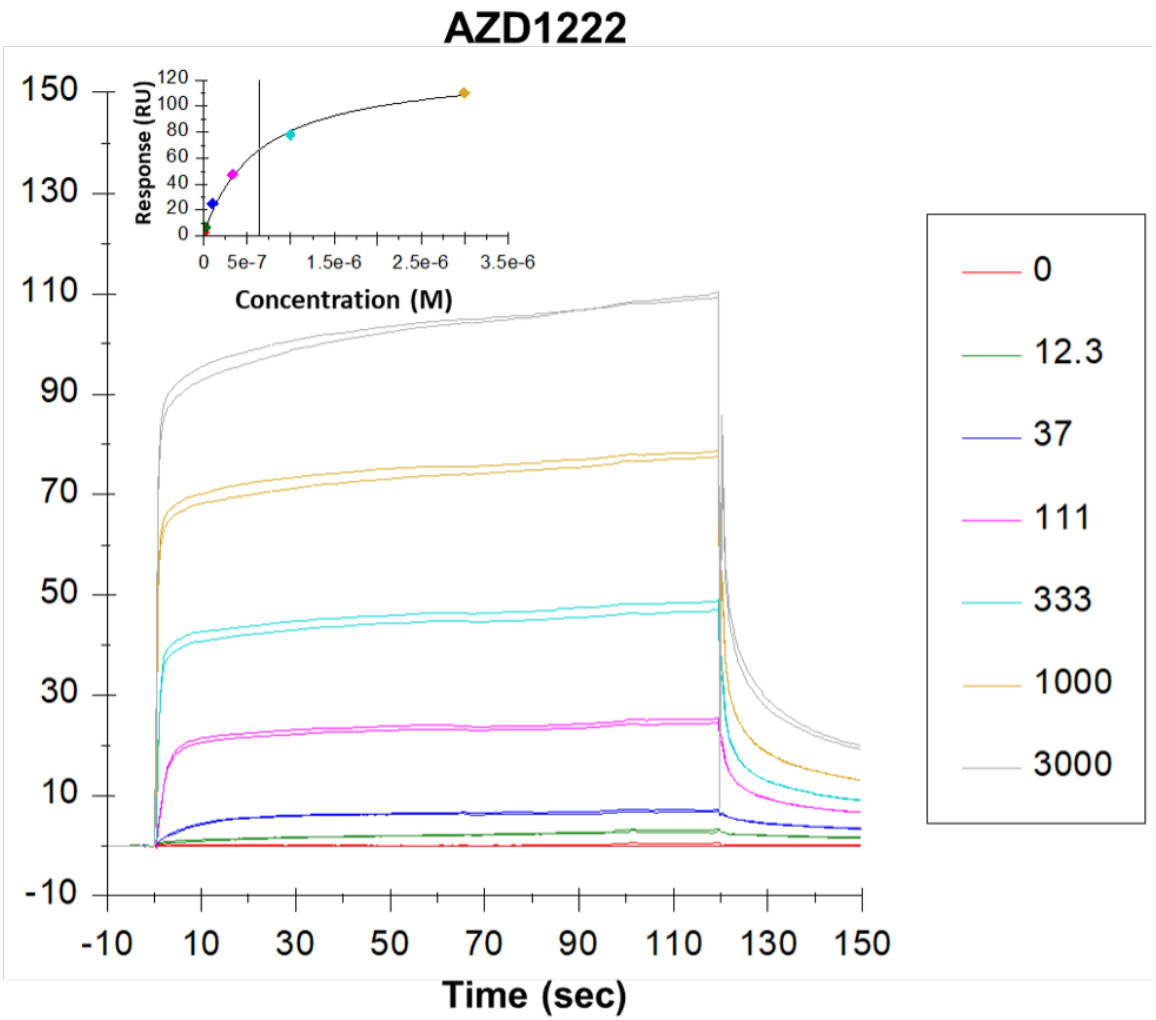

Figure 2.12: **The ChAdOx1 nCoV-19 vaccine preparation (AZD1222) binds to PF4 with high affinity.** Serial titration SPR at the indicated concentrations (nM, see legend) shows the ChAdOx1 nCoV-19 vaccine preparation binds to PF4 with affinity (KD= 514 ± 40 nM) comparable to that of CsCl purified adenoviruses as determined by the steady state model (inset figure).

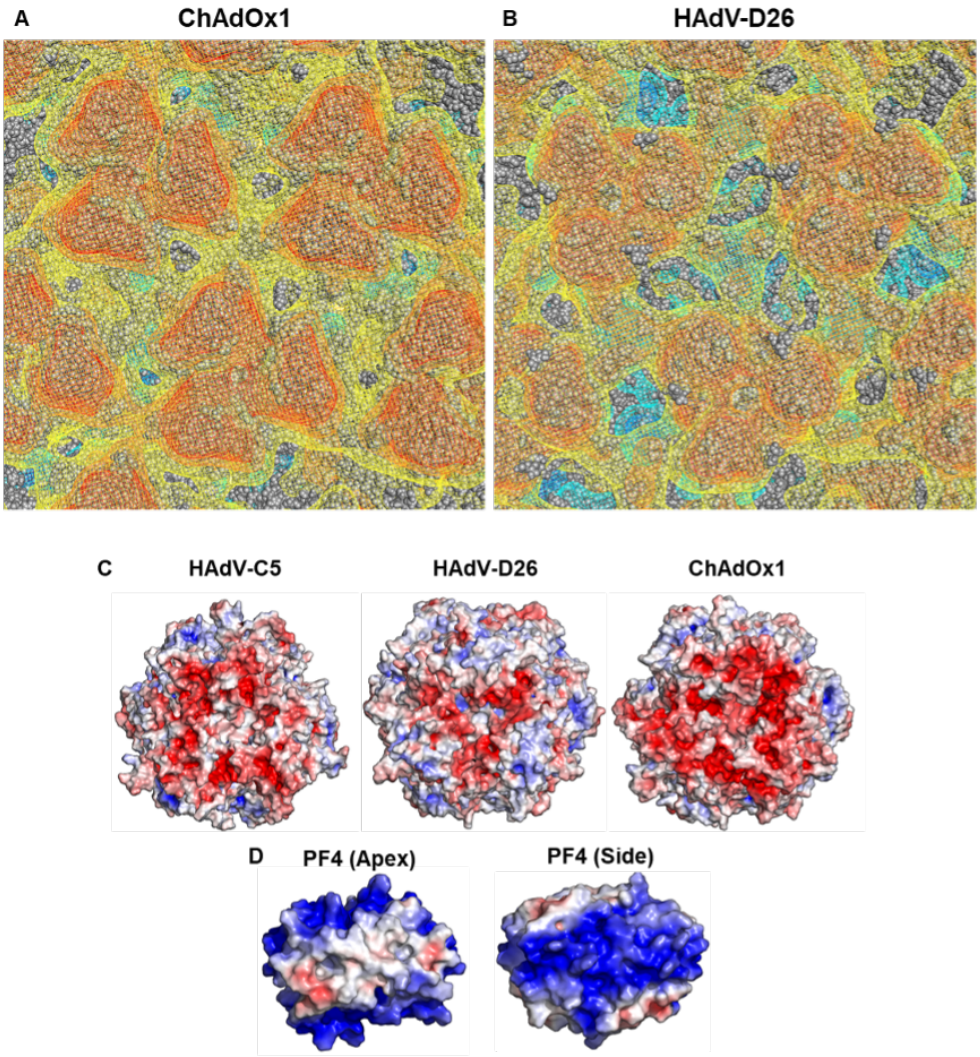

Figure 2.13: **ChAdOx1 is strongly electronegative, the opposite of PF4.** Close-up inspection of the electrostatic surface of ChAdOx1 (A) and HAdV-D26 (B) shows the strong electronegative potential emanating from the hexon apexes, with regions of electropositive potential in the space between hexons. The electronegative potential is substantily stronger in ChAdOx1, while the regions of electropositive potential are stronger in HAdV-D26. Visualisation in individual hexons shows how the apext of the trimer is electronegative around the apex of the 3 fold axis, and that the charge is strongest in ChAdOx1, followed by HAdV-C5, and weakest in HAdV-D26, with HAdV-D26 showing the strongest electropositive charges in the lateral regions (C). This contrasts with PF4, which has a strongly overall electropositive charge (D). Continuum electrostatic calculations are shown as a mesh from -0.5KBT (yellow), -1.0KBT (orange), -1.5KBT (red), 0.5KBT (cyan), 1.0KBT (blue), and 1.5KBT (dark blue). APBS is visualized on a +/-5.0eV ramp from blue to red.

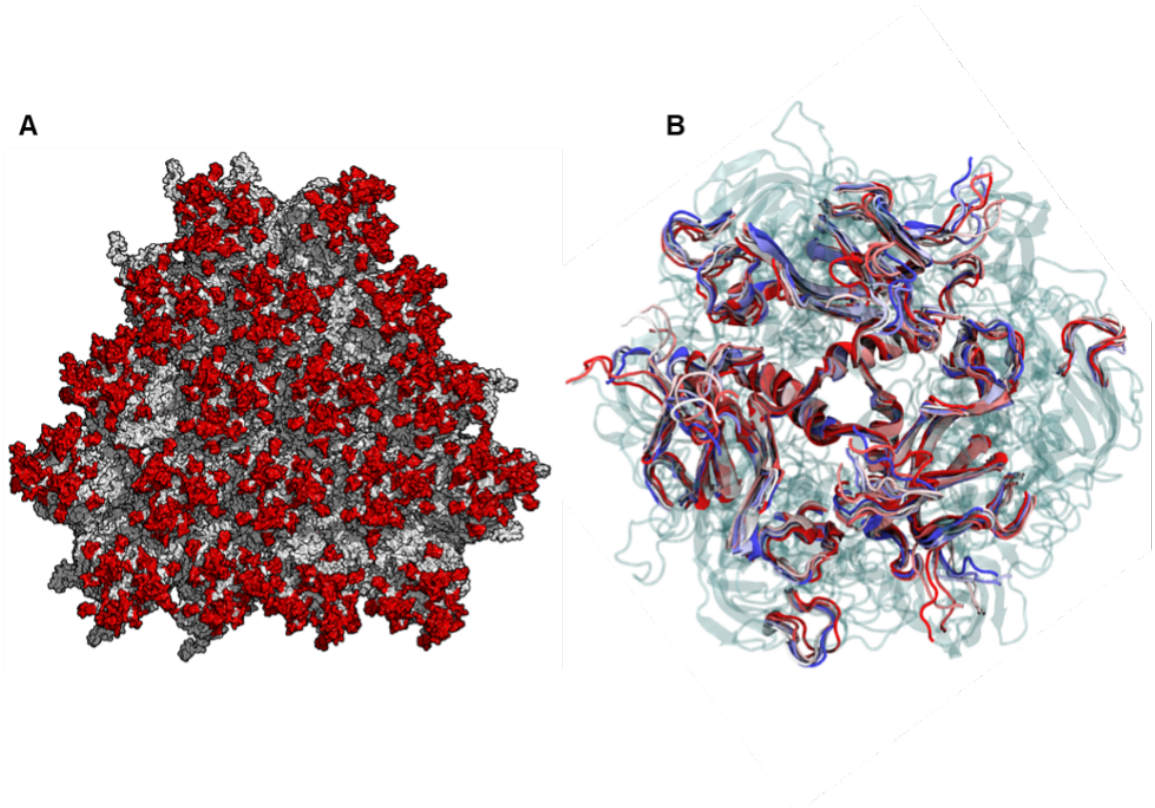

Figure 2.14: **The ChAdOx1 hexon HVRs face into the space between hexons and are highly flexible.** The hyper variable regions of the ChAdOx1 hexons (red) cluster about the apex and present into the space between hexons (A). Molecular dynamics simulations demonstrate that the HVRs are highly flexible (B, HVR positions are shown in full color).

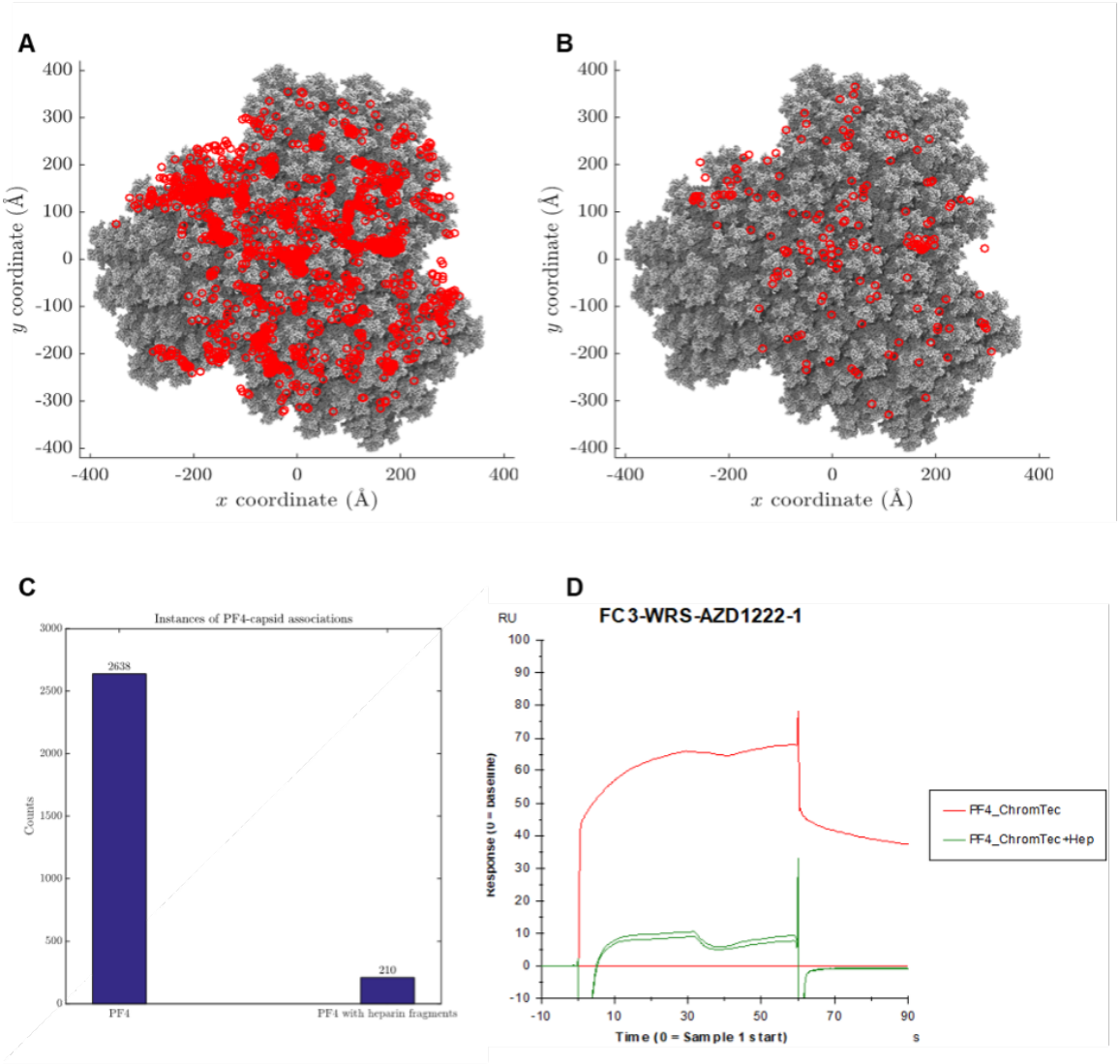

Figure 2.15: **The ChAdOx1 nCoV-19 vaccine preparation binds to PF4 with high affinity, but this interaction is weakened by the presence of heparin.** Brownian dynamics simulations show frequent interactions (red spots) between the PF4 tetramer and the ChAdOx1 surface (grey) (A). Similar simulations performed with the PF4-Fondaparinux (PDB 4R9W) showed the frequency of interactions reduced (B) by 12.56-fold (C). SPR shows that PF4 binds to the ChAdOx1 nCoV-19 vaccine preparation with high affinity (red), but when PF4 is preincubated with Heparin (green) this affinity is drastically reduced (D).

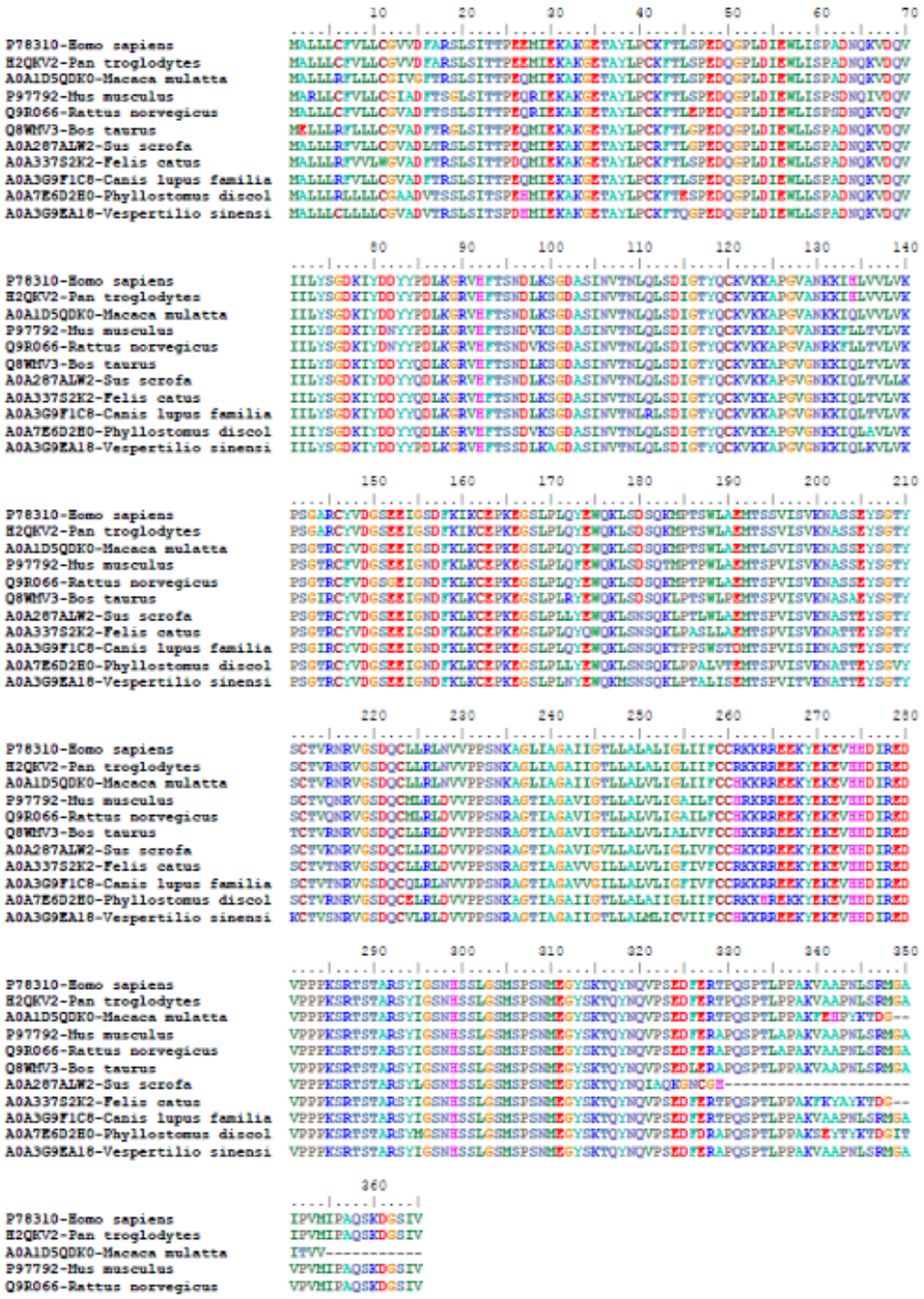

Figure 2.16: **CAR is a highly conserved protein across a range of scientifically important, domestic, and agriculturally significant species.** Humans (homo sapiens) and Chimpanzees (Pan Troglodytes) share a 100% sequence identity for their canonical CAR isoform. Sequences in this alignment taken from the indicted UniProt accession numbers.

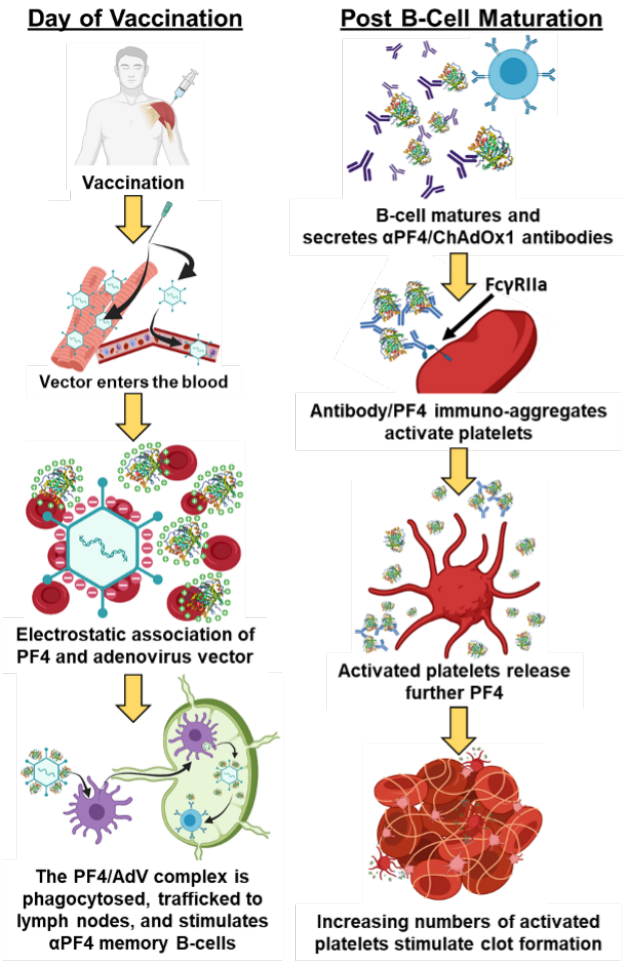

Figure 2.17: **Cartoon representation of a proposed mechanism by which ChAdOx1 association with PF4 might result in thrombosis with thrombocytopenia syndrome.** Following intramuscular vaccination with ChAdOx1 nCoV-19 small quantities of viral vector may enter the blood where they could interact with PF4 and form a complex through the mechanisms described in this study. This complex could also form at the injection site. This complex can then be taken up by monocytes and transported to, or drain directly into, the lymph nodes where it may stimulate the proliferation of pre-existing PF4 specific B-cells. After maturation of these B-cells, >5 days later, αPF4 IgG will be secreted which can form aggregates with PF4 circulating in the blood. These aggregates can stimulate activation of platelets by binding to FcγRIIa, stimulating further PF4 release. This could trigger a positive feedback loop culminating in clot formation and NETs, as in HIT.

Chapter 3

BIOCHEMICAL CHARACTERIZATION AND COMPUTATIONAL SIMULATION OF HUMAN SYX, A RHOGEF IMPLICATED IN GLIOBLASTOMA

Ryan J. Boyd, Tien L. Olson, James D. Zook, Manuel Aceves, Derek Stein, Wan-Hsin Lin, Felicia M. Craciunescu, Debra T. Hansen, Panos Z. Anastasiadis, Abhishek Singharoy, and Petra Fromme

3.1 Abstract

Structural discovery of guanine nucleotide exchange factor (GEF) protein complexes is likely to become increasingly relevant with the development of new therapeutics targeting small GTPases and development of new classes of small molecules that inhibit protein-protein interactions. Syx (also known as PLEKHG5 in humans) is a RhoA GEF implicated in the pathology of glioblastoma (GBM). Here we investigated protein expression and purification of ten different human Syx constructs and performed biophysical characterizations and computational studies that provide insights into why expression of this protein was previously intractable. We show that human Syx can be expressed and isolated and Syx is folded as observed by circular dichroism (CD) spectroscopy and actively binds to RhoA as determined by co-elution during size exclusion chromatography (SEC). This characterization may provide critical insights into the expression and purification of other recalcitrant members of the large class of oncogenic — Diffuse B-cell lymphoma (Dbl) homology GEF proteins. In addition, we performed detailed homology modeling and molecular dynamics simulations on the surface of a physiologically realistic membrane. These simulations reveal novel insights into GEF activity and allosteric modulation by the plekstrin homology (PH) domain. These newly revealed interactions between the GEF PH domain and the membrane

embedded region of RhoA support previously unexplained experimental findings regarding the allosteric effects of the PH domain from numerous activity studies of Dbl homology GEF proteins. This work establishes new hypotheses for structural interactivity and allosteric signal modulation in Dbl homology RhoGEFs.

3.2 Introduction

Recent successes designing drugs to inhibit small GTPase based drivers of oncogenesis and advances in modulating protein-protein interactions with structurally guided drug design have inspired renewed interest in characterizing the prolific family of small GTPase activating guanine exchange factor (GEF) proteins with the hope of establishing a new class of drug targets against this expansive class of potential oncogenes [192]. These proteins are responsible for modulating a diverse array of cell processes. Diffuse B-cell lymphoma (Dbl) family guanine exchange factors (GEFs) are the largest family of GEFs, containing 71-members out of 82 total RhoGEFs in humans [118]. Dbl GEFs facilitate the activation of small GTPases. The mechanistic details of GEF interaction with small GTPases have been reviewed previously [193]. The tightly controlled activation and localization of the small GTPase RhoA is directly coupled to stress fiber formation, cell mobility, and proliferation pathways via the opposing effects of Rho Activated Kinase (ROCK) and Diaphanous Homologue (Dia) [194]. There is a three-fold higher prevalence of Rho activating GEFs (RhoGEFs) as compared to Rho GTPases (22 members in mammals) indicating that the GEFs are likely regulators of activation specificity for these pathways [113]. This is further corroborated by the fact that almost all GEF proteins have been shown to be tightly modulated by numerous mechanisms of inhibition or autoinhibition, suggesting that multiple layers of regulation acting on the GEF are needed for correct conditional flow of these signals within the cell [125, 133]. Aberrant activation of these signals can be oncogenic, therefore inhibitors to

RhoGEF proteins could be potential cancer therapeutics. Dbl family RhoGEFs are defined by two tandem domains—the DH-PH domains [195]. The 170-190 amino acid DH (Dbl homology) domain facilitates the exchange of guanine nucleotide bound within the small GTPase by structurally manipulating two "finger regions" that encapsulate the nucleotide binding pocket. Simultaneously, many GEFs also affect GDP binding with RhoA by moving a magnesium ion held in complex with Thr-37 and Thr-19 of RhoA out of its binding conformation with the phosphate groups of the RhoA-bound GDP [193] thereby reducing binding interactions. The approximately 120 amino acid pleckstrin homology (PH) domain is often responsible for binding phospho-inositide phosphate (PIP) lipid head groups at the inner leaflet of the cell membrane [196, 197]. In some cases, the PH domain allosterically activates the GEF activity of the protein or relieves autoinhibition [198–200]. While the mechanism and overall contribution of PH domain allostery are a matter of continuing study and vary in a protein dependent manner, it is quite clear that in general, GEFs are closely regulated in the cell and often have auto-inhibitory domains or are bound by other proteins to repress their activities when and where they are not intended to be active [201, 202]. This spatiotemporal control keeps GEFs from spuriously activating their corresponding small GTPases [203]. It is well established that spurious GEF activity and small GTPase activation are drivers of cell migration, cell proliferation and cancer progression [112, 204]. Dachsel et al. 2013 and others revealed that Syx is highly expressed in human glioma cells [131, 205]. Experimental depletion of Syx in U87 and U251 glioma cells disrupts cell polarity, resulting in a "fried egg" morphology that does not display chemotactic cell movement that is characteristic of cancer proliferation [206]. Notably, the inability of Syx depleted cells to migrate was rescued by the expression of exogenous Syx, but not by a Syx mutant with no GEF activity[131]. Additionally, depletion of Syx in conventional or patient-derived GBM cell lines inhibits GBM cell growth (unpublished observations). These results suggest that inhibition of Syx

activity may be a possible treatment modality for GBM, and therefore Syx warrants biophysical and structural characterization, to facilitate structurally guided drug design[124, 207]. Several structures of Dbl homology RhoGEF DH-PH domains have been solved previously, and GEF characterization methods have been established. In contrast, Syx is in a subgroup of Dbl homology GEFs that are largely uncharacterized outside of basic protein-protein interaction data and no structural information is yet available for this protein[118, 208]. Structural elucidation and drug screening efforts require production and purification of milligram quantities of monomeric protein. Failure to overcome protein expression and purification issues are the most common pitfall of structural characterization projects[209]. Here we report the first high yeild expression, and biophysical characterization of purified human RhoGEF Syx including characterization of RhoA binding activity of the Syx DH-PH domain, as well as computational analysis to support ongoing structural studies and drug design efforts.

3.3 Materials and Methods

3.3.1 Sequence Analysis and Homology Modeling

The full length Syx sequence (UniProt identifier: O94827-1, NCBI reference number: NM_020631.6) was analyzed with the iTASSER homology-modeling server (Table S1)[148] as well as PSIPRED[210], SERp[211], and XtalPred[212] servers. The resultant disorder prediction and structural information were used to guide where truncation would be most appropriate. Several truncation sequences were made based on designing constructs that contained the DH and PH domains but removed unordered regions that would interfere with structural studies. The patterns of truncations were also guided by sequence alignments with Rho GEF structures 1XCG, 1X86, and 3ODO (PDZRhoGEF, LARG, and P115-RhoGEF respectively). Sequences were aligned with the MAFFT server

using the L-INS-i method[213].

3.3.2 Model Building and Molecular Dynamics

Known RhoGEF-RhoA complex structures (1XCG, 1X86 , 2RGN, 4XH9, 4DON) were structurally aligned with the Syx homology model to produce an initial Syx-RhoA model. This model was then repeatedly refined using Rosetta docking protocols[214, 215]. The resulting homology model of Syx was structurally aligned with several other known structures of PH domains and visually compared to structures containing bound lipid head groups to estimate the orientation of a potential lipid binding pocket on Syx[196, 216–218]. The Bio Chemical Library (BCL) software package was used to generate lipid headgroup conformers and Rosetta ligand docking protocols were used to place a $PI(4,5)P_2$ lipid into the putative binding pocket[219, 220]. The Orientations of Proteins in Membranes (OPM) server and CHARMM-GUI membrane builder were used to add a geranylgeranyl group to the tail of RhoA and then generate an all atom simulated membrane bilayer around the OPM generated lipid-protein interface, as well as place waters and NaCl ions throughout the box[221–223]. Parameter files for GDP, GTP, magnesium, POPC, $PI(4,5)P_2$, and geranylgeranyl groups were either generated by CGenFF or found in CHARMM36m params files. NAMD 2.14-CUDA utilizing the CHARMM36m force field was used to run a NPT simulations with 2 fs timesteps for approximately 1.2 microseconds after equilibration[169, 224, 225]. A temperature of 300˚K and 1 atm of pressure was maintained by a Langevin thermostat and barostat and electrostatics were calculated with the particle mesh Ewald method. All simulations were run on GTX1080 Nvidia GPUs until RMSD values reached equilibrium and visual observation confirmed that lipids were correctly oriented[155].

3.3.3 Dynamic Network Analysis

Dynamic network analysis was performed as described in Sethi et al. 2009[226]. Nodes were defined as Cα carbons, or phosphates. Community analysis of groups of residues that are most strongly interconnected was performed using the Girvan-Newman algorithm and visualized with VMD. Optimal path analysis was performed between several residues that clearly bind membrane lipids on both the PH and DH domain of Syx protein and residue Thr-37, located at the center of switch I region of RhoA.

3.3.4 Protein Engineering and Mutagenesis

CamSol analysis was performed by uploading the Syx homology model and sequence to the CamSol server[227]. The resulting prediction was encoded into the B-factor of the protein and visualized with PyMol. Mutants at these sites were either picked by hand or because they were scored favorably by the Rosetta design protocol[228].

3.3.5 Expression Optimization

Initial expression constructs containing several truncated versions of wild-type mouse Syx homologs were generated by the Anastasiadis lab. Chemo-competent BL21(DE3) cells (New England Biolabs) were transformed according to the manufacturer's instructions. A single resultant colony was isolated and then used to inoculate a 5 ml liquid culture containing TB containing 12g/L tryptone, 24g/L yeast extract, 4mL/L glycerol, 2.31 g/L KH_2PO_4 (17mM), 12.54 g/L K_2HPO_4 (72mM), with appropriate antibiotic[229]. Cell stocks were made by adding glycerol to 30% and stored at -80˚C. Starter cultures were inoculated by using a sterile pipette tip to transfer a small chunk of frozen glycerol stock into 1ml of pre-warmed TB. After overnight growth, this starter culture was visually checked for cell growth (with a desired OD600 of approximately 0.8)

and added to an autoclaved 250ml baffled flask containing 50ml of Terrific Broth (TB) and cells were allowed to grow at 37°C. IPTG was added to a final concentration of 0.5mM when the culture reached an OD600 of 0.8, and 1 ml aliquots were taken for analysis at desired time points. For subsequent SDS-PAGE analysis, aliquots were centrifuged at 17K x g and the supernatant was discarded. 10µl of cell pellet was mixed with 500µl 1X Laemmli buffer (Bio-Rad Cat 1610747) and stored at -20°C. Samples were incubated at 95°C for 5 minutes and spun down at 17K x g for 10 min to remove cell debris before analysis of raw supernatant was performed via SDS-PAGE using a 12% acrylamide-tris gel and subsequent overnight transfer to a Western blot PVDF membrane and visualization with an anti-His antibody (Qiagen Cat 34440, RRID:AB_2714179). Further optimization was done with His_6-TEV-$Syx_{393-792}$. This construct was transformed into BL21(DE3)(NEB), BL21(PlysS)(NEB), Lemo21(DE3) (NEB), BL21-AI(Invitrogen), KTD101(DE3), KJ740(DE3), C41(DE3), and C43(DE3) strains of E. coli cells. Strain KJ740 was obtained from the Yale E. coli Genetic Stock Center (CGSC), and the (DE3) lysogen was made using the λDE3 Lysogenization Kit 538 (EMD Millipore $69734-3$). Expression was performed as described above apart from chloramphenicol being used with Lemo strains. Trials with 1 and 2mM rhamnose were tested with the Lemo21(DE3) cells. For BL21-AI, arabinose at 0.2% final concentration was added along with IPTG at induction, and TB medium contained 0.1% glucose.

3.3.6 Cloning

Codon optimized constructs of the truncated versions of human Syx were designed and obtained from GenScript. Fusion constructs were generated as described previously[229] by cloning our codon optimized Syx gene into vectors containing the following tags that are cleavable with tobacco etch virus (TEV) protease: N-terminal His6 plus maltose binding protein (MBP; RRID:Addgene_29708); C-terminal MBP plus His6

(Addgene_37237); N-terminal His6 plus glutathione S-transferase (GST; RRID:Addgene_29707); N-terminal His6 plus small ubiquitin-like modifier (SUMO; RRID:Addgene_29711); or N-terminal His6 plus green fluorescent protein (GFP; RRID:Addgene_29716). Note that in the plasmid names for this clone the numbering of Syx residues was based on the Syx isoform from NCBI Reference Sequence NP_001036128.1. The sequence of this isoform is identical to the UniProt sequence O94827-1 used for the computational studies, aside from an additional 56 amino acids at the N-terminus of NP_001036128.1. All constructs were transformed into both BL21(DE3) and T7 Express lysY/Iq high competency E. coli (New England Biolabs C3013I). Ligation independent cloning was performed with the In-Fusion HD Cloning Plus system (Clontech 638910). Plasmid DNA was prepared with the QIAprep Spin Miniprep (QIAGEN 27106). DNA sequences were verified by Sanger sequencing at the DNA Laboratory core facility at Arizona State University or at GenScript.

3.3.7 Preparation Scale E. coli Expression

A 5ml overnight growth of the N-terminal His_6-MBP-TEV-$Syx_{393-792}$ (referred to as MBP-$Syx_{393-792}$ for brevity, or $Syx_{393-792}$ if referring to protein which has undergone TEV cleavage and MBP removal) construct in T7 Express lysY/Iq E. coli was visually checked for cell growth (OD600 of approximately 0.8) before being added to 1 L of pre-warmed TB containing 100ug/ml ampicillin. Cells were grown at 37°C and 300 rpm shaking to an OD600 of 0.8. The temperature was decreased to 25°C and IPTG was added to a final concentration of 0.4mM. Cells were allowed to grow for another 4 h before being spun down. Cell pellets were weighed and resuspended in 10ml Lysis Buffer A per 1 g of cells, and the resulting slurry was frozen at -80°C. Lysis Buffer A contained PBS (137mM NaCl, 2.7mM KCl, 10mM Na_2PO_4, 1.8mM KH_2PO_4, pH 8), 2mM dithiothretol (DTT), protein inhibitor cocktail (Roche cOmplete Ultra, Sigma part no.

5892791001), 1mM PMSF.

3.3.8 Purification of E. coli Derived MBP-Syx_393-792

Frozen cells were resuspended in 4˚C lysis buffer and 2mg/ml hen egg lysozyme (Sigma part no. 4403) and 0.2mg/ml bovine pancreas DNase (Sigma part no. $9003-98-9$) were added. The thawing cell slurry was sonicated on ice at 50% power for 1sec on, 2sec off, for 1min using a Branson 550 sonicator. The resulting slurry was centrifuged at $40,000rcf$ for 15min at 4˚C and then filtered through a 0.45µM filter before using a 150ml superloop connected to an AKTA FPLC in a 4˚C cold room to load protein at $0.5ml/min$ onto a 5ml amylose column (Cytiva Product no. 28918779). The column was previously equilibrated with buffer A (10mM Na_2PO_4, 1.8mM KH_2PO_4, pH 8, and 1mM TCEP). The protein was washed with 10 column volumes at 5ml/min and then eluted in 1ml fractions with buffer A plus 50mM maltose. Fractions with an absorbance peak at 280nm (combined volume of 20-25ml at a protein concentration of 1-5mg/ml) were concentrated to a volume of 500µl using a 30kD Molecular Weight Cut Off (MWCO) spin concentrator (Millipore part no. $UFC903096$) spun at 3000rcf, while visually ensuring there was no turbidity and mixing the solution every 5min with a pipette. The concentrated sample was injected onto a pre-equilibrated Superdex 200 Increase 30/100 GL column (Cytiva part no. 28990944) and run at $0.4ml/min$ at 4˚C with buffer A. Peaks were pooled and stored at 4˚C. The protein concentration and yeild was determined at this stage by absorbance at 280nm(A_{280}), using a molar extinction coefficient of 112,355 M-1cm-1 for the MBP-$Syx_{393-792}$ fusion construct. SDS-PAGE gels were run on all fractions and stained with Coomassie to ascertain purity.

3.3.9 TEV Cleavage and Negative Purification

The fractions containing purified protein at the expected molecular weight as determined by Coomassie stained SDS-PAGE gel were cleaved with TEV protease by

incubating a 10:1 ratio of protein and TEV mixture overnight at 4°C in buffer A. This mix was then incubated with 3ml of nickel NTA slurry for 20min to remove the His tagged MBP and TEV. Flow-through and subsequent washes were collected and concentrated using a 30kDa Molecular Weight Cut Off (MWCO) spin concentrator (Millipore part no. UFC903096). Protein concentrations were confirmed with A_{280} measurements after each interval with a molar extinction coefficient of $39880M - 1cm - 1$ for the cleaved $Syx_{393-792}$. Presence of the correct protein species was confirmed routinely with western blot. RhoA ($1mg/ml$) and anti-Syx antibody were blotted directly on PVDF as control before blocking with BSA (Figure 3.18). Anti-Syx antibody (Proteintech Cat $19830 - 1 - AP$, RRID:$AB_10858324$) (8ul in 10ml of TBST) was used in conjunction with a goat anti-rabbit antibody (Jackson ImmunoResearch cat $111 - 035 - 003$. RRID: $AB_2313567$) for visualization.

3.3.10 Preparation Scale SF9 Expression

3.3.11 Purification of SF9 Derived MBP-$Syx_{393-792}$ with on Column Cleavage

Frozen cells were re-suspended in 4˚C lysis buffer containing 10mM Na_2PO_4, 1.8mM KH_2PO_4, pH 8, and 2mM DTT, 0.2mg/ml bovine pancreas DNase (Sigma part no. $9003 - 98 - 9$) in a ratio of 7g cells to 20ml buffer. The thawing cell slurry was sonicated on ice at 30% power for 1sec on, 10sec off, for 30sec of ”on” time using a Branson 550 sonicator. The lysate was then dounce homoginized 8 times in a 50ml homogenizer. The resulting slurry was centrifuged at 100,000rcf for 15min at 4˚C and then filtered through a 0.45µM filter before using a 150ml superloop connected to an AKTA FPLC in a 4˚C cold room to load protein at 0.5ml/min onto a 5ml amylose column (Cytiva Product no. 28918779). The column was previously equilibrated with 3 column volumes of buffer A (10mM Na_2PO_4, 1.8mM KH_2PO_4, pH 8, and 1mM TCEP). The

protein was washed with 10 column volumes at 5ml/min. At this point the 5ml column was detached from the FPLC and 100ul of acTEV protease (Thermo cat no. 12575-015) was injected directly into the column using a 1ml syringe. The column was left at 4˚C overnight. The column was then linked in series to a 5ml HisTrap HP column (Cytiva product no. 17524801) and cleaved protein was washed through by running wash buffer at 5ml/min while collecting all flow-through peaks in 5ml fractions. Fractions of the flow-through with an absorbance peak at 280nm were concentrated to a volume of 500µl using a 30kD Molecular Weight Cut Off (MWCO) spin concentrator (Millipore part no. $UFC903096$) spun at 3000rcf, while visually ensuring there was no turbidity and mixing the solution every 5min with a pipette. This solution was stored at 4˚C until further purification could be performed by SEC. Both columns were recovered by washing with buffer A plus 50mM maltose and 400mM imidazole. The protein concentration and yeild was determined at this stage by A_280, using a molar extinction coefficient of 39,880 M-1cm-1 for $Syx_{393-792}$.

3.3.12 Size Exclusion Chromatography

The superdex 200 column was connected to the AKTA FPLC in the 4˚C cold room and equilibrated with at least 2 column volumes of sterile filtered water followed by at least 2 column volumes of containing 10mM Na_2PO_4, 1.8mM KH_2PO_4 pH 8, and 1mM TCEP buffer until the A_{280} and conductance traces appeared constant. Samples were spun down at 17,000g for 10min in a tabletop centrifuge at 4˚C before $500l$ of sample was injected onto the column and run at 0.4ml/min for the entire run. Fractions were collected at 1ml intervals over 1.5 column volumes. After each run, the column was re-equilibrated for 2 column volumes before the next run was initiated. A standard curve was run periodically to determine the elution volume which corresponded to the molecular radius of each protein (Cytiva part no. 28403842). Peaks eluting before 8ml were considered to be in the void

volume of this column.

3.3.13 Dynamic Light Scattering

The monodispersity of the purified protein was ascertained with a Molecular Dimensions SpectroSize 302 DLS apparatus with a 785nm 60mW laser imaging of 2µl protein droplets suspended in a 24 well hanging drop plate. The DLS data were collected in 10 scans with 20min long scans each, and resultant data was examined by the cumulants method113. DLS based buffer screening was done by mixing 2ul of protein with 2ul of each well of the Hampton research buffer screen 1 and 2 kits (CAT NO: HR2-072, HR2-413) and incubated for one hour before testing with DLS.

3.3.14 RhoA Expression

RhoA plasmid (RRID:Addgene_73231) expressing the TEV cleavable N-terminal His_6-tagged soluble domain of RhoA including residues 1-184 (referred to as His_6-TEV-$RhoA_{1-184}$ or just RhoA unless otherwise stated) was transformed into Rosetta 2 BL21(DE3) cells and frozen as glycerol stocks that were used to inoculate 5ml overnight starter cultures grown overnight at 37˚C, 250rpm. 5ml overnight starter cultures were used to inoculate 2L baffled flasks containing 1L of TB media with antibiotic and allowed to grow at 37˚C until the culture reached an OD600 of 0.6–0.8. At this point 250mM IPTG was added, the temperature was turned down to 18˚C, and the culture was allowed to grow overnight. The resulting culture was spun down at 4000 rpm and the pellet weighed and frozen at -80˚C.

3.3.15 RhoA Purification

Critically, all buffers were supplemented with 50µM GDP (Sigma cat no. G7127) to maintain RhoA in a folded state. Seven grams of cells were homogenized with 80ml of

Lysis Buffer (Tris-HCl pH 8.0, 150mM NaCl, 2mM $MgCl_2$, 50µM GDP, 10% glycerol, 5mM imidazole, 1mM PMSF, 1 SIGMAFAST ETDA-free protease inhibitor coctail tab (Sigma sku S8830-20TAB), 2mg/mL lysozyme, 2mM TCEP). Cells were lysed via probe-sonication with a Branson 550 sonicator set to run in intervals of 1 sec on, 2 sec off for a total of 1 min at 50% power. Sonication was repeated 2 times before the lysate was spun down at 40000rcf for 20min at 4˚C. The resulting supernatant was passed through a 0.45µM syringe filter before the supernatant was added to a 150ml superloop attached to a GE Akta series FPLC running unicorn 7 software to automate the following protocol: The clarified supernatant was injected at 1ml/min onto a 5ml Ni-NTA column (Cytiva part no. 17524802) equilibrated with Wash Buffer (50mM Tris-HCl pH 8.0, 500mM NaCl, 2mM $MgCl_2$, 50µM GDP, 10% glycerol, 15mM imidazole, 2mM TCEP). The column was washed at 5ml/min with 10 column volumes of wash buffer before a linear gradient of Elution buffer (50mM Tris-HCl pH 8.0, 300mM NaCl, 2mM $MgCl_2$, 50µM GDP, 10% Glycerol, 200mM Imidazole, 2mM TCEP) was used to elute the bound protein(49). Fractions of the elution step were collected and run on an SDS-PAGE gel before being stained with Coomassie to reveal fractions containing bands corresponding to the molecular weight of RhoA at 22kDa. Fractions were pooled and an A_{280} absorbance trace was measured using the elution buffer as a blank to estimate protein concentration and overall yield. The presence of His_6-TEV-$RhoA_{1-184}$ was also confirmed with Western blot using an anti-RhoA antibody (Thermo Fisher Scientific Cat MA1-134, RRID:AB_2536840).

3.3.16 RhoA – MBP-Syx$_{393-792}$ Complex Formation

Several methods for complex formation were tested to assess the most effective protocol for forming the MBP-$Syx_{393-792}$-RhoA complex to ascertain which produced the highest quality protein. The following protocols used Un-cleaved MBP-$Syx_{393-792}$ (unless

otherwise stated) incubated at 4˚C with un-cleaved His_6-TEV-$RhoA_{1-184}$ in a 1:2 ratio for 1 hour in all 5 trials. In "mix 1" (Figure 3.3A, purple trace), 10mM EDTA was added to the mixture to chelate magnesium out of the GDP binding site of RhoA. "mix 2" (Figure 3.3A, red trace) used cleaved $Syx_{393-792}$ (Figure 3.3B) mixed with RhoA, and also contained 10mM EDTA to chelate magnesium. "mix 3" (Figure 3.3, black trace) contained MBP-$Syx_{393-792}$ mixed with RhoA which was buffer exchanged 6 times in a 10k MWCO spin concentrator to remove all buffer containing GDP. In "mix 4" (Figure 3.3, light blue trace) an excess of ammonium sulfate was used to precipitate a protein mixture containing both MBP-$Syx_{393-792}$ and RhoA in order to to competitively force GDP out of the active site of RhoA and remove GDP containing buffer. For "mix 5" (Figure 3.3, grey trace) the process was the same as "mix 4" except that the ammonium sulfate precipitation was performed on RhoA alone, then MBP-$Syx_{393-792}$ protein solution was added to the RhoA. Each resulting solution was run on a Superdex 200 column as previously described. Controls show RhoA (Figure 3.3A, green trace), MBP-$Syx_{393-792}$ (Figure 3.3A, orange trace), and a molecular weight control (Figure 3.3A, dark blue trace).

3.3.17 Circular Dichroism

Cleaved $Syx_{393-792}$ was buffer exchanged 4 times into CD buffer (150mM sodium fluoride adjusted to pH 7.5 with 50mM monobasic and dibasic sodium phosphate) using a 15kDa MWCO Amicon spin column. The circular dichroism (CD) spectra were measured on a Jasco J-815 circular dichroism spectrophotometer scanning from 190-260 nm[230]. The resulting spectra were analyzed by the servers BeStSeL, K3D2, and DichroWeb's CDSSTR protocol using the SMP180 basis set[231–233]. Spectral analysis was compared to CD spectra of homology models and known protein structures with homology greater than 20% (Table 1) by back-calculating CD spectra with the PDB2CD server to check that the experiment accurately recapitulated secondary structure of the predicted folds seen in

the homology model[234].

3.3.18 Lipid Blots

Echelon PIP membranes were incubated with 20ml PBST-BSA blocking buffer (137mM NaCl, 2.7mM KCl, 10mM Na_2PO_4, 1.8mM KH_2PO_4, pH 8, 0.1% (v/v) Tween-20, 1mg/ml BSA) for 1 hour. The membrane was then incubated with 0.5 µg/ml $Syx_{393-792}$ in PBST-BSA buffer for 1 hour. The protein solution was discarded and the membrane was washed 3 times for 5 minutes with PBST. The membrane was then incubated with 5ul of Qiagen 34660 mouse anti-HIS – 1:2500) in 20ml PBST-BSA for 1 hour, followed by another 3 wash steps with PBST for 5 minutes each. Finally, the membrane was washed with 10ul secondary antibody (in 20ml PBST-BSA) for 1 hour before washing another 4 times with PBST for 10 minutes. The blot was imaged using a based chemo-luminescent system using peroxide and luminol solutions from thermo (thermo 46640), and imaged with a GE Typhoon imager.

3.4 Results

3.4.1 Sequence Analyses Homology Modeling Guided Construct Optimization for Structural Studies

To assess which regions of Syx were most likely to be ordered and determine which domains were likely to be useful targets for structural discovery, a homology model and corresponding sequence analysis were performed. Sequence identity between Syx and the most homologous proteins that have solved structures indicated a sequence identity of approximately 25% (Figure 3.11). Homology modeling of Syx DH-PH fragments predictably produced a model largely similar to known homologous structures, however regions of the DH and PH domain have several stretches that were unable to be modeled

reliably as determined by their homology to known structures. Most notably a loop on the PH domain had no matching homology anywhere in the PDB (Figure 3.11). Interestingly, despite these regions not being well represented in the PDB, in a multiple sequence alignment (mapped onto a homology model for reference) these same regions were not highly divergent from known sequences the NCBI sequence database (Figure 3.20). Analyses of the full length Syx protein using iTASSER [235] and DISOPRED3 [236] showed that the regions flanking the DH and PH domain were predicted to contain intermittent regions of highly disordered loops and poly-glutamate stretches. These regions were predicted to be poor targets for structural discovery, therefore truncation of the wild type protein was warranted.

3.4.2 Expression Screens Generate Reliable Protein Production Conditions

HIS-tagged mouse Syx constructs received from the Anastasiadis lab contained Syx GEF domains with truncations over four residue ranges: 1) 290-799, 2) 290-748, 3) 406-799, 4) 406-748, as well as a GST-tagged full-length mouse Syx. Expression in E. coli was only observable for mouse construct $Syx_{406-799}$, which showed modest expression with several unwanted lower molecular weight bands for the mouse Syx protein (Figure 3.1, lane B). Screening of expression conditions revealed that peak protein levels were achieved within four hours of induction at 25°C. At this juncture a human homologue of the $Syx_{406-799}$ mouse construct we refer to as $Syx_{393-792}$ was optimized for expression in E. coli. Screening showed meager enhancement of expression, but more importantly it showed none of the unwanted lower molecular weight bands seen in the mouse construct (Figure 3.1, lane A (human optimized) vs. lane B (mouse native)). Marginal improvements in yield were achieved by using T7 Express lysY/Iq BL21(DE3) E. coli (NEB). We then aimed to further improve on the codon-optimized construct with the addition of various fusion proteins for enhanced solubility and purification (Figure

3.12). We also attempted small scale IMAC (Ion Metal Affinity Chromatography) purification, however, we were not able to recover any substantial amount of protein. When expression was screened on several fusion constructs, the N-terminal MBP-Syx fusion construct produced large quantities of protein which were clearly visible on a Coomassie stained SDS-PAGE gel at the correct molecular weight (Figure 3.13).

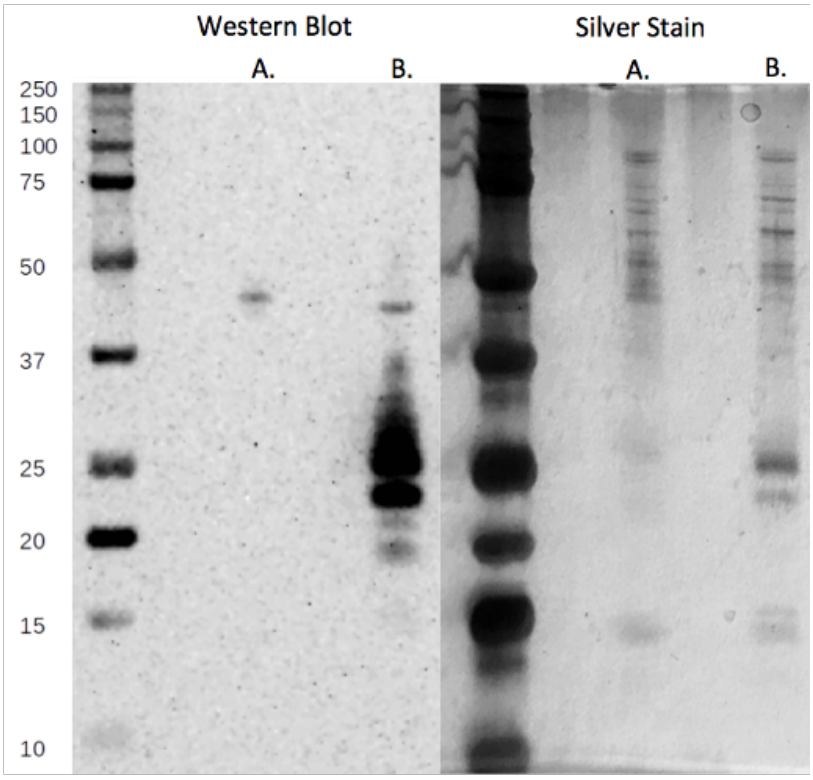

Figure 3.1: Comparison of expression of mouse $Syx_{406-799}$ and codon optimized human $Syx_{393-792}$ genes. Identical fractions were visualized with silver stain and western blot. (Lanes A. Human $Syx_{393-792}$: MW 48.3kDa. Lanes B. Mouse $Syx_{406-799}$: MW 46.6kD.)

3.4.3 Size Exclusion Chromatography Dynamic Light Scattering Reveal Pure, Milligram Quantities of MBP-$Syx_{393-792}$ with a Large Molecular Radius

Protein quality after expression was tested via size exclusion chromatography (SEC) and DLS. Purification of the MBP-$Syx_{393-792}$ via amylose column and SEC was confirmed

to be over 90% pure by Coomassie stained SDS-PAGE (Figure 3.13). Protein yields after amylose column were approximately 10 mg per liter of culture. DLS showed presence of an aggregate with a particle sized 17 nm and a polydispersity index (PDI) of 0.54 indicating a mixture of populations (Figure 3.18). All SEC runs with MBP-$Syx_{393-792}$ on a Superdex-200 increase 30/100 GL SEC column resulted in a large clearly visible peak eluting at or near the void volume of the column, around 8ml (Figure 3.2). This occurred regardless of changes in pH from pH 10 to pH 5, below which no protein was visible indicating that it had crashed out of solution. In addition, trials of numerous common buffer additives commonly used to reduce aggregation were not effective. These results are indicative of a soluble aggregate or very large homo-oligomer. The best conditions established ($10mM$ Na_2PO_4, $1.8mM$ KH_2PO_4, pH 8) were able to generate a very small peak corresponding to monomeric protein (MBP-$Syx_{393-792}$ control shown in orange Figure 3.3A). When the peak corresponding to the molecular radius of monomeric protein was isolated and re-run on the same SEC column, the result was a similar equilibrium of two peaks with the predominant population in the void volume. Solubility screening using Hampton detergent and additive screens were not successful at reducing the presence of the aggregate as measured by DLS.

3.4.4 RhoA – $Syx_{393-792}$ Complex Formation

Size exclusion chromatography was used to visualize peak shifts that indicate the formation of a protein-protein complex upon mixing MBP-$Syx_{393-792}$ or cleaved $Syx_{393-792}$ with RhoA. The $Syx_{393-792}$-RhoA complex was formed in several different trials to establish conditions which would produce a monodisperse complex suitable for structural studies. RhoGEF DH-PH domains are expected to have the highest affinity for RhoA when it has no nucleotide bound, therefore removal of GDP is likely necessary to drive complex formation with Syx. Most small GTPases are unstable in their apo form and quickly degrade without GDP or a GEF stabilizing them. This step was complicated

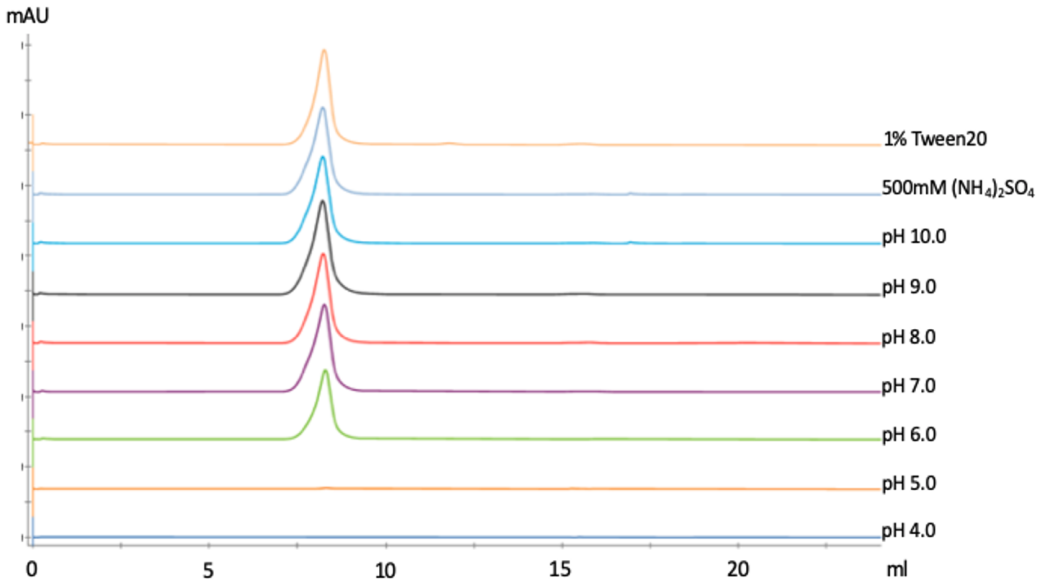

Figure 3.2: Screening of SEC buffer conditions did not produce monomeric MBP-$Syx_{393-792}$ as shown by SEC absorbance trace at 280nm. Each sample was from the same preperation of MBP-$Syx_{393-792}$ and differed only by the buffer additives indicated in the legend. Buffers all contained 500mM NaCl, and also contained the following buffers: pH 4-5: 20mM sodium acetate buffer, pH 6: 20mM sodium citrate, pH 7: 20mM sodium phosphate, pH 8: 20mM Tris, pH 9: 20mM glycine, and pH 10: 20mM CAPS buffers. 1% Tween20 and 500mM $(NH_4)_2SO_4$ respectively were both added to a base buffer of 20mM HEPES pH 7.5, 500mM NaCl in the case of the final two SEC runs.

by the high binding affinity of GDP with RhoA, which required optimization to find conditions which do not drive aggregation but still effectively remove GDP. The dashed line in each of the SEC traces in Figure 3.3A indicates absorbance at 260nm which is the absorbance peak for nucleotides like GDP while the solid line shows the absorbance at 280nm. peaks where the 260nm absorbance signal is greater than 280nm absorbance signal suggest the presence of lingering GDP. These data indicate that GDP appeared to be most effectively removed from RhoA by ammonium sulfate precipitation in the presence of Syx (Figure 3.3A, second trace from the top, shown in light blue). This condition also shows the largest peak shifted towards lower retention times, suggesting the presence of a complex which was larger than the control trace of Syx alone (Figure 3.3A,

orange trace). This was confirmed by SDS-PAGE analysis showing bands at the correct molecular weights for $Syx_{393-792}$ and RhoA in this fraction (Figure 3.4).

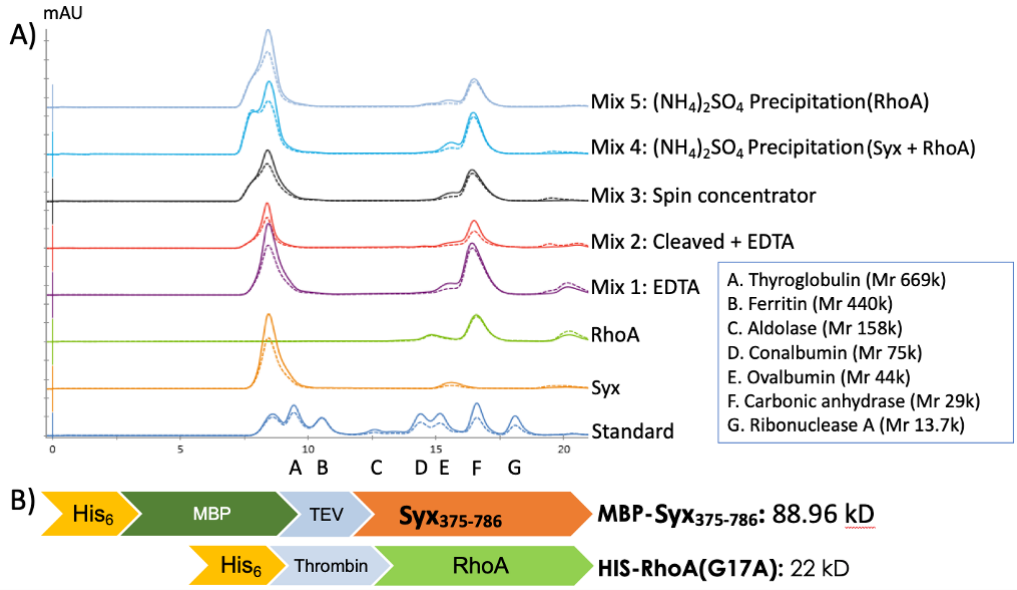

Figure 3.3: (A) SEC absorbance trace at 280nm of mixtures of MBP-$Syx_{393-792}$ and RhoA after using varying strategies for removing GDP from RhoA to induce the formation of a high affinity MBP-$Syx_{393-792}$–RhoA complex. The protein standard consists of A. Thyroglobulin (Mr 669 000), B. Ferritin (Mr 440 000), C. Aldolase (Mr 158 000), D. Conalbumin (Mr 75 000), E. Ovalbumin (Mr 44 000), F. Carbonic anhydrase (Mr 29 000), G. Ribonuclease A (Mr 13 700). MW of N-term MBP-Syx is 90.8kDa. RhoA is 22kDa. (B) Cartoons depict expressed protein fusion constructs of both MBP-$Syx_{393-792}$ and RhoA. RhoA is truncated at residue 184 to remove its highly charged linker and geranylgeranyl transferase recognition site. Mix 5 was made by ammonium sulphate precipitation of just RhoA before mixing. All other complex formation mixes (Mix 1-4) were made by first mixing MBP-$Syx_{393-792}$ and RhoA 1:1 and allowed to equilibrate for one hour before attempting to remove GDP.

3.4.5 Circular Dichroism Spectroscopy Indicates That E. coli Expressed $Syx_{393-792}$ Has Characteristic Spectra of a Folded Protein

Circular dichroism (CD) spectroscopy was performed to ascertain if cleaved $Syx_{393-792}$ was folded correctly by comparing the experimentally predicted secondary

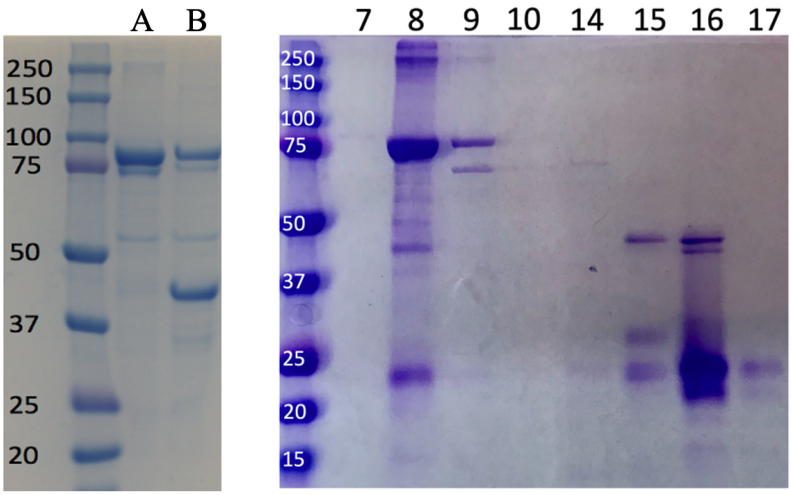

Figure 3.4: Coomassie gel on the left shows MBP-Syx$_{393-792}$ (lane A) cleavage with TEV protease produces an approximately 48kDa band (Lane B) corresponding to the molecular weight of Syx$_{393-792}$ (48kDa and MBP 42kDa), indicative of successful cleavage. Coomassie gel to the right shows fractions from SEC run "mix 4" shows the presence of bands corresponding to the correct molecular weight for RhoA and MBP-Syx$_{393-792}$. Bands in fractions at 8 and 9ml indicate the presence of MBP-Syx$_{393-792}$ and RhoA where bands in fraction 15, 16, and 17ml indicate the presence of RhoA and cleaved MBP-Syx$_{393-792}$ due to background cleavage activity at the TEV site.

structure with the secondary structure of known highly homologous crystal structures. Analysis of the CD spectra of Syx predicted an α-helical content of 30–56% and a β-sheet content of 10–24% depending on the algorithm used. CD results were checked by feeding an iTASSER homology model into PDB2CD that resulted in a plausible secondary structure prediction of 47% helix and 11% β-sheet (Table 3.1)[237]. Therefore, CD indicates the presence of a folded protein (Figure 3.4) with similar secondary structure characteristics as Syx homologues (Table 3.1).

Method	Helix	β-sheet	Turns	Unordered	NRMSD	Homology
BeStSel	30.1%	24.6%	8.6%	36.7%	0.013	-
CDSSTR	54.0%	10.0%	10.0%	24.0%	0.014	-
K2D3	36.2%	20.1%	-	43.8%	-	-
Syx_{DH-PH} model	47.2%	10.9%	-	-	-	100%
(PDZRhoGEF) 1XCG	47.1%	10.9%	-	-	-	25.8%
(P115-RhoGEF) 3ODW	57.7%	14.0%	-	-	-	23.9%
(LARG-RhoGEF) 1X86	48.7%	13.0%	-	-	-	21.4%

Table 3.1: The top of the table shows CD-spectra secondary structure prediction of $Syx_{393-792}$ using various methods including BeStSel, CDSSTR, and K2D3 vary considerably. The bottom half shows secondary structure prediction of different homologous PDB structures and the DH-PH domain of the Syx homology model.

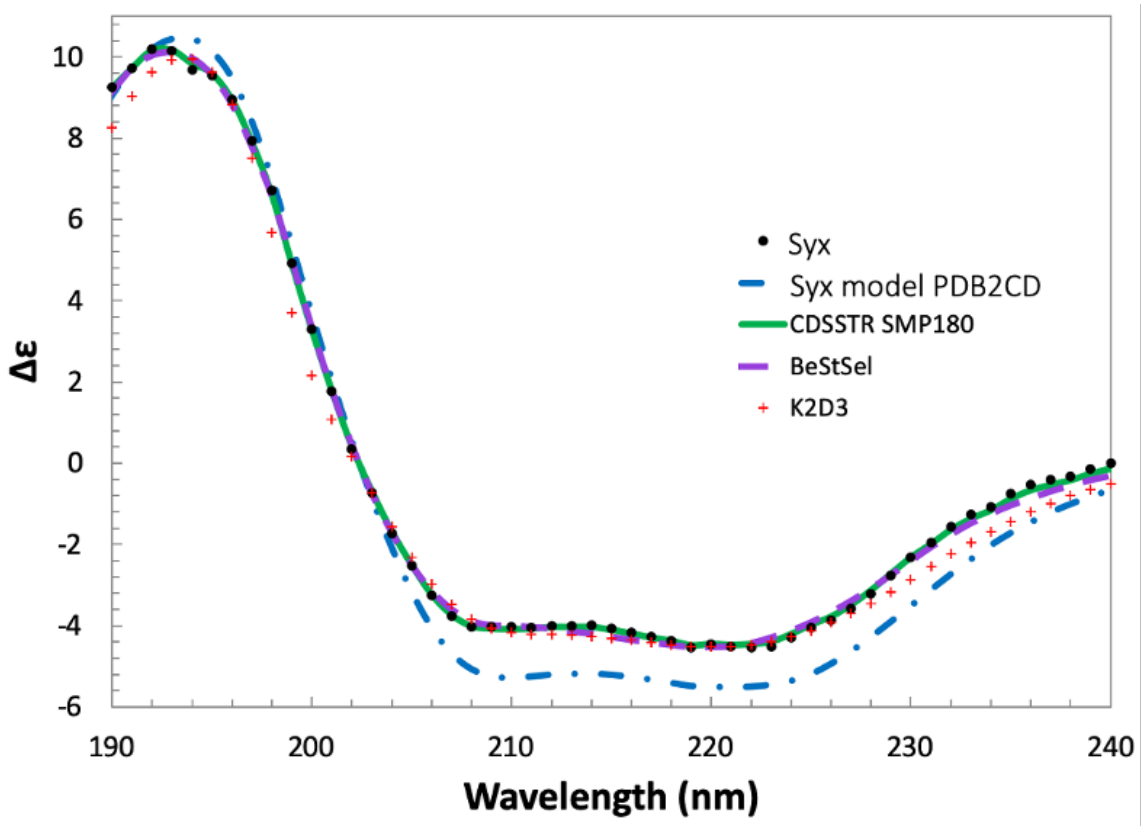

Figure 3.5: CD spectral analysis of Syx. Experimental spectra is shown as black dots in the plot below. Fits of CDSSTR (SMP180), BeStSel, and K2D3 CD analysis algorithms are shown as purple dashes, green line and red + respectively. The predicted spectra of Syx based on the homology model is shown in blue dashes.

3.4.6 Biophysical Surface Analysis

The homology model of Syx was analyzed by several methods to ascertain why size exclusion results suggest the presence of an aggregated protein. Homology models were analyzed with the protein-sol server that produced protein models scoring the ratio of solvent accessible non-polar residues to polar residues at a given location in the sequence to illustrate relative hydrophobicity of the structure. The analysis also calculated electrostatic potential of the protein surface using a Finite Difference Poisson-Boltzmann (FDPB) method to score the structure such that it can be visualized based on charge distribution (Figure 3.15)[238]. The analysis revealed a highly un-conserved, hydrophobic loop on the PH domain of Syx that may influence its interaction with the membrane or drive interactions with other hydrophobic domains (Figure 3.5, indicated in purple). Visualization of charge distribution also showed that the protein was highly polar and had a predominantly positive charge all over the DH domain including the RhoA binding site[239], and a highly negative charge on the PH domain, except for a few membrane facing loops (Figure 3.15).

3.4.7 protein Engineering

Structurally corrected CamSol web server[227] predictions indicated that several arginine residues were potentially driving aggregation, shown as redder areas on the cartoon (Figure 3.6). These predictions coincided with several predictions made by Rosetta design for stabilizing mutations. After manual curation of predicted sites, positions R466, R562, and R698 (Figure 3.6 cartoon) were chosen for site directed mutagenesis. Protein was purified and analyzed identically to Figure 3.3 MBP-Syx$_{393-792}$ control (orange trace). SEC of mutants revealed several shifts towards higher retention on the column suggesting a reduction in molecular radius of the aggregate (Figure 3.6 blue,

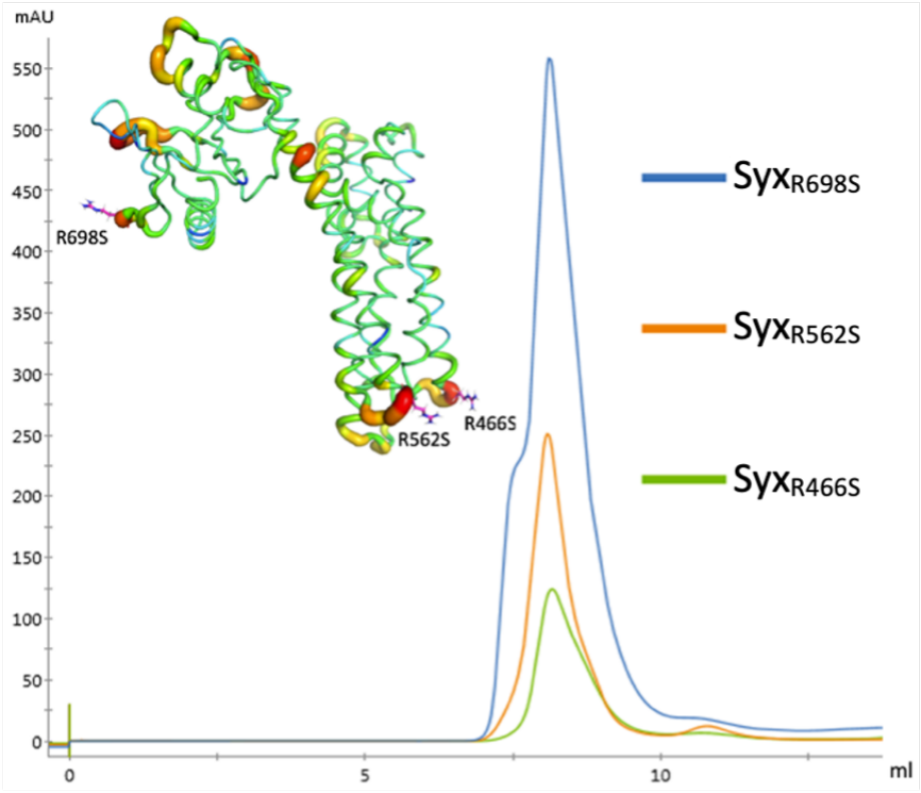

Figure 3.6: **Mutations to surface residues predicted by CamSol web server resulted in SEC peak shifts.** Mutations to surface residues predicted by CamSol web server resulted in SEC peak shifts suggesting that these mutations produced improvements to problematic aggregation characteristics. Mutant R698S shown in blue had the most pronounced peak shift.

orange, and green trace).

3.4.8 Molecular Dynamics Simulations Recapitulate Interactions Seen in RhoGEF Crystal Structures and Suggest Mechanisms of Membrane Allostery

An all atom molecular dynamics simulation of the full length Syx-RhoA complex (Figure 3.8A, cropped for visualization) was performed to observe if the protein-lipid interface between Syx and the membrane produced significant structural reorganization of hydrophobic loops, and dynamic network analysis was performed to attempt to detect interactions that might produce allosteric effects on the active site of RhoA. Dynamic

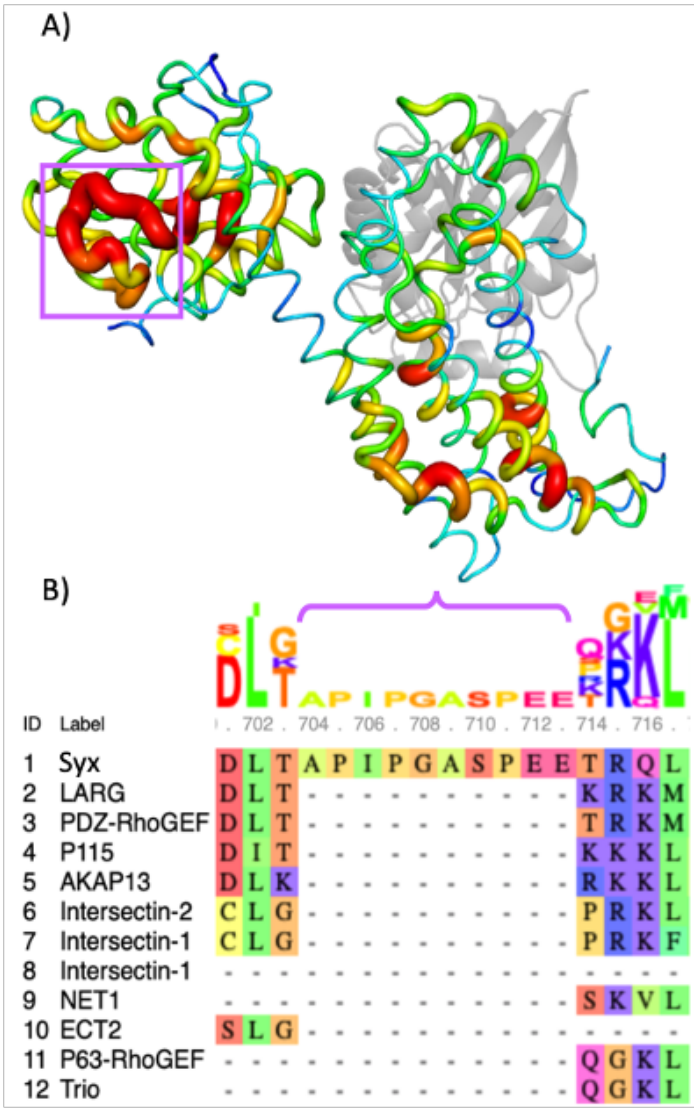

Figure 3.7: The ratio of non-polar to polar residues that are solvent accessible, as scored by the protein-sol server. Red regions have the highest ratio of non-polar residues while blue patches have the lowest ratio of non-polar to polar residues. The purple bracket indicates the unique hydrophobic loop on the Syx PH domain in the multiple sequence alignment. The analysis reveals a large, membrane facing, non-polar loop on the PH domain which is not conserved in any other homologous RhoGEF structures.

network analysis revealed that these simmulations accurately recapitulated binding interactions that have been observed in other co-crystal structures of Dbl family RhoGEFs with RhoA (Figure 3.8B)[193, 240]. Both the “switch I” and “switch II” region of RhoA

were shown to interact with the DH domain of Syx (Figure 3.8B)[115]. Syx interactions with the "switch I" region of RhoA were observed to co-vary with several residues responsible for binding the magnesium co-factor that interacts with the di-phosphate moiety of GDP, including Thr-19, Thr-37, and Asp -59. Displacement of this magnesium is expected to be pivotal for hypothesized mechanisms of guanine exchange[128]. Optimal path analysis to determine the most significant interaction networks between two linked residues suggested that several interactions between the PH domain and RhoA were observed to be capable of linking membrane interacting residues on the PH domain to many key residues in the RhoA switch region such as Thr-37. Residues such as Lys-104 of RhoA were found to propagate interactions from the PH domain all the way to the GDP binding site (Figure 3.17A), and have the potential to propagate allosteric interactions that could influence GEF activity when the GEF-RhoA complex is in the presence of a membrane. Additionally, the modeled geranylgeranyl linked cysteine-190 at the C-terminus of RhoA was observed to make several transient interactions with the membrane embedded PH domain of Syx (Figure 3.8C).

3.4.9 SEC of SF9 pDUAL Syx-RhoA Co-expression Shows a Peak at 10ml Suggesting the Presence of Protein Suitable for Structural Studies.

SF9 cells transfected with bacmid containing the pDual plasmid for co-expression of MBP-Syx$_{393-792}$ and RhoA produce protein that resulted in a SEC peak at approximately 10ml that was 2x larger than the peak at 8ml (Figure 3.9A). This peak is not present in SEC traces of proteins purified from *E.coli* cells. Coomassie stained SDS-PAGE confirms the presence of bands in all fractions at the correct molecular weight to be MBP-Syx$_{393-792}$. Bands in fractions 10, 11, and 12 correspond to fractions that elute at 10ml. These fractions also contain contaminating bands at approximately 40kDa and 15kDa (Figure 3.9B).

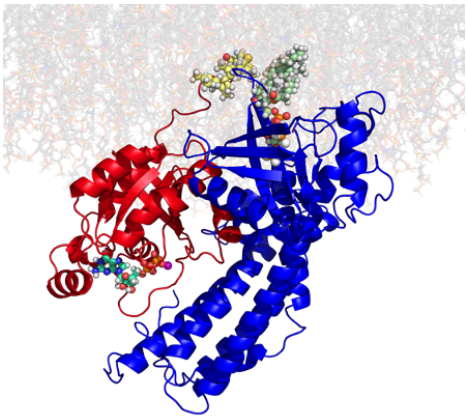

(a)

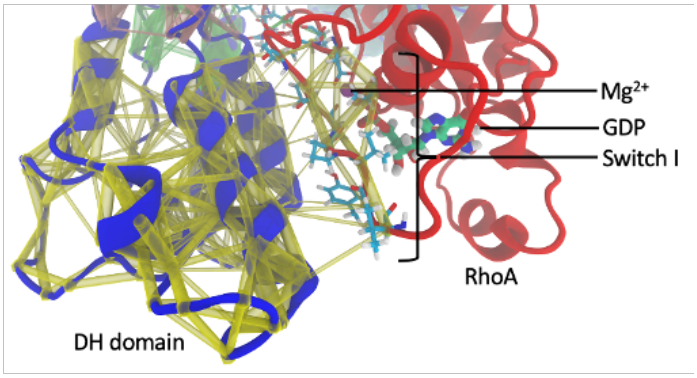

(b)

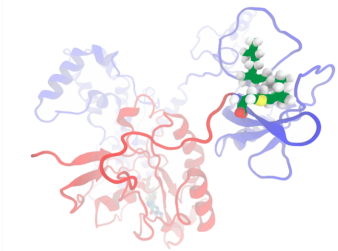

(c)

Figure 3.8: (A) The architecture of the docked Syx-RhoA complex as was simulated, complete with PI(4,5)P_2 (light green spheres), GDP (teal sticks), and Mg^2+ (purple sphere) cofactors and post translationally geranylgeranylated Cys-190 (light yellow spheres), simulated on a POPC and PI(4,5)P_2 bilayer. (B) Dynamic network analysis of the DH domain interacting with RhoA Switch I and Switch II residues (shown as cyan sticks) illustrate how these interactions (yellow tubes) influence the residues responsible for complexing Mg^2+. (C) shows the geranylgeranyl group (green) conjugated to RhoA (red) residue C190. The geranylgerany group formed transient interactions with the PH domain of Syx (blue) at the interface of the membrane and the cytoplasm during the 1 microsecond all atom mollecular dynamics simmulation.

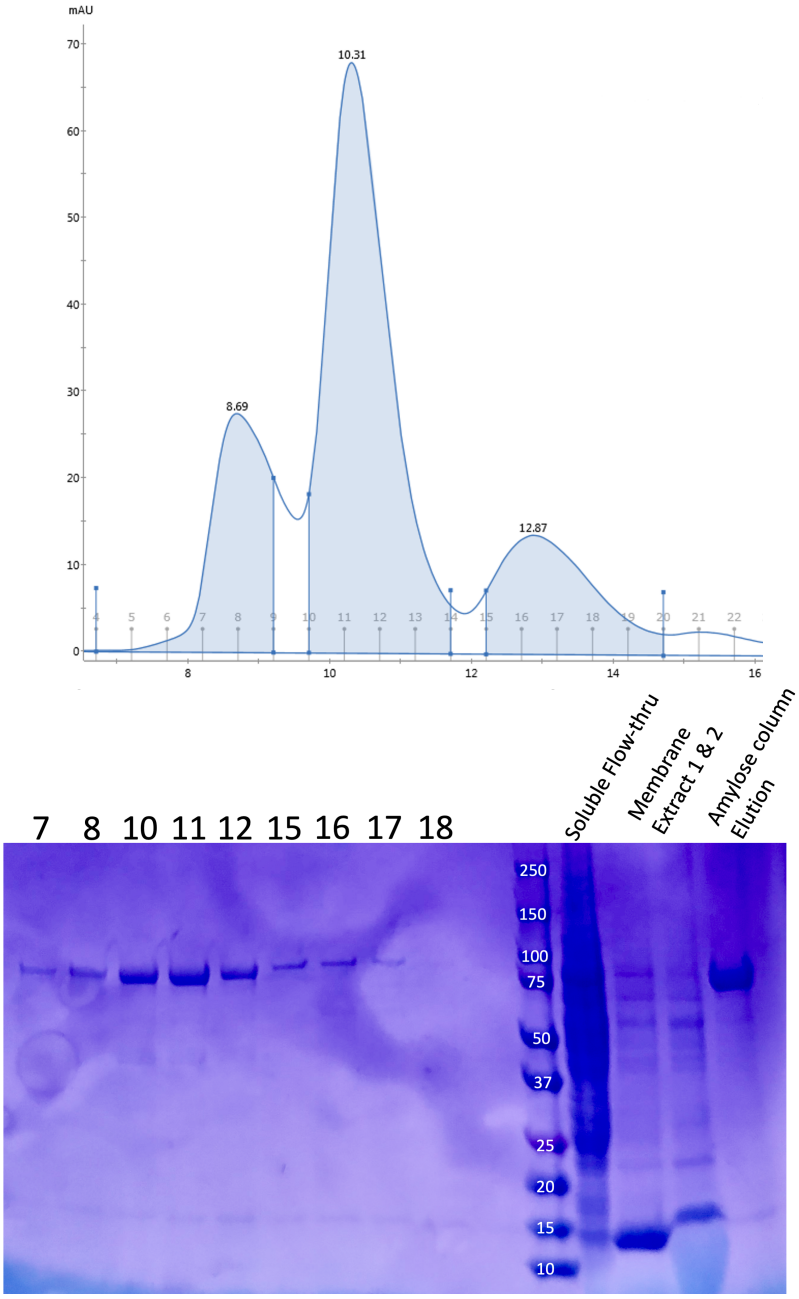

Figure 3.9: (A) Syx and RhoA co-expression in SF9 cells results protein which produces a SEC peak at 10ml. This is suggestive of the fact that this peak contains protein which is not aggregated and may be suitable for structural studies. (B) Coomassie SDS-PAGE gel of SEC fractions of the SF9 pDUAL expressed protein reveals that all fractions contain MBP-$Syx_{393-792}$, with peaks at 10ml containing traces of contamination or degradation products. On the right, lanes show protein from the amylose column elution and flow through, as well as the results of an unsuccessful membrane extraction from the same cell pellet using β-DM.

3.4.10 Lipid Blots

The lipid blots show that *E.coli* derived Syx binds PIP2 isomers, especially PI(4,5)P2, with minor binding apparent for PI(3,4)P2 and PI(3,5)P2. Unexpectedly, Syx also showed strong affinity for phosphatidic acid (PA)(Figure 3.10A). The same experiment repeated with protein derived from SF9 cells resulted in a drastically different PIP binding profile which bound the same PIP2 moieties but also bound PI(3)P, PI(4)P, and PI(5)P (Figure 3.10B).

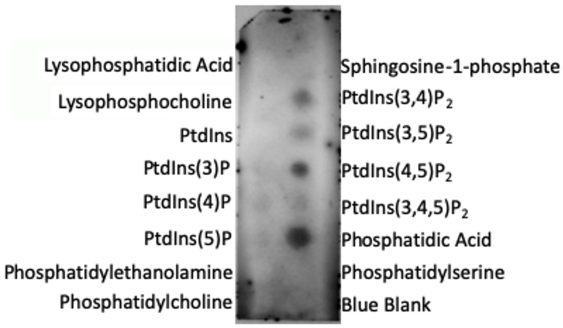

(a) *E. coli* derived lipid blot with Syx

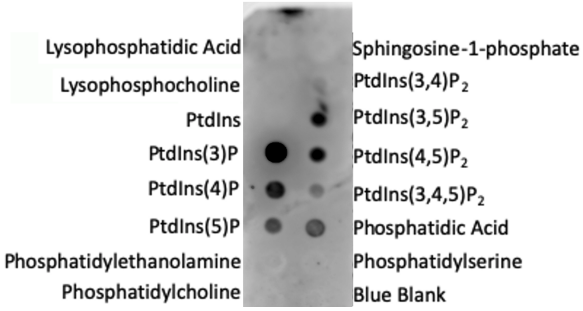

(b) *S. frugiperda* derived lipid blot with Syx

Figure 3.10: (A) Lipid blot made using *E. coli* derived $Syx_{393-792}$ shows qualitative Syx lipid binding to several lipids and indicates affinity for phosphatidic acid and PI(4,5)P2 as well as other PIP2 species. (B) Lipid blot made using $Syx_{393-792}$ from *S. frugiperda* cells shows more promiscuous binding and also shows tropism for PIP lipids PI(3)p, PI(4)P, and PI(5)P. Considering that the sequence of the construct is otherwise identical, this is suggestive of a difference in folding of the PH domain produced in each respective organism.

3.5 Discussion

Here we use a combination of protein expression, purification, spectroscopic and modeling techniques to characterize Syx, a partially soluble Dbl RhoGEF protein. Successful expression and purification of Syx was pivotal for all biophysical characterization performed. The exploratory expression of the wild type mouse Syx gene

initially displayed low expression and degradation when expressed in E. coli. The fact that codon optimization alleviated the formation of degradation products suggests that initial expression difficulties were caused by bacterial ribosomes being unable to complete production of the protein because of stoichiometric restrictions due to the presence of rare or promiscuous codons in the mouse gene. It is also notable that all solved structures of RhoGEFs were fragments of the DH and PH domain, expressed with the help of fusion constructs of either MBP or GST[241–243]. We also observed that MBP fusion enabled high level expression and protein solubility dropped dramatically upon TEV cleavage, suggesting that solubility was a culprit of the expression issues with these proteins and that hydrophobic loops might be exposed on the protein surface. Protocols for production of a monodispersed sample of native Syx protein remain elusive despite numerous exhaustive attempts at construct and buffer optimization, including pH modulation, addition of several detergents, chaotropes, kosmotropes, and charged amino acids (arginine and glutamic acid)[244, 245]. Buffer and purification optimization is ongoing with the goal of minimizing aggregation and achieving a polydispersity index (PDI) of <0.2 which is ideal for crystallographic studies. Low solubility is a major limitation for crystallographic studies which work best with high concentrations of protein. TEV cleavage of the purified MBP fusion protein produced an increasingly turbid suspension at concentrations above 4mg/ml, indicating the formation of large aggregates in solution without the solubility enhancing effects of the fusion tag (Figure 3.14). This was further corroborated by size exclusion chromatography. We have shown circular dichroism experiments that support the hypothesis that this protein is not forming a misfolded aggregate (Figure 3.5) and is instead forming non-stoichiometric homo-oligomers. This is further supported by the fact that this protein complex shows RhoA binding activity by SEC (Figure 3.3) and dot blot (Figure 3.19). This suggests that disruption of the protein-protein interactions that lead to the formation of the large non-stoichiometric homo-oligomer could result in a protein

sample which is suitable for structural studies[246–248]. This hypothesis of non-specific interaction is potentially explained by the results of the protein-sol analysis which shows that this protein contains highly hydrophobic loops which may drive interaction (Figure 3.7). The analysis also revealed highly charged domains with a large positively charged patch on the DH domain and negative charged regions on the PH domain (Figure 3.15). These patches may stick to each other without the steric bulk and entropically driven stabilizing effects of disordered regions that are present in the native protein. Protein engineering efforts focused on removing the numerous highly exposed arginine residues and other surface facing residues known to cause nonspecific protein interactions such as methionine, tryptophan, tyrosine, and phenylalanine, presents a promising approach for producing monomeric protein suitable for structural studies that will be suitable for future drug design efforts. A complex structure of Syx bound to RhoA would be most useful for structurally guided drug design so optimized protocols for forming the complex while maintaining the integrity of the proteins is needed. RhoGEFs have highest affinity for apo RhoA so formation of apo RhoA is essential, however RhoA has picomolar affinity for GDP[249]. The active site of RhoA contains a magnesium ion which forms multiple ionic interactions with the phosphate groups of GDP. Strategies to remove the tightly bound GDP require removal of the magnesium, either with excess EDTA, high concentrations of ammonium sulphate, aggressive buffer exchange, or the presence of an active GEF.

Ongoing work seeks to quantify Syx binding affinity to phosphoinositide lipids to characterize contextual protein localization in the cell and potentially establish if allosteric inhibition is possible. Lipid blots were used to verify Syx binding affinity to PI(4,5)P phospho-inositide lipids. This is the canonical ligand for PH domains[132, 196]. Syx was also observed to bind to other inositide lipids and phosphatidic acid, suggesting the presence of other binding sites or promiscuous binding. Syx is known to associate with the CRUMBS polarity complex, and is associated with stress fiber production and the

maintenance of cell-cell junctions, therefore it would make sense that the PH domain of this protein would bind a PIP lipid[109–111, 116, 133, 194, 250, 251]. However the presence of binding activity for lipids outside the canonical $PI(4,5)P_2$ suggests the possibility for previously undescribed associations and localization dynamics that may be relevant to epithelial-mesenchymal plasticity.

In vivo, Syx is bound to the CRUMBS complex via Mupp-1[133, 206]. Given the membrane trafficking at this site, it would make sense that the PH domain of this protein would likely bind $PI(4,5)P_2$, the canonical ligand for PH domains, because $PI(4,5)P_2$ is also associated with actin cytoskeletal activity modulated by the CRUMBS polarity complex[109–111, 132, 133, 206, 250–253]. Active RhoA stimulates PIP 5-kinase and subsequent formation of $PI(4,5)P_2$, implicating a positive feedback mechanism where active RhoA results in production of $PI(4,5)P_2$, which recruits Syx to reactivate RhoA as part of a cell's apical cell polarity program[253, 254]. Notably, Syx mediated RhoA activation of kinases is colocalized with angiomotin, another phosphoinositide binding protein with phosphorylation dependent oncogenic potential via the hippo pathway[206, 255]. In the future, Large Unilamellar Vesicle (LUV) pull-down assays may answer these questions as well as guide ongoing purification and structural analysis strategies that include the addition of various lipids, membrane mimetics, and protein cofactors that may reduce unwanted interactions and ultimately allow for further characterization.

All atom molecular dynamics simulations revealed a network of interactions that facilitate GEF activity when bound to RhoA. The analysis revealed several interactions between RhoA and the PH domain, mediated by hydrogen bonding networks between positively charged residues and $PI(4,5)P_2$ phospho-inositide head groups which may represent a novel mechanism for allostery (Figure 3.16, 3.17). This interaction may directly influence the active site of RhoA, as optimal path analysis of the dynamic network

showed interactions at the membrane interface of the PH domain share covariance networks that form a link to the active site of RhoA via an optimal path traveling through a lipid headgroup (Figure 3.16). Even more intriguingly, simulations revealed novel interactions between the geranylgeranyl prenyl group ligated to the N-term of RhoA residue 191. These simulated interactions represent a hypothesis for a novel function of the PH domain in membrane associated GEFs (Figure 3.8C). It is conceivable that the PH domain constitutes a lipid binding site situated within the membrane that forms intermolecular interactions with the geranylgeranyl group and helps position RhoA for efficient guanine exchange and alter the binding mode between the DH and PH domains in such a way that it could impinge on the switch regions of RhoA, and help facilitate the opening of the binding site, thus enhancing the release of GDP (Figure 3.8, 3.16). These C-terminal residues and post translational modifications of RhoA are missing from all current GEF-RhoA complex structures. Given that addition of liposomes to activity assays has been shown to enhance activity in other related systems, it is conceivable that this type of interaction is contributing to guanine exchange catalysis [198, 200, 256–258]. Structural and kinetic studies with GEFs bound to geranylgeranylated RhoA in the presence of a membrane are required to confirm this hypothesis which may be the subject of future work. Subsequent attempts at generating monodispersed Syx will be made by co-expressing Syx with RhoA in insect cells, as well as purification strategies that take into account the amphiphilic nature of this membrane-associated protein. The modeling efforts included in this paper have provided insights for ongoing future work including mutagenesis efforts to engineer the surface of Syx to replace residues that are likely to contribute to nonspecific protein interactions as well as several provocative insights into the potential effect of membranes on the structure and function of this protein that may support establishment of new druggable sites with further experimental validation.

3.6 Outlook

3.6.1 Conclusions and Further Experiments

We have shown data to suggest that insect cell derived Syx may be properly folded and monomeric, therefore more experiments are warranted to determine if this protein is suitable for structural studies. Experiments to repeat many of the characterizations done with *E.coli* derived protein such as complex formation experiments, lipid binding assays, and secondary structure analysis with a CD melting curve would establish its stability and suitability for crystallography [259].

While structural discovery remains difficult with this protein, opportunities exist to progress with research that would be beneficial for the development of therapeutics against the Syx-RhoA complex. Furthermore several tractable experiments would increase our understanding of this protein and associated disease states. Chief among these would be to measure the GEF activity of this protein. Commercial assays exist, which will determine GEF activity and are suitable for high throughput drug assays[260]. In addition, experiments measuring the tropism and binding constants of Syx small GTPase binding activity would go a long way towards establishing if Syx is predominantly a RhoA GEF as has been postulated by bioinformatic analyses of the binding site. It remains plausible that the effects of Syx knockdown are due to a different mechanism such as Rab26 tropism reported in Lüningschrör et al. (2017) [208].

A bioinformatic analysis comparing the amino acid ratios reveals that when comparing this protein's DH-PH domain with the other solved Dbl family RhoGEF structures, the ratio of arginine residues to lysine residues is significantly higher in the Syx DH-PH region than any other of the solved structures (Figure 3.6). When doing a manual analysis of the surface of the homology model of Syx it is clear that many of these residues are both solvent accessible and not relevant to the RhoA binding interface and

therefore would make good mutagenesis targets. Furthermore, it is well known that the residues methionine, tryptophan, phenylalanine, and tyrosine can also produce problematic conditions on the surface of proteins and may also be viable targets for mutagenesis. At the same time, the most significant methodological improvements would most likely be a combination of mutagenesis and expression in a mammalian cell line where the protein can be properly folded and stabilized.

3.6.2 Open Questions in Syx Biochemistry

We also note the existence of a PLEKHG5 isoform 8 (UniProt ID Q5SY18) that is noticeably absent in both a PDZ binding motif, as well as the C-terminal phosphorylation site that was shown to be a 14-3-3 protein binding site. Given that 14-3-3 protein binding may be a source of inhibition and negative regulation of GEFs, it is possible that this isoform may be an un-regulated and constitutively active form which may not appear in typical experiments where the Syx protein is visualized using antibodies or pull-down methods which bind the missing C-term.

Another open question is the level of contribution that the PH domain has in terms of binding RhoA and catalyzing GEF activity. Canonically, the DH domain is the primary domain responsible for inducing conformational changes on small GTPases that promote GDP release from the active site, and allow the GTP to bind, reactivating the small GTPase. The PH domain is largely responsible the specific localization of the GEF to negatively charged and highly phosphorylated regions of the lipid membrane. At the same time, a cursory analysis of GEF structures in the PDB reveals that variability among GEFs as to how much the PH domain interacts with their respective small G protein. Structures like 4XH9 show the PH domain directly interacting with RhoA, while 4DON shows no interaction at all. More homologous structures such as 1X86 and 1XCG show variable amounts of PH domain interaction, suggesting that this could potentially also be an artifact of crystallization

conditions or of protein folding, especially given the sensitive nature of these domains.

3.7 Supporting Information

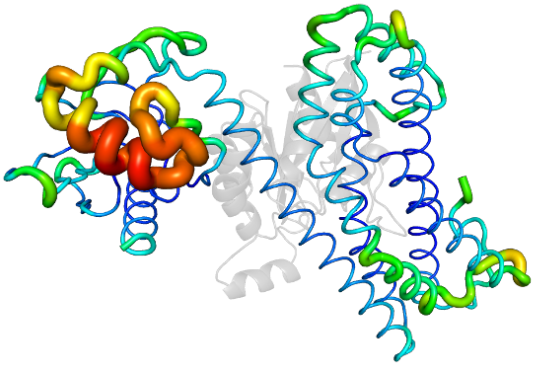

(a)

GEF name	PDB ID	Syx % identity
PDZRhoGEF	1XCG	25.81%
p115-RhoGEF	3ODW	23.95%
LARG	1X86	21.42%
AKAP-Lbc	4D0N	16.38%
p63RhoGEF	2RGN	15.84%
Dbl	1LB1	15.54%
Vav1	3KY9	15.53%

(b)

Figure 3.11: (A) Homology modeling of Syx protein. Most key functional regions associated with interactions with RhoA were highly conserved between known PDB structures (shown in blue) but some peripheral loops were not conserved and were therefore poorly modeled as shown in red. (B) Structures in the Protein Data Bank with percent identity to the Syx DH-PH domain of greater than 15% are shown. Three Dbl homology RhoGEFs had the highest percent sequence identity, with PDZRhoGEF sharing 26% sequence identity.

C-score	Expected TM-score	Expected RMSD
0.19	0.74±0.11	6.2±3.8

Table 3.2: Homology model metrics suggest that the homology model generated by iTASSER was highly accurate. C-score may vary between -5 and 2 with higher C-scores considered to be higher confidence predictions. Another measure of model quality, TM-scores of >0.5 indicates the correct overall topology as determined by RMSD.

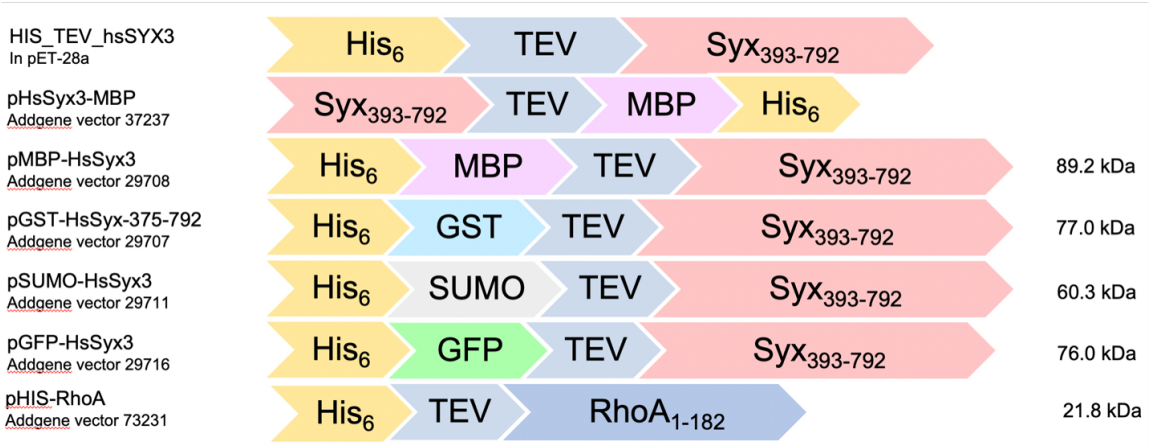

Figure 3.12: All variants of Syx were cloned into addgene constructs based off of the pET series of vectors and were expressed in BL(21) pLysS/I_Q *E.coli* cells. Constructs included N-terminal His tagged MBP, GST, SUMO, GFP, and C-terminal MBP with a TEV cleavage sequence for tag removal.

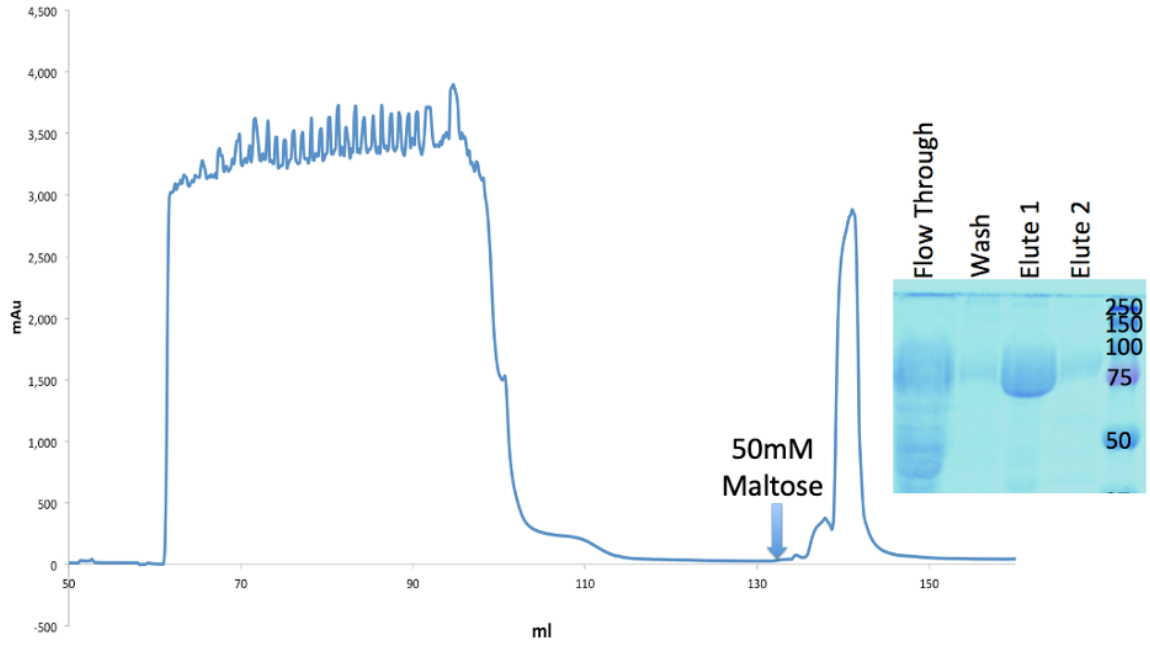

Figure 3.13: Amylose column purification trace of MBP-$Syx_{375-792}$ shown as blue trace produced approximately 90% pure protein as indicated in overlayed Coomassie SDS-PAGE gel image.

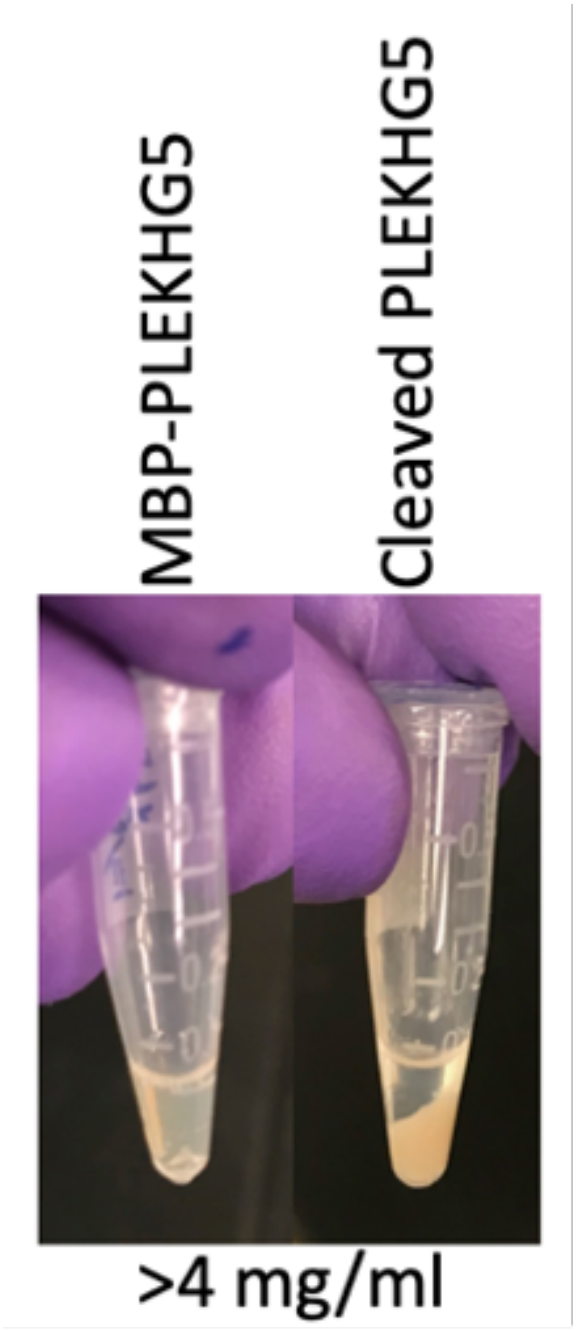

Figure 3.14: Cleavage of MBP from MBP-Syx$_{393-792}$ reduces solubility and results in crashed out protein above 4mg/ml.

Figure 3.15: B-factor tubes indicate electrostatic potential of the protein surface as calculated by the Finite Difference Poisson-Boltzmann (FDPB) method. Highly positively charged sections colored red and highly negatively charged sections in blue.

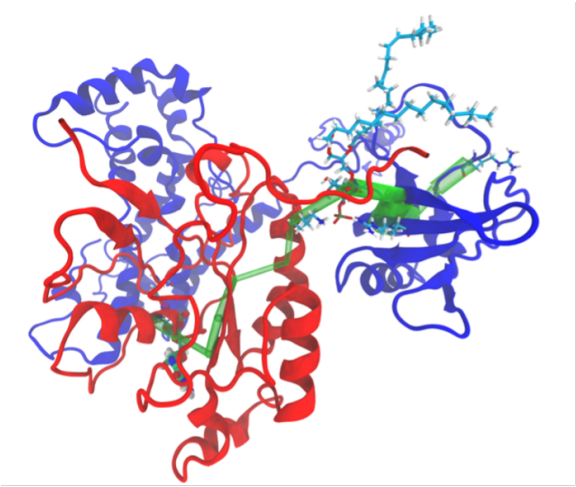

Figure 3.16: Optimal path analysis shown in green shows a direct path from residues at the membrane interface of the Syx PH domain (dark blue cartoon), through a PI(4,5)P lipid (shown as aqua colored sticks), and on to the active site of RhoA (red cartoon).

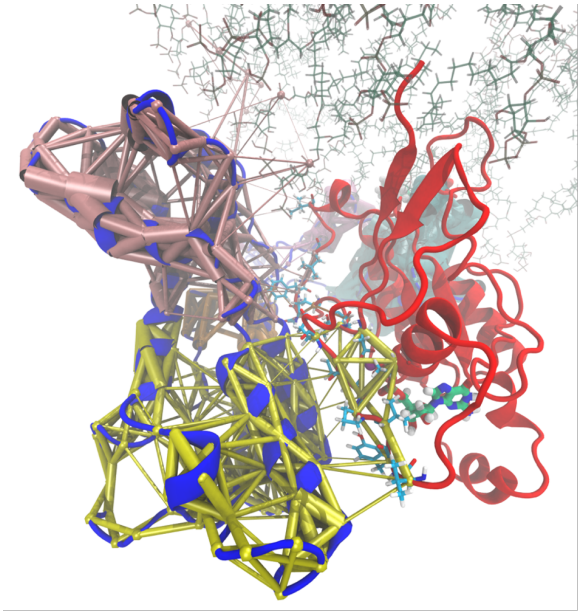

Figure 3.17: Protein-lipid interactions with a modeled lipid membrane (only PA and PI(4,5)P shown to demonstrate membrane orientation), and covariance network of the upper half of the DH domain shows interacting networks of covariance (shown in pink and yellow) propagating from the DH domain of Syx (blue cartoon) into the active site of RhoA (red cartoon). RhoA Switch I residues with significant interactions with the DH domain are shown in aqua, GDP is shown in teal.

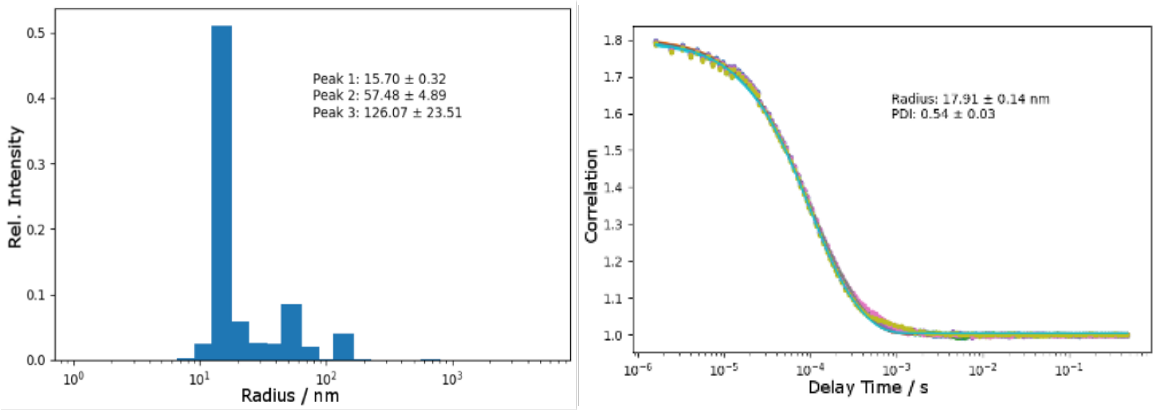

Figure 3.18: DLS of *E.coli* derrived Syx revealed a polydisperse particle size with a dominant population of particles too large to be monomeric Syx, indicating likely homo-oligomerization or aggregation.

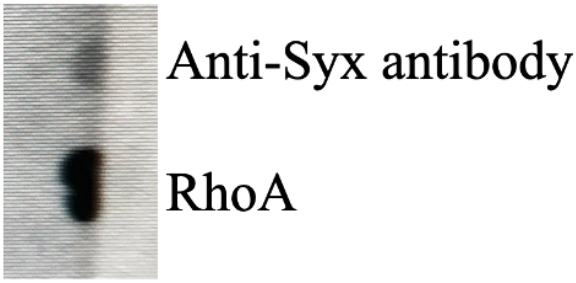

Figure 3.19: Protein dot blot shows that Syx binds to RhoA as revealed by staining with an anti-Syx antibody. The same antibody was blotted onto the membrane above RhoA as a positive control.

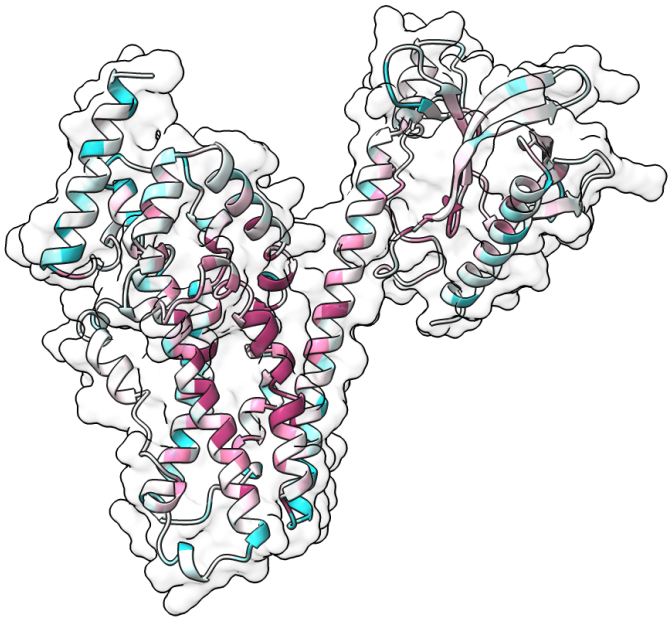

Figure 3.20: Sequence conservation between Syx and other highly homologous sequences is mapped onto a homology model of the Syx DH-PH domain. Magenta colored regions indicate the most highly conserved regions, with blue indicating the most divergent regions of the sequence. MAFFT was used to create the conservation matrix with an average sequence identity was cut-off at 18.7% pairwise % identity (BLOSUM62 pairwise % positive: 35.2%)

REFERENCES

[1] Jun Chang. Adenovirus vectors: Excellent tools for vaccine development. 21(1):e6. doi: 10.4110/in.2021.21.e6.

[2] Sarah C. Gilbert and George M. Warimwe. Rapid development of vaccines against emerging pathogens: The replication-deficient simian adenovirus platform technology. 35(35):4461–4464. doi: 10.1016/j.vaccine.2017.04.085.

[3] Eric A. Weaver and Michael A. Barry. Low Seroprevalent Species D Adenovirus Vectors as Influenza Vaccines. *PLOS ONE*, 8(8):e73313, August 2013. doi: 10.1371/journal.pone.0073313.

[4] L. Jean Patterson and Marjorie Robert-Guroff. Replicating adenovirus vector prime/protein boost strategies for HIV vaccine development. *Expert opinion on biological therapy*, 8(9):1347–1363, September 2008. doi: 10.1517/14712598.8.9.1347.

[5] Iain D. Milligan, Malick M. Gibani, Richard Sewell, Elizabeth A. Clutterbuck, Danielle Campbell, Emma Plested, Elizabeth Nuthall, Merryn Voysey, Laura Silva-Reyes, M. Juliana McElrath, Stephen C. De Rosa, Nicole Frahm, Kristen W. Cohen, Georgi Shukarev, Nicola Orzabal, Wilbert van Duijnhoven, Carla Truyers, Nora Bachmayer, Daniel Splinter, Nathaly Samy, Maria Grazia Pau, Hanneke Schuitemaker, Kerstin Luhn, Benoit Callendret, Johan Van Hoof, Macaya Douoguih, Katie Ewer, Brian Angus, Andrew J. Pollard, and Matthew D. Snape. Safety and Immunogenicity of Novel Adenovirus Type 26- and Modified Vaccinia Ankara-Vectored Ebola Vaccines: A Randomized Clinical Trial. *JAMA*, 315(15): 1610–1623, April 2016. doi: 10.1001/jama.2016.4218.

[6] W. C. Russell. Adenoviruses: update on structure and function. 90:1–20, . doi: 10.1099/vir.0.003087-0.

[7] W. C. Russell. Update on adenovirus and its vectors. 81(11):2573–2604, . doi: 10.1099/0022-1317-81-11-2573.

[8] Matthew Charman, Christin Herrmann, and Matthew D. Weitzman. Viral and cellular interactions during adenovirus DNA replication. 593(24):3531–3550. doi: 10.1002/1873-3468.13695.

[9] W. C. Russell. Adenoviruses: update on structure and function. *The Journal of General Virology*, 90(Pt 1):1–20, January 2009. doi: 10.1099/vir.0.003087-0.

[10] Alexander T. Baker, Carmen Aguirre-Hernández, Gunnel Halldén, and Alan L. Parker. Designer Oncolytic Adenovirus: Coming of Age. *Cancers*, 10(6):201, June 2018. doi: 10.3390/cancers10060201.

[11] Susan J Morris, Sarah Sebastian, Alexandra J Spencer, and Sarah C Gilbert. Simian adenoviruses as vaccine vectors. 11(9):649–659. doi: 10.2217/fvl-2016-0070.

[12] Akshay Dhingra, Elias Hage, Tina Ganzenmueller, Sindy Böttcher, Jörg Hofmann, Klaus Hamprecht, Patrick Obermeier, Barbara Rath, Fabian Hausmann, Thomas Dobner, and Albert Heim. Molecular evolution of human adenovirus (HAdV) species c. 9(1):1039. doi: 10.1038/s41598-018-37249-4.

[13] Thomas Lion. Adenovirus Infections in Immunocompetent and Immunocompromised Patients. *Clinical Microbiology Reviews*, 27(3):441–462, July 2014. doi: 10.1128/CMR.00116-13.

[14] Brennetta J. Crenshaw, Leandra B. Jones, Courtnee' R. Bell, Sanjay Kumar, and Qiana L. Matthews. Perspective on adenoviruses: Epidemiology, pathogenicity, and gene therapy. 7(3):61. doi: 10.3390/biomedicines7030061.

[15] Alison M. Kesson. Respiratory virus infections. 8(3):240–248. doi: 10.1016/j.prrv.2007.07.003.

[16] Morris Saffold Jones, Balázs Harrach, Robert D. Ganac, Mary M. A. Gozum, Wilfred P. dela Cruz, Brian Riedel, Chao Pan, Eric L. Delwart, and David P. Schnurr. New Adenovirus Species Found in a Patient Presenting with Gastroenteritis. *Journal of Virology*, 81(11):5978–5984, June 2007. doi: 10.1128/JVI.02650-06.

[17] Koki Aoki and Yoshitugu Tagawa. A Twenty-One Year Surveillance of Adenoviral Conjunctivitis in Sapporo, Japan. *International Ophthalmology Clinics*, 42(1): 49–54, January 2002.

[18] J. K. Louie, A. E. Kajon, M. Holodniy, L. Guardia-LaBar, B. Lee, A. M. Petru, J. K. Hacker, and D. P. Schnurr. Severe pneumonia due to adenovirus serotype 14: A new respiratory threat? 46(3):421–425. doi: 10.1086/525261.

[19] Tristan W Clark, Daniel H Fleet, and Martin J Wiselka. Severe community-acquired adenovirus pneumonia in an immunocompetent 44-year-old woman: a case report and review of the literature. 5(1):259. doi: 10.1186/1752-1947-5-259.

[20] Susanna Esposito, Valentina Preti, Silvia Consolo, Erica Nazzari, and Nicola Principi. Adenovirus 36 infection and obesity. 55(2):95–100. doi: 10.1016/j.jcv.2012.06.009.

[21] Maria C. Bewley, Karen Springer, Yian-Biao Zhang, Paul Freimuth, and John M. Flanagan. Structural Analysis of the Mechanism of Adenovirus Binding to Its Human Cellular Receptor, CAR. *Science*, 286(5444):1579–1583, November 1999. doi: 10.1126/science.286.5444.1579.

[22] Marko Marttila, David Persson, Dan Gustafsson, M. Kathryn Liszewski, John P. Atkinson, Göran Wadell, and Niklas Arnberg. CD46 is a cellular receptor for all species B adenoviruses except types 3 and 7. *Journal of Virology*, 79(22): 14429–14436, November 2005. doi: 10.1128/JVI.79.22.14429-14436.2005.

[23] Hongjie Wang, Zong-Yi Li, Ying Liu, Jonas Persson, Ines Beyer, Thomas Möller, Dilara Koyuncu, Max R. Drescher, Robert Strauss, Xiao-Bing Zhang, James K. Wahl Iii, Nicole Urban, Charles Drescher, Akseli Hemminki, Pascal Fender, and André

Lieber. Desmoglein 2 is a receptor for adenovirus serotypes 3, 7, 11 and 14. *Nature Medicine*, 17(1):96–104, January 2011. doi: 10.1038/nm.2270.

[24] Alexander T. Baker, Rosie M. Mundy, James A. Davies, Pierre J. Rizkallah, and Alan L. Parker. Human adenovirus type 26 uses sialic acid–bearing glycans as a primary cell entry receptor. *Science Advances*, 5(9):eaax3567, September 2019. doi: 10.1126/sciadv.aax3567.

[25] Alexander T. Baker, Rosie Mundy, James Davies, Pierre J. Rizkallah, and Alan L. Parker. Adenovirus serotype 26 utilises sialic acid bearing glycans as a primary cell entry receptor. *bioRxiv*, page 580076, March 2019. doi: 10.1101/580076.

[26] Niklas Arnberg, Patricia Pring-Åkerblom, and Göran Wadell. Adenovirus Type 37 Uses Sialic Acid as a Cellular Receptor on Chang C Cells. *Journal of Virology*, 76 (17):8834–8841, September 2002. doi: 10.1128/JVI.76.17.8834-8841.2002.

[27] Niklas Arnberg, Karin Edlund, Alistair H. Kidd, and Göran Wadell. Adenovirus Type 37 Uses Sialic Acid as a Cellular Receptor. *Journal of Virology*, 74(1):42–48, January 2000. doi: 10.1128/JVI.74.1.42-48.2000.

[28] N. Arnberg. Adenovirus receptors: implications for targeting of viral vectors. *Trends Pharmacol Sci*, 33:442–8, August 2012. doi: 10.1016/j.tips.2012.04.005.

[29] S. Patterson and W. C. Russell. Ultrastructural and Immunofluorescence Studies of Early Events in Adenovirus-HeLa Cell Interactions. *Journal of General Virology*, 64(5):1091–1099, 1983. doi: 10.1099/0022-1317-64-5-1091.

[30] Erguang Li, Dwayne Stupack, Gary M. Bokoch, and Glen R. Nemerow. Adenovirus Endocytosis Requires Actin Cytoskeleton Reorganization Mediated by Rho Family GTPases. *Journal of Virology*, 72(11):8806–8812, November 1998.

[31] Erguang Li, Dwayne Stupack, Richard Klemke, David A. Cheresh, and Glen R. Nemerow. Adenovirus Endocytosis via αv Integrins Requires Phosphoinositide-3-OH Kinase. *Journal of Virology*, 72(3):2055–2061, March 1998.

[32] Tanja Rauma, Juha Tuukkanen, Jeffrey M. Bergelson, Gerene Denning, and Timo Hautala. rab5 GTPase regulates adenovirus endocytosis. 73(11):9664–9668. doi: 10.1128/JVI.73.11.9664-9668.1999.

[33] Zsuzsanna Zsengellér, Kazuhisa Otake, Shaikh-Abu Hossain, Pierre-Yves Berclaz, and Bruce C. Trapnell. Internalization of adenovirus by alveolar macrophages initiates early proinflammatory signaling during acute respiratory tract infection. 74 (20):9655–9667. doi: 10.1128/JVI.74.20.9655-9667.2000.

[34] Nelson C. Di Paolo, Edward A. Miao, Yoichiro Iwakura, Kaja Murali-Krishna, Alan Aderem, Richard A. Flavell, Thalia Papayannopoulou, and Dmitry M. Shayakhmetov. Virus binding to a plasma membrane receptor triggers interleukin-1α-mediated proinflammatory macrophage response in vivo. 31(1):110–121. doi: 10.1016/j.immuni.2009.04.015.

[35] Mareike D. Maler, Peter J. Nielsen, Nicole Stichling, Idan Cohen, Zsolt Ruzsics, Connor Wood, Peggy Engelhard, Maarit Suomalainen, Ildiko Gyory, Michael Huber, Joachim Müller-Quernheim, Wolfgang W. A. Schamel, Siamon Gordon, Thilo Jakob, Stefan F. Martin, Willi Jahnen-Dechent, Urs F. Greber, Marina A. Freudenberg, and György Fejer. Key Role of the Scavenger Receptor MARCO in Mediating Adenovirus Infection and Subsequent Innate Responses of Macrophages. *mBio*, 8(4):e00670–17, September 2017. doi: 10.1128/mBio.00670-17.

[36] Eric Lam, Saskia Stein, and Erik Falck-Pedersen. Adenovirus Detection by the cGAS/STING/TBK1 DNA Sensing Cascade. *Journal of Virology*, 88(2):974–981, January 2014. doi: 10.1128/JVI.02702-13.

[37] Vincenzo Cerullo, Michael P Seiler, Viraj Mane, Nicola Brunetti-Pierri, Christian Clarke, Terry K Bertin, John R Rodgers, and Brendan Lee. Toll-like receptor 9 triggers an innate immune response to helper-dependent adenoviral vectors. 15(2): 378–385. doi: 10.1038/sj.mt.6300031.

[38] Laura Lau, Elizabeth E. Gray, Rebecca L. Brunette, and Daniel B. Stetson. DNA tumor virus oncogenes antagonize the cGAS-STING DNA-sensing pathway. 350 (6260):568–571. doi: 10.1126/science.aab3291.

[39] Artur Yakimovich, Heidi Gumpert, Christoph J. Burckhardt, Verena A. Lütschg, Andreas Jurgeit, Ivo F. Sbalzarini, and Urs F. Greber. Cell-free transmission of human adenovirus by passive mass transfer in cell culture simulated in a computer model. 86(18):10123–10137. doi: 10.1128/JVI.01102-12.

[40] Oliver Lieleg, Corinna Lieleg, Jesse Bloom, Christopher B. Buck, and Katharina Ribbeck. Mucin biopolymers as broad-spectrum antiviral agents. 13(6):1724–1732. doi: 10.1021/bm3001292.

[41] Christopher M. Wiethoff, Harald Wodrich, Larry Gerace, and Glen R. Nemerow. Adenovirus protein VI mediates membrane disruption following capsid disassembly. 79(4):1992–2000. doi: 10.1128/JVI.79.4.1992-2000.2005.

[42] C. L. Moyer, C. M. Wiethoff, O. Maier, J. G. Smith, and G. R. Nemerow. Functional genetic and biophysical analyses of membrane disruption by human adenovirus. 85 (6):2631–2641. doi: 10.1128/JVI.02321-10.

[43] M.Y. Nakano and U.F. Greber. Quantitative microscopy of fluorescent adenovirus entry. 129(1):57–68. doi: 10.1006/jsbi.1999.4201.

[44] Steffen Lindert, Mariena Silvestry, Tina-Marie Mullen, Glen R. Nemerow, and Phoebe L. Stewart. Cryo-Electron Microscopy Structure of an Adenovirus-Integrin Complex Indicates Conformational Changes in both Penton Base and Integrin. *Journal of Virology*, 83(22):11491–11501, November 2009. doi: 10.1128/JVI.01214-09.

[45] Harald Wodrich, Daniel Henaff, Baptist Jammart, Carolina Segura-Morales, Sigrid Seelmeir, Olivier Coux, Zsolt Ruzsics, Christopher M. Wiethoff, and Eric J. Kremer. A capsid-encoded PPxY-motif facilitates adenovirus entry. 6(3):e1000808, . doi: 10.1371/journal.ppat.1000808.

[46] James C. Warren, Adam Rutkowski, and Lynne Cassimeris. Infection with replication-deficient adenovirus induces changes in the dynamic instability of host cell microtubules. 17(8):3557–3568. doi: 10.1091/mbc.e05-09-0850.

[47] M. Suomalainen, M.Y. Nakano, K. Boucke, S. Keller, and U.F. Greber. Adenovirus-activated PKA and p38/MAPK pathways boost microtubule-mediated nuclear targeting of virus. 20(6):1310–1319, . doi: 10.1093/emboj/20.6.1310.

[48] Philip L. Leopold, Geri Kreitzer, Naoki Miyazawa, Stephanie Rempel, K. Kevin Pfister, Enrique Rodriguez-Boulan, and Ronald G. Crystal. Dynein- and microtubule-mediated translocation of adenovirus serotype 5 occurs after endosomal lysis. 11(1):151–165. doi: 10.1089/10430340050016238.

[49] Samir Kelkar, Bishnu P. De, Guangping Gao, James M. Wilson, Ronald G. Crystal, and Philip L. Leopold. A common mechanism for cytoplasmic dynein-dependent microtubule binding shared among adeno-associated virus and adenovirus serotypes. 80(15):7781–7785. doi: 10.1128/JVI.00481-06.

[50] Maarit Suomalainen, Michel Y. Nakano, Stephan Keller, Karin Boucke, Robert P. Stidwill, and Urs F. Greber. Microtubule-dependent plus- and minus end–directed motilities are competing processes for nuclear targeting of adenovirus. 144(4): 657–672, . doi: 10.1083/jcb.144.4.657.

[51] K. Helen Bremner, Julian Scherer, Julie Yi, Michael Vershinin, Steven P. Gross, and Richard B. Vallee. Adenovirus transport via direct interaction of cytoplasmic dynein with the viral capsid hexon subunit. 6(6):523–535. doi: 10.1016/j.chom.2009.11.006.

[52] Julian Scherer and Richard B. Vallee. Conformational changes in the adenovirus hexon subunit responsible for regulating cytoplasmic dynein recruitment. 89(2): 1013–1023. doi: 10.1128/JVI.02889-14.

[53] Jie Zhou, Julian Scherer, Julie Yi, and Richard B. Vallee. Role of kinesins in directed adenovirus transport and cytoplasmic exploration. 14(5):e1007055. doi: 10.1371/journal.ppat.1007055.

[54] Sten Strunze, Martin F. Engelke, I-Hsuan Wang, Daniel Puntener, Karin Boucke, Sibylle Schleich, Michael Way, Philipp Schoenenberger, Christoph J. Burckhardt, and Urs F. Greber. Kinesin-1-mediated capsid disassembly and disruption of the nuclear pore complex promote virus infection. 10(3):210–223. doi: 10.1016/j.chom.2011.08.010.

[55] Clemence E. Hindley, Fiona J. Lawrence, and David A. Matthews. A role for transportin in the nuclear import of adenovirus core proteins and DNA. 8(10): 1313–1322. doi: 10.1111/j.1600-0854.2007.00618.x.

[56] Harald Wodrich, Aurelia Cassany, Maximiliano A. D'Angelo, Tinglu Guan, Glen Nemerow, and Larry Gerace. Adenovirus core protein pVII is translocated into the nucleus by multiple import receptor pathways. 80(19):9608–9618, . doi: 10.1128/JVI.00850-06.

[57] Kasey A. Karen and Patrick Hearing. Adenovirus core protein VII protects the viral genome from a DNA damage response at early times after infection. 85(9): 4135–4142. doi: 10.1128/JVI.02540-10.

[58] Urs F. Greber and Justin W. Flatt. Adenovirus entry: From infection to immunity. 6 (1):177–197. doi: 10.1146/annurev-virology-092818-015550.

[59] Shawn M. Sumida, Diana M. Truitt, Angelique A. C. Lemckert, Ronald Vogels, Jerome H. H. V. Custers, Marylyn M. Addo, Shahin Lockman, Trevor Peter, Fred W. Peyerl, Michael G. Kishko, Shawn S. Jackson, Darci A. Gorgone, Michelle A. Lifton, Myron Essex, Bruce D. Walker, Jaap Goudsmit, Menzo J. E. Havenga, and Dan H. Barouch. Neutralizing antibodies to adenovirus serotype 5 vaccine vectors are directed primarily against the adenovirus hexon protein. 174(11):7179–7185. doi: 10.4049/jimmunol.174.11.7179.

[60] Jonatan Ersching, Malva I.M. Hernandez, Fabrizzio S. Cezarotto, Jovino D.S. Ferreira, Amely B. Martins, William M. Switzer, Zhiquan Xiang, Hildegund C.J. Ertl, Carlos R. Zanetti, and Aguinaldo R. Pinto. Neutralizing antibodies to human and simian adenoviruses in humans and new-world monkeys. 407(1):1–6. doi: 10.1016/j.virol.2010.07.043.

[61] Hugues Fausther-Bovendo and Gary P Kobinger. Pre-existing immunity against ad vectors: Humoral, cellular, and innate response, what's important? 10(10): 2875–2884. doi: 10.4161/hv.29594.

[62] Franck J. D. Mennechet, Océane Paris, Aline Raissa Ouoba, Sofia Salazar Arenas, Sodiomon B. Sirima, Guy R. Takoudjou Dzomo, Amidou Diarra, Isidore T. Traore, Dramane Kania, Karsten Eichholz, Eric A. Weaver, Edouard Tuaillon, and Eric J. Kremer. A review of 65 years of human adenovirus seroprevalence. *Expert Review of Vaccines*, 18(6):597–613, June 2019. doi: 10.1080/14760584.2019.1588113.

[63] Hua Zhao, Can Xu, Xiaoli Luo, Feng Wei, Ning Wang, Huiying Shi, and Xiubao Ren. Seroprevalence of Neutralizing Antibodies against Human Adenovirus Type-5 and Chimpanzee Adenovirus Type-68 in Cancer Patients. *Frontiers in Immunology*, 9, March 2018. doi: 10.3389/fimmu.2018.00335.

[64] Alan L. Parker, Simon N. Waddington, Suzanne M. K. Buckley, Jerome Custers, Menzo J. E. Havenga, Nico van Rooijen, Jaap Goudsmit, John H. McVey, Stuart A. Nicklin, and Andrew H. Baker. Effect of neutralizing sera on factor x-mediated adenovirus serotype 5 gene transfer. 83(1):479–483. doi: 10.1128/JVI.01878-08.

[65] H. Qiu, X. Li, X. Tian, Z. Zhou, K. Xing, H. Li, N. Tang, W. Liu, P. Bai, and R. Zhou. Serotype-specific neutralizing antibody epitopes of human adenovirus type 3 (HAdV-3) and HAdV-7 reside in multiple hexon hypervariable regions. 86(15): 7964–7975. doi: 10.1128/JVI.07076-11.

[66] Jiangtao Ma, Margaret R. Duffy, Lin Deng, Rachel S. Dakin, Taco Uil, Jerome Custers, Sharon M. Kelly, John H. McVey, Stuart A. Nicklin, and Andrew H. Baker. Manipulating Adenovirus Hexon Hypervariable Loops Dictates Immune Neutralisation and Coagulation Factor X-dependent Cell Interaction In

Vitro and In Vivo. *PLOS Pathogens*, 11(2):e1004673, February 2015. doi: 10.1371/journal.ppat.1004673. Publisher: Public Library of Science.

[67] Feng-Cai Zhu, Yu-Hua Li, Xu-Hua Guan, Li-Hua Hou, Wen-Juan Wang, Jing-Xin Li, Shi-Po Wu, Bu-Sen Wang, Zhao Wang, Lei Wang, Si-Yue Jia, Hu-Dachuan Jiang, Ling Wang, Tao Jiang, Yi Hu, Jin-Bo Gou, Sha-Bei Xu, Jun-Jie Xu, Xue-Wen Wang, Wei Wang, and Wei Chen. Safety, tolerability, and immunogenicity of a recombinant adenovirus type-5 vectored COVID-19 vaccine: a dose-escalation, open-label, non-randomised, first-in-human trial. *The Lancet*, 395 (10240):1845–1854, June 2020. doi: 10.1016/S0140-6736(20)31208-3. Publisher: Elsevier.

[68] Jerald Sadoff, Glenda Gray, An Vandebosch, Vicky Cárdenas, Georgi Shukarev, Beatriz Grinsztejn, Paul A. Goepfert, Carla Truyers, Hein Fennema, Bart Spiessens, Kim Offergeld, Gert Scheper, Kimberly L. Taylor, Merlin L. Robb, John Treanor, Dan H. Barouch, Jeffrey Stoddard, Martin F. Ryser, Mary A. Marovich, Kathleen M. Neuzil, Lawrence Corey, Nancy Cauwenberghs, Tamzin Tanner, Karin Hardt, Javier Ruiz-Guiñazú, Mathieu Le Gars, Hanneke Schuitemaker, Johan Van Hoof, Frank Struyf, and Macaya Douoguih. Safety and efficacy of single-dose ad26.COV2.s vaccine against covid-19. 384(23):2187–2201. doi: 10.1056/NEJMoa2101544.

[69] Merryn Voysey, Sue Ann Costa Clemens, Shabir A. Madhi, Lily Y. Weckx, Pedro M. Folegatti, Parvinder K. Aley, Brian Angus, Vicky L. Baillie, Shaun L. Barnabas, Qasim E. Bhorat, Sagida Bibi, Carmen Briner, Paola Cicconi, Andrea M. Collins, Rachel Colin-Jones, Clare L. Cutland, Thomas C. Darton, Keertan Dheda, Christopher J. A. Duncan, Katherine R. W. Emary, Katie J. Ewer, Lee Fairlie, Saul N. Faust, Shuo Feng, Daniela M. Ferreira, Adam Finn, Anna L. Goodman, Catherine M. Green, Christopher A. Green, Paul T. Heath, Catherine Hill, Helen Hill, Ian Hirsch, Susanne H. C. Hodgson, Alane Izu, Susan Jackson, Daniel Jenkin, Carina C. D. Joe, Simon Kerridge, Anthonet Koen, Gaurav Kwatra, Rajeka Lazarus, Alison M. Lawrie, Alice Lelliott, Vincenzo Libri, Patrick J. Lillie, Raburn Mallory, Ana V. A. Mendes, Eveline P. Milan, Angela M. Minassian, Alastair McGregor, Hazel Morrison, Yama F. Mujadidi, Anusha Nana, Peter J. O'Reilly, Sherman D. Padayachee, Ana Pittella, Emma Plested, Katrina M. Pollock, Maheshi N. Ramasamy, Sarah Rhead, Alexandre V. Schwarzbold, Nisha Singh, Andrew Smith, Rinn Song, Matthew D. Snape, Eduardo Sprinz, Rebecca K. Sutherland, Richard Tarrant, Emma C. Thomson, M. Estée Török, Mark Toshner, David P. J. Turner, Johan Vekemans, Tonya L. Villafana, Marion E. E. Watson, Christopher J. Williams, Alexander D. Douglas, Adrian V. S. Hill, Teresa Lambe, Sarah C. Gilbert, Andrew J. Pollard, Marites Aban, Fatola Abayomi, Kushala Abeyskera, Jeremy Aboagye, Matthew Adam, Kirsty Adams, James Adamson, Yemi A. Adelaja, Gbadebo Adewetan, Syed Adlou, Khatija Ahmed, Yasmeen Akhalwaya, Saajida Akhalwaya, Andrew Alcock, Aabidah Ali, Elizabeth R. Allen, Lauren Allen, Thamires C. D. S. C. Almeida, Mariana P. S. Alves, Fabio Amorim, Foteini Andritsou, Rachel Anslow, Matthew Appleby, Edward H. Arbe-Barnes, Mark P. Ariaans, Beatriz Arns, Laiana Arruda, Paula Azi, Lorena Azi, Gavin Babbage, Catherine Bailey, Kenneth F. Baker, Megan Baker, Natalie Baker, Philip Baker, Lisa Baldwin, Ioana Baleanu, Danieli Bandeira, Anna Bara, Marcella

A. S. Barbosa, Debbie Barker, Gavin D. Barlow, Eleanor Barnes, Andrew S. Barr, Jordan R. Barrett, Jessica Barrett, Louise Bates, Alexander Batten, Kirsten Beadon, Emily Beales, Rebecca Beckley, Sandra Belij-Rammerstorfer, Jonathan Bell, Duncan Bellamy, Nancy Bellei, Sue Belton, Adam Berg, Laura Bermejo, Eleanor Berrie, Lisa Berry, Daniella Berzenyi, Amy Beveridge, Kevin R. Bewley, Helen Bexhell, Sutika Bhikha, Asad E. Bhorat, Zaheda E. Bhorat, Else Bijker, Geeta Birch, Sarah Birch, Adam Bird, Olivia Bird, Karen Bisnauthsing, Mustapha Bittaye, Katherine Blackstone, Luke Blackwell, Heather Bletchly, Caitlin L. Blundell, Susannah R. Blundell, Pritesh Bodalia, Bruno C. Boettger, Emma Bolam, Elena Boland, Daan Bormans, Nicola Borthwick, Francesca Bowring, Amy Boyd, Penny Bradley, Tanja Brenner, Phillip Brown, Claire Brown, Charlie Brown-O'Sullivan, Scott Bruce, Emily Brunt, Ruaridh Buchan, William Budd, Yusuf A. Bulbulia, Melanie Bull, Jamie Burbage, Hassan Burhan, Aileen Burn, Karen R. Buttigieg, Nicholas Byard, Ingrid Cabera Puig, Gloria Calderon, Anna Calvert, Susana Camara, Michelangelo Cao, Federica Cappuccini, João R. Cardoso, Melanie Carr, Miles W. Carroll, Andrew Carson-Stevens, Yasmin de M. Carvalho, José A. M. Carvalho, Helen R. Casey, Paul Cashen, Thais Castro, Lucia Carratala Castro, Katrina Cathie, Ana Cavey, José Cerbino-Neto, Jim Chadwick, David Chapman, Sue Charlton, Irina Chelysheva, Oliver Chester, Sunder Chita, Jee-Sun Cho, Liliana Cifuentes, Elizabeth Clark, Matthew Clark, Andrea Clarke, Elizabeth A. Clutterbuck, Sarah L. K. Collins, Christopher P. Conlon, Sean Connarty, Naomi Coombes, Cushla Cooper, Rachel Cooper, Lynne Cornelissen, Tumena Corrah, Catherine Cosgrove, Tony Cox, Wendy E. M. Crocker, Sarah Crosbie, Lorraine Cullen, Dan Cullen, Debora R. M. F. Cunha, Christina Cunningham, Fiona C. Cuthbertson, Suzete N. Farias Da Guarda, Larissa P. da Silva, Brad E. Damratoski, Zsofia Danos, Maria T. D. C. Dantas, Paula Darroch, Mehreen S. Datoo, Chandrabali Datta, Malika Davids, Sarah L. Davies, Hannah Davies, Elizabeth Davis, Judith Davis, John Davis, Maristela M. D. De Nobrega, Lis Moreno De Oliveira Kalid, David Dearlove, Tesfaye Demissie, Amisha Desai, Stefania Di Marco, Claudio Di Maso, Maria I. S. Dinelli, Tanya Dinesh, Claire Docksey, Christina Dold, Tao Dong, Francesca R. Donnellan, Tannyth Dos Santos, Thainá G. dos Santos, Erika Pachecho Dos Santos, Naomi Douglas, Charlotte Downing, Jonathan Drake, Rachael Drake-Brockman, Kimberley Driver, Ruth Drury, Susanna J. Dunachie, Benjamin S. Durham, Lidiana Dutra, Nicholas J. W. Easom, Samual van Eck, Mandy Edwards, Nick J. Edwards, Omar M. El Muhanna, Sean C. Elias, Mike Elmore, Marcus English, Alisgair Esmail, Yakub Moosa Essack, Eoghan Farmer, Mutjaba Farooq, Madi Farrar, Leonard Farrugia, Beverley Faulkner, Sofiya Fedosyuk, Sally Felle, Shuo Feng, Carla Ferreira Da Silva, Samantha Field, Richard Fisher, Amy Flaxman, James Fletcher, Hazel Fofie, Henry Fok, Karen J. Ford, Jamie Fowler, Pedro H. A. Fraiman, Emma Francis, Marilia M. Franco, John Frater, Marilúcia S. M. Freire, Samantha H. Fry, Sabrina Fudge, Julie Furze, Michelle Fuskova, Pablo Galian-Rubio, Eva Galiza, Harriet Garlant, Madita Gavrila, Ailsa Geddes, Karyna A. Gibbons, Ciaran Gilbride, Hardeep Gill, Sharon Glynn, Kerry Godwin, Karishma Gokani, Ursula Carvalho Goldoni, Maria Goncalves, Isabela G. S. Gonzalez, Jayne Goodwin, Amina Goondiwala, Katherine Gordon-Quayle, Giacomo Gorini, Janet Grab, Lara Gracie, Melanie Greenland, Nicola Greenwood, Johann Greffrath, Marisa M. Groenewald, Leonardo Grossi, Gaurav Gupta, Mark Hackett, Bassam Hallis, Mainga Hamaluba,

Elizabeth Hamilton, Joseph Hamlyn, Daniel Hammersley, Aidan T. Hanrath, Brama Hanumunthadu, Stephanie A. Harris, Clair Harris, Tara Harris, Thomas D. Harrison, Daisy Harrison, Thomas C. Hart, Birgit Hartnell, Shadin Hassan, John Haughney, Sophia Hawkins, Jodie Hay, Ian Head, John Henry, Macarena Hermosin Herrera, David B. Hettle, Jennifer Hill, Gina Hodges, Elizea Horne, Mimi M. Hou, Catherine Houlihan, Elizabeth Howe, Nicola Howell, Jonathan Humphreys, Holly E. Humphries, Katrina Hurley, Claire Huson, Angela Hyder-Wright, Catherine Hyams, Sabina Ikram, Alka Ishwarbhai, Monica Ivan, Poppy Iveson, Vidyashankara Iyer, Frederic Jackson, Jeanne De Jager, Shameem Jaumdally, Helen Jeffers, Natasha Jesudason, Bryony Jones, Kathryn Jones, Elizabeth Jones, Christopher Jones, Marianna Rocha Jorge, Aylin Jose, Amar Joshi, Eduardo A. M. S. Júnior, Joanne Kadziola, Reshma Kailath, Faeeza Kana, Konstantinos Karampatsas, Mwila Kasanyinga, Jade Keen, Elizabeth J. Kelly, Dearbhla M. Kelly, Debbie Kelly, Sarah Kelly, David Kerr, Renato de Ávila Kfouri, Liaquat Khan, Baktash Khozoee, Sarah Kidd, Annabel Killen, Jasmin Kinch, Patrick Kinch, Lloyd D. W. King, Thomas B. King, Lucy Kingham, Paul Klenerman, Francesca Knapper, Julian C. Knight, Daniel Knott, Stanislava Koleva, Matilda Lang, Gail Lang, Colin W. Larkworthy, Jessica P. J. Larwood, Rebecca Law, Erica M. Lazarus, Amanda Leach, Emily A. Lees, Nana-Marie Lemm, Alvaro Lessa, Stephanie Leung, Yuanyuan Li, Amelia M. Lias, Kostas Liatsikos, Aline Linder, Samuel Lipworth, Shuchang Liu, Xinxue Liu, Adam Lloyd, Stephanie Lloyd, Lisa Loew, Raquel Lopez Ramon, Leandro Lora, Vicki Lowthorpe, Kleber Luz, Jonathan C. MacDonald, Gordon MacGregor, Meera Madhavan, David O. Mainwaring, Edson Makambwa, Rebecca Makinson, Mookho Malahleha, Ross Malamatsho, Garry Mallett, Kushal Mansatta, Takalani Maoko, Katlego Mapetla, Natalie G. Marchevsky, Spyridoula Marinou, Emma Marlow, Gabriela N. Marques, Paula Marriott, Richard P. Marshall, Julia L. Marshall, Flávia J. Martins, Masebole Masenya, Mduduzi Masilela, Shauna K. Masters, Moncy Mathew, Hosea Matlebjane, Kedidimetse Matshidiso, Olga Mazur, Andrea Mazzella, Hugh McCaughan, Joanne McEwan, Joanna McGlashan, Lorna McInroy, Zoe McIntyre, Daniela McLenaghan, Nicky McRobert, Steve McSwiggan, Clare Megson, Savviz Mehdipour, Wilma Meijs, Renata N. Á Mendonça, Alexander J. Mentzer, Neginsadat Mirtorabi, Celia Mitton, Sibusiso Mnyakeni, Fiona Moghaddas, Kgaogelo Molapo, Mapule Moloi, Maria Moore, M. Isabel Moraes-Pinto, Marni Moran, Ella Morey, Róisín Morgans, Susan Morris, Sheila Morris, Helen C. Morris, Franca Morselli, Gertraud Morshead, Richard Morter, Lynelle Mottal, Andrew Moultrie, Nathifa Moya, Mushiya Mpelembue, Sibekezelo Msomi, Yvonne Mugodi, Ekta Mukhopadhyay, Jilly Muller, Alasdair Munro, Claire Munro, Sarah Murphy, Philomena Mweu, Celia Hatsuko Myasaki, Gurudutt Naik, Kush Naker, Eleni Nastouli, Abida Nazir, Bongani Ndlovu, Fabio Neffa, Cecilia Njenga, Helena Noal, Andrés Noé, Gabrielle Novaes, Fay L. Nugent, Géssika Nunes, Katie O'Brien, Daniel O'Connor, Miranda Odam, Suzette Oelofse, Blanche Oguti, Victoria Olchawski, Neil J. Oldfield, Marianne G. Oliveira, Catarina Oliveira, Angela Oosthuizen, Paula O'Reilly, Piper Osborne, David R. J. Owen, Lydia Owen, Daniel Owens, Nelly Owino, Mihaela Pacurar, Brenda V. B. Paiva, Edna M. F. Palhares, Susan Palmer, Sivapriyai Parkinson, Helena M. R. T. Parracho, Karen Parsons, Dipak Patel, Bhumika Patel, Faeezah Patel, Kelly Patel, Maia Patrick-Smith, Ruth O. Payne, Yanchun Peng, Elizabeth J. Penn, Anna Pennington,

Marco Polo Peralta Alvarez, James Perring, Nicola Perry, Rubeshan Perumal, Sahir Petkar, Tricia Philip, Daniel J. Phillips, Jennifer Phillips, Mary Kgomotso Phohu, Lorinda Pickup, Sonja Pieterse, Jo Piper, Dimitra Pipini, Mary Plank, Joan Du Plessis, Samuel Pollard, Jennifer Pooley, Anil Pooran, Ian Poulton, Claire Powers, Fernando B. Presa, David A. Price, Vivien Price, Marcelo Primeira, Pamela C. Proud, Samuel Provstgaard-Morys, Sophie Pueschel, David Pulido, Sheena Quaid, Ria Rabara, Alexandra Radford, Kajal Radia, Durga Rajapaska, Thurkka Rajeswaran, Alberto San Francisco Ramos, Fernando Ramos Lopez, Tommy Rampling, Jade Rand, Helen Ratcliffe, Tom Rawlinson, David Rea, Byron Rees, Jesús Reiné, Mila Resuello-Dauti, Emilia Reyes Pabon, Carla M. Ribiero, Marivic Ricamara, Alex Richter, Neil Ritchie, Adam J. Ritchie, Alexander J. Robbins, Hannah Roberts, Ryan E. Robinson, Hannah Robinson, Talita T. Rocchetti, Beatriz Pinho Rocha, Sophie Roche, Christine Rollier, Louisa Rose, Amy L. Ross Russell, Lindie Rossouw, Simon Royal, Indra Rudiansyah, Sarah Ruiz, Stephen Saich, Claudia Sala, Jessica Sale, Ahmed M. Salman, Natalia Salvador, Stephannie Salvador, Milla Sampaio, Annette D. Samson, Amada Sanchez-Gonzalez, Helen Sanders, Katherine Sanders, Erika Santos, Mayara F. S. Santos Guerra, Iman Satti, Jack E. Saunders, Caroline Saunders, Aakifah Sayed, Ina Schim van der Loeff, Annina B. Schmid, Ella Schofield, Gavin Screaton, Samiullah Seddiqi, Rameswara R. Segireddy, Roberta Senger, Sonia Serrano, Rajiv Shah, Imam Shaik, Hannah E. Sharpe, Katherine Sharrocks, Robert Shaw, Adam Shea, Amy Shepherd, James G. Shepherd, Farah Shiham, Emad Sidhom, Sarah E. Silk, Antonio Carlos da Silva Moraes, Gilberto Silva-Junior, Laura Silva-Reyes, Anderson D. Silveira, Mariana B. V. Silveira, Jaisi Sinha, Donal T. Skelly, Daniel C. Smith, Nick Smith, Holly E. Smith, David J. Smith, Catherine C. Smith, Airanuédida Soares, Tiago Soares, Carla Solórzano, Guilherme L. Sorio, Kim Sorley, Tiffany Sosa-Rodriguez, Cinthia M. C. D. L. Souza, Bruno S. D. F. Souza, Alessandra R. Souza, Alexandra J. Spencer, Fernanda Spina, Louise Spoors, Lizzie Stafford, Imogen Stamford, Igor Starinskij, Ricardo Stein, Jill Steven, Lisa Stockdale, Lisa V. Stockwell, Louise H. Strickland, Arabella C. Stuart, Ann Sturdy, Natalina Sutton, Anna Szigeti, Abdessamad Tahiri-Alaoui, Rachel Tanner, Carol Taoushanis, Alexander W. Tarr, Keja Taylor, Ursula Taylor, Iona Jennifer Taylor, Justin Taylor, Rebecca te Water Naude, Yrene Themistocleous, Andreas Themistocleous, Merin Thomas, Kelly Thomas, Tonia M. Thomas, Asha Thombrayil, Fawziyah Thompson, Amber Thompson, Kevin Thompson, Ameeka Thompson, Julia Thomson, Viv Thornton-Jones, Patrick J. Tighe, Lygia Accioly Tinoco, Gerlynn Tiongson, Bonolo Tladinyane, Michele Tomasicchio, Adriana Tomic, Susan Tonks, James Towner, Nguyen Tran, Julia Tree, Gerry Trillana, Charlotte Trinham, Rose Trivett, Adam Truby, Betty Lebogang Tsheko, Aadil Turabi, Richard Turner, Cheryl Turner, Marta Ulaszewska, Benjamin R. Underwood, Rachel Varughese, Dennis Verbart, Marije Verheul, Iason Vichos, Taiane Vieira, Claire S. Waddington, Laura Walker, Erica Wallis, Matthew Wand, Deborah Warbick, Theresa Wardell, George Warimwe, Sarah C. Warren, Bridget Watkins, Ekaterina Watson, Stewart Webb, Alice Webb-Bridges, Angela Webster, Jessica Welch, Jeanette Wells, Alison West, Caroline White, Rachel White, Paul Williams, Rachel L. Williams, Rebecca Winslow, Mark Woodyer, Andrew T. Worth, Danny Wright, Marzena Wroblewska, Andy Yao, Rafael Zimmer, Dalila Zizi, and Peter Zuidewind. Safety and efficacy of the

ChAdOx1 nCoV-19 vaccine (AZD1222) against SARS-CoV-2: an interim analysis of four randomised controlled trials in Brazil, South Africa, and the UK. *The Lancet*, 397(10269):99–111, January 2021. doi: 10.1016/S0140-6736(20)32661-1. Publisher: Elsevier.

[70] Denis Y Logunov, Inna V Dolzhikova, Dmitry V Shcheblyakov, Amir I Tukhvatulin, Olga V Zubkova, Alina S Dzharullaeva, Anna V Kovyrshina, Nadezhda L Lubenets, Daria M Grousova, Alina S Erokhova, Andrei G Botikov, Fatima M Izhaeva, Olga Popova, Tatiana A Ozharovskaya, Ilias B Esmagambetov, Irina A Favorskaya, Denis I Zrelkin, Daria V Voronina, Dmitry N Shcherbinin, Alexander S Semikhin, Yana V Simakova, Elizaveta A Tokarskaya, Daria A Egorova, Maksim M Shmarov, Natalia A Nikitenko, Vladimir A Gushchin, Elena A Smolyarchuk, Sergey K Zyryanov, Sergei V Borisevich, Boris S Naroditsky, and Alexander L Gintsburg. Safety and efficacy of an rAd26 and rAd5 vector-based heterologous prime-boost COVID-19 vaccine: an interim analysis of a randomised controlled phase 3 trial in russia. 397(10275):671–681. doi: 10.1016/S0140-6736(21)00234-8.

[71] Matthew D. J. Dicks, Alexandra J. Spencer, Nick J. Edwards, Göran Wadell, Kalifa Bojang, Sarah C. Gilbert, Adrian V. S. Hill, and Matthew G. Cottingham. A Novel Chimpanzee Adenovirus Vector with Low Human Seroprevalence: Improved Systems for Vector Derivation and Comparative Immunogenicity. *PLoS ONE*, 7(7), July 2012. doi: 10.1371/journal.pone.0040385.

[72] Katie Ewer, Sarah Sebastian, Alexandra J. Spencer, Sarah Gilbert, Adrian V. S. Hill, and Teresa Lambe. Chimpanzee adenoviral vectors as vaccines for outbreak pathogens. 13(12):3020–3032. doi: 10.1080/21645515.2017.1383575.

[73] Anu-Maaria Puumalainen, Matti Vapalahti, Reitu S. Agrawal, Maija Kossila, Johanna Laukkanen, Pauliina Lehtolainen, Helena Viita, Leo Paljärvi, Ritva Vanninen, and Seppo Ylä-Herttuala. β-Galactosidase Gene Transfer to Human Malignant Glioma In Vivo Using Replication-Deficient Retroviruses and Adenoviruses. *Human Gene Therapy*, 9(12):1769–1774, August 1998. doi: 10.1089/hum.1998.9.12-1769.

[74] H. Chen, Z. Q. Xiang, Y. Li, R. K. Kurupati, B. Jia, A. Bian, D. M. Zhou, N. Hutnick, S. Yuan, C. Gray, J. Serwanga, B. Auma, P. Kaleebu, X. Zhou, M. R. Betts, and H. C. J. Ertl. Adenovirus-Based Vaccines: Comparison of Vectors from Three Species of Adenoviridae. *Journal of Virology*, 84(20):10522–10532, October 2010. doi: 10.1128/JVI.00450-10.

[75] Julie C. Fitzgerald, Guang-Ping Gao, Arturo Reyes-Sandoval, George N. Pavlakis, Zhi Q. Xiang, Anthony P. Wlazlo, Wynetta Giles-Davis, James M. Wilson, and Hildegund C. J. Ertl. A Simian Replication-Defective Adenoviral Recombinant Vaccine to HIV-1 Gag. *The Journal of Immunology*, 170(3):1416–1422, February 2003. doi: 10.4049/jimmunol.170.3.1416. Publisher: American Association of Immunologists Section: HOST DEFENSE.

[76] Ensheng Dong, Hongru Du, and Lauren Gardner. An interactive web-based dashboard to track COVID-19 in real time. 20(5):533–534. doi: 10.1016/S1473-3099(20)30120-1.

[77] The coronavirus effect on global economic sentiment, september 2021, .

[78] Neeltje van Doremalen, Elaine Haddock, Friederike Feldmann, Kimberly Meade-White, Trenton Bushmaker, Robert J. Fischer, Atsushi Okumura, Patrick W. Hanley, Greg Saturday, Nick J. Edwards, Madeleine H. A. Clark, Teresa Lambe, Sarah C. Gilbert, and Vincent J. Munster. A single dose of ChAdOx1 MERS provides protective immunity in rhesus macaques. 6(24):eaba8399. doi: 10.1126/sciadv.aba8399.

[79] THE COVAX FACILITY: INTERIM DISTRIBUTION FORECAST - latest as of 3 february 2021, .

[80] Tom Randall, Cedrick Sam, Andre Tartar, and Christopher Cannon. Covid-19 deals tracker: 9.6 billion doses under contract.

[81] Xiaohua Zhang, Liqing Chen, Daniel P. Bancroft, C. K. Lai, and Theodore E. Maione. Crystal structure of recombinant human platelet factor 4. 33(27): 8361–8366, . doi: 10.1021/bi00193a025.

[82] T. F. Deuel, P. S. Keim, M. Farmer, and R. L. Heinrikson. Amino acid sequence of human platelet factor 4. 74(6):2256–2258. doi: 10.1073/pnas.74.6.2256.

[83] R Eisman, S Surrey, B Ramachandran, E Schwartz, and M Poncz. Structural and functional comparison of the genes for human platelet factor 4 and PF4alt. 76(2): 336–344. doi: 10.1182/blood.V76.2.336.336.

[84] Rodger E. Weismann. Arterial embolism occurring during systemic heparin therapy. 76(2):219. doi: 10.1001/archsurg.1958.01280200041005.

[85] I Ahmed, A Majeed, and R Powell. Heparin induced thrombocytopenia: diagnosis and management update. *Postgraduate Medical Journal*, 83(983):575–582, September 2007. doi: 10.1136/pgmj.2007.059188.

[86] Zheng Cai, Serge V. Yarovoi, Zhiqiang Zhu, Lubica Rauova, Vincent Hayes, Tatiana Lebedeva, Qun Liu, Mortimer Poncz, Gowthami Arepally, Douglas B. Cines, and Mark I. Greene. Atomic description of the immune complex involved in heparin-induced thrombocytopenia. 6(1):8277. doi: 10.1038/ncomms9277.

[87] Theodore E. Warkentin. Drug-induced immune-mediated thrombocytopenia — from purpura to thrombosis. 356(9):891–893. doi: 10.1056/NEJMp068309.

[88] Yifan Cheng, Nikolaus Grigorieff, Pawel A. Penczek, and Thomas Walz. A primer to single-particle cryo-electron microscopy. 161(3):438–449. doi: 10.1016/j.cell.2015.03.050.

[89] E. V. Orlova and H. R. Saibil. Structural analysis of macromolecular assemblies by electron microscopy. 111(12):7710–7748. doi: 10.1021/cr100353t.

[90] Eva Nogales and Sjors H.W. Scheres. Cryo-EM: A unique tool for the visualization of macromolecular complexity. 58(4):677–689. doi: 10.1016/j.molcel.2015.02.019.

[91] Sjors H. W. Scheres and Shaoxia Chen. Prevention of overfitting in cryo-EM structure determination. *Nature Methods*, 9(9):853–854, September 2012. doi: 10.1038/nmeth.2115. Number: 9 Publisher: Nature Publishing Group.

[92] Sjors H.W. Scheres. RELION: Implementation of a Bayesian approach to cryo-EM structure determination. *Journal of Structural Biology*, 180(3):519–530, December 2012. doi: 10.1016/j.jsb.2012.09.006.

[93] S H W Scheres. *Processing of Structurally Heterogeneous Cryo-EM Data in RELION*, volume 579. Elsevier Inc., 1 edition. doi: 10.1016/bs.mie.2016.04.012.

[94] Dorothee Liebschner, Pavel V. Afonine, Matthew L. Baker, Gábor Bunkóczi, Vincent B. Chen, Tristan I. Croll, Bradley Hintze, Li-Wei Hung, Swati Jain, Airlie J. McCoy, Nigel W. Moriarty, Robert D. Oeffner, Billy K. Poon, Michael G. Prisant, Randy J. Read, Jane S. Richardson, David C. Richardson, Massimo D. Sammito, Oleg V. Sobolev, Duncan H. Stockwell, Thomas C. Terwilliger, Alexandre G. Urzhumtsev, Lizbeth L. Videau, Christopher J. Williams, and Paul D. Adams. Macromolecular structure determination using x-rays, neutrons and electrons: recent developments in *Phenix*. 75(10):861–877. doi: 10.1107/S2059798319011471.

[95] T. I. Croll. ISOLDE: a physically realistic environment for model building into low-resolution electron-density maps. *Acta Crystallographica Section D: Structural Biology*, 74(6):519–530, June 2018. doi: 10.1107/S2059798318002425. Number: 6 Publisher: International Union of Crystallography.

[96] P. Emsley and K. Cowtan. Coot: model-building tools for molecular graphics. 60 (12):2126–2132. doi: 10.1107/S0907444904019158.

[97] Abhishek Singharoy, Ivan Teo, Ryan McGreevy, John E Stone, Jianhua Zhao, and Klaus Schulten. Molecular dynamics-based refinement and validation for sub-5 Å cryo-electron microscopy maps. *eLife*, 5:e16105, July 2016. doi: 10.7554/eLife.16105. Publisher: eLife Sciences Publications, Ltd.

[98] Rafael Fernandez-Leiro and Sjors H. W. Scheres. Unravelling biological macromolecules with cryo-electron microscopy. 537(7620):339–346. doi: 10.1038/nature19948.

[99] Marc Adrian, Jacques Dubochet, Jean Lepault, and Alasdair McDowall. Cryo-electron microscopy of viruses. 308:32–36.

[100] Vijay S. Reddy, S. Kundhavai Natchiar, Phoebe L. Stewart, and Glen R. Nemerow. Crystal structure of human adenovirus at 3.5 Å resolution. 329(5995):1071–1075. doi: 10.1126/science.1187292.

[101] Xiaodi Yu, David Veesler, Melody G. Campbell, Mary E. Barry, Francisco J. Asturias, Michael A. Barry, and Vijay S. Reddy. Cryo-EM structure of human adenovirus D26 reveals the conservation of structural organization among human adenoviruses. *Science Advances*, 3(5):e1602670, May 2017. doi: 10.1126/sciadv.1602670.

[102] Xinghong Dai, Lily Wu, Ren Sun, and Z. Hong Zhou. Atomic Structures of Minor Proteins VI and VII in Human Adenovirus. *Journal of Virology*, 91(24), December 2017. doi: 10.1128/JVI.00850-17. Publisher: American Society for Microbiology Journals Section: Structure and Assembly.

[103] Peter A. Leong, Xuekui Yu, Z. Hong Zhou, and Grant J. Jensen. Correcting for the ewald sphere in high-resolution single-particle reconstructions. In *Methods in Enzymology*, volume 482, pages 369–380. Elsevier. ISBN 978-0-12-384991-5. doi: 10.1016/S0076-6879(10)82015-4.

[104] J. Bernard Heymann and David M. Belnap. Bsoft: Image processing and molecular modeling for electron microscopy. 157(1):3–18. doi: 10.1016/j.jsb.2006.06.006.

[105] Guang Tang, Liwei Peng, Philip R. Baldwin, Deepinder S. Mann, Wen Jiang, Ian Rees, and Steven J. Ludtke. EMAN2: An extensible image processing suite for electron microscopy. 157(1):38–46. doi: 10.1016/j.jsb.2006.05.009.

[106] K. Wennerberg, K. L. Rossman, and C. J. Der. The ras superfamily at a glance. 118: 843–6. doi: 10.1242/jcs.01660.

[107] K. L. Rossman, C. J. Der, and J. Sondek. GEF means go: turning on RHO GTPases with guanine nucleotide-exchange factors. 6(2):167–80. doi: 10.1038/nrm1587.

[108] Delinasios. Rho/ROCK and MAPK signaling pathways are involved in glioblastoma cell migration and proliferation. pages 1–5.

[109] S. P. Ngok, W. H. Lin, and P. Z. Anastasiadis. Establishment of epithelial polarity–GEF who's minding the GAP? 127:3205–15, . doi: 10.1242/jcs.153197.

[110] S. Hanna and M. El-Sibai. Signaling networks of rho GTPases in cell motility. 25 (10):1955–61. doi: 10.1016/j.cellsig.2013.04.009.

[111] O. Pertz, L. Hodgson, R. L. Klemke, and K. M. Hahn. Spatiotemporal dynamics of RhoA activity in migrating cells. 440(7087):1069–72. doi: 10.1038/nature04665.

[112] D. Vigil, J. Cherfils, K. L. Rossman, and C. J. Der. Ras superfamily GEFs and GAPs: validated and tractable targets for cancer therapy? 10(12):842–57. doi: 10.1038/nrc2960.

[113] J. Cherfils and M. Zeghouf. Regulation of small GTPases by GEFs, GAPs, and GDIs. 93(1):269–309, . doi: 10.1152/physrev.00003.2012.

[114] J. Cherfils and M. Zeghouf. Chronicles of the GTPase switch. 7(8):493–5, . doi: 10.1038/nchembio.608.

[115] I. R. Vetter and A. Wittinghofer. The guanine nucleotide-binding switch in three dimensions. 294(5545):1299–304. doi: 10.1126/science.1062023.

[116] A. P. Wheeler and A. J. Ridley. Why three rho proteins? RhoA, RhoB, RhoC, and cell motility. 301(1):43–9. doi: 10.1016/j.yexcr.2004.08.012.

[117] P. A. Konstantinopoulos, M. V. Karamouzis, and A. G. Papavassiliou. Post-translational modifications and regulation of the RAS superfamily of GTPases as anticancer targets. 6(7):541–55. doi: 10.1038/nrd2221.

[118] P. Fort and A. Blangy. The evolutionary landscape of dbl-like RhoGEF families: Adapting eukaryotic cells to environmental signals. 9(6):1471–1486. doi: 10.1093/gbe/evx100.

[119] Gerald R. Hammond and Yang Hong. Phosphoinositides and membrane targeting in cell polarity. 10(2):a027938. doi: 10.1101/cshperspect.a027938.

[120] G. R. Hammond and T. Balla. Polyphosphoinositide binding domains: Key to inositol lipid biology. 1851(6):746–58. doi: 10.1016/j.bbalip.2015.02.013.

[121] Quinn T Ostrom, Gino Cioffi, Haley Gittleman, Nirav Patil, Kristin Waite, Carol Kruchko, and Jill S Barnholtz-Sloan. CBTRUS statistical report: Primary brain and other central nervous system tumors diagnosed in the united states in 2012–2016. 21: v1–v100. doi: 10.1093/neuonc/noz150.

[122] Mustafa Khasraw, Malaka S Ameratunga, Robin Grant, Helen Wheeler, and Nick Pavlakis. Antiangiogenic therapy for high-grade glioma. doi: 10.1002/14651858.CD008218.pub3.

[123] O. Gallego. Nonsurgical treatment of recurrent glioblastoma. 22(4):e273–81. doi: 10.3747/co.22.2436.

[124] M. K. Garnaas, K. L. Moodie, M. L. Liu, G. V. Samant, K. Li, R. Marx, J. M. Baraban, A. Horowitz, and R. Ramchandran. Syx, a RhoA guanine exchange factor, is essential for angiogenesis in vivo. 103(7):710–6. doi: 10.1161/CIRCRESAHA.108.181388.

[125] S. P. Ngok, R. Geyer, A. Kourtidis, P. Storz, and P. Z. Anastasiadis. Phosphorylation-mediated 14-3-3 protein binding regulates the function of the rho-specific guanine nucleotide exchange factor (RhoGEF) syx. 288(9):6640–50, . doi: 10.1074/jbc.M112.432682.

[126] M. Jaiswal, L. Gremer, R. Dvorsky, L. C. Haeusler, I. C. Cirstea, K. Uhlenbrock, and M. R. Ahmadian. Mechanistic insights into specificity, activity, and regulatory elements of the regulator of g-protein signaling (RGS)-containing rho-specific guanine nucleotide exchange factors (GEFs) p115, PDZ-RhoGEF (PRG), and leukemia-associated RhoGEF (LARG). 286(20):18202–12, . doi: 10.1074/jbc.M111.226431.

[127] G. M. Gasmi-Seabrook, C. B. Marshall, M. Cheung, B. Kim, F. Wang, Y. J. Jang, T. W. Mak, V. Stambolic, and M. Ikura. Real-time NMR study of guanine nucleotide exchange and activation of RhoA by PDZ-RhoGEF. 285(8):5137–45. doi: 10.1074/jbc.M109.064691.

[128] K. L. Rossman and J. Sondek. Larger than dbl: new structural insights into RhoA activation. 30(4):163–5. doi: 10.1016/j.tibs.2005.02.002.

[129] X. Shang, F. Marchioni, N. Sipes, C. R. Evelyn, M. Jerabek-Willemsen, S. Duhr, W. Seibel, M. Wortman, and Y. Zheng. Rational design of small molecule inhibitors targeting RhoA subfamily rho GTPases. 19(6):699–710. doi: 10.1016/j.chembiol.2012.05.009.

[130] U. Derewenda, A. Oleksy, A. S. Stevenson, J. Korczynska, Z. Dauter, A. P. Somlyo, J. Otlewski, A. V. Somlyo, and Z. S. Derewenda. The crystal structure of RhoA in complex with the DH/PH fragment of PDZRhoGEF, an activator of the ca(2+) sensitization pathway in smooth muscle. 12(11):1955–65. doi: 10.1016/j.str.2004.09.003.

[131] J. C. Dachsel, S. P. Ngok, L. J. Lewis-Tuffin, A. Kourtidis, R. Geyer, L. Johnston, R. Feathers, and P. Z. Anastasiadis. The rho guanine nucleotide exchange factor syx regulates the balance of dia and ROCK activities to promote polarized-cancer-cell migration. 33(24):4909–18. doi: 10.1128/MCB.00565-13.

[132] S. P. Ngok and P. Z. Anastasiadis. Rho GEFs in endothelial junctions: Effector selectivity and signaling integration determine junctional response. 1(5):e27132. doi: 10.4161/tisb.27132.

[133] S. P. Ngok, R. Geyer, M. Liu, A. Kourtidis, S. Agrawal, C. Wu, H. R. Seerapu, L. J. Lewis-Tuffin, K. L. Moodie, D. Huveldt, R. Marx, J. M. Baraban, P. Storz, A. Horowitz, and P. Z. Anastasiadis. VEGF and angiopoietin-1 exert opposing effects on cell junctions by regulating the rho GEF syx. 199(7):1103–15, . doi: 10.1083/jcb.201207009.

[134] Maheshi N. Ramasamy, Angela M. Minassian, Katie J. Ewer, Amy L. Flaxman, Pedro M. Folegatti, Daniel R. Owens, Merryn Voysey, Parvinder K. Aley, Brian Angus, Gavin Babbage, Sandra Belij-Rammerstorfer, Lisa Berry, Sagida Bibi, Mustapha Bittaye, Katrina Cathie, Harry Chappell, Sue Charlton, Paola Cicconi, Elizabeth A. Clutterbuck, Rachel Colin-Jones, Christina Dold, Katherine R. W. Emary, Sofiya Fedosyuk, Michelle Fuskova, Diane Gbesemete, Catherine Green, Bassam Hallis, Mimi M. Hou, Daniel Jenkin, Carina C. D. Joe, Elizabeth J. Kelly, Simon Kerridge, Alison M. Lawrie, Alice Lelliott, May N. Lwin, Rebecca Makinson, Natalie G. Marchevsky, Yama Mujadidi, Alasdair P. S. Munro, Mihaela Pacurar, Emma Plested, Jade Rand, Thomas Rawlinson, Sarah Rhead, Hannah Robinson, Adam J. Ritchie, Amy L. Ross-Russell, Stephen Saich, Nisha Singh, Catherine C. Smith, Matthew D. Snape, Rinn Song, Richard Tarrant, Yrene Themistocleous, Kelly M. Thomas, Tonya L. Villafana, Sarah C. Warren, Marion E. E. Watson, Alexander D. Douglas, Adrian V. S. Hill, Teresa Lambe, Sarah C. Gilbert, Saul N. Faust, Andrew J. Pollard, Jeremy Aboagye, Kelly Adams, Aabidah Ali, Elizabeth R. Allen, Lauren Allen, Jennifer L. Allison, Foteini Andritsou, Rachel Anslow, Edward H. Arbe-Barnes, Megan Baker, Natalie Baker, Philip Baker, Ioana Baleanu, Debbie Barker, Eleanor Barnes, Jordan R. Barrett, Kelly Barrett, Louise Bates, Alexander Batten, Kirsten Beadon, Rebecca Beckley, Duncan Bellamy, Adam Berg, Laura Bermejo, Eleanor Berrie, Amy Beveridge, Kevin Bewley, Else M. Bijker, Geeta Birch, Luke Blackwell, Heather Bletchly, Caitlin L. Blundell, Susannah R. Blundell, Emma Bolam, Elena Boland, Daan Bormans, Nicola Borthwick, Konstantinos Boukas, Thomas Bower, Francesca Bowring, Amy

Boyd, Tanja Brenner, Phillip Brown, Charlie Brown-O'Sullivan, Scott Bruce, Emily Brunt, Jamie Burbage, Joshua Burgoyne, Karen R. Buttigieg, Nicholas Byard, Ingrid Cabera Puig, Susana Camara, Michelangelo Cao, Federica Cappuccini, Melanie Carr, Miles W. Carroll, Paul Cashen, Ana Cavey, Jim Chadwick, Ruth Challis, David Chapman, David Charles, Irina Chelysheva, Jee-Sun Cho, Liliana Cifuentes, Elizabeth Clark, Sarah Collins, Christopher P. Conlon, Naomi S. Coombes, Rachel Cooper, Cushla Cooper, Wendy E. M. Crocker, Sarah Crosbie, Dan Cullen, Christina Cunningham, Fiona Cuthbertson, Brad E. Datoo, Lynne Dando, Mehreen S. Datoo, Chandrabali Datta, Hannah Davies, Sarah Davies, Elizabeth J. Davis, Judith Davis, David Dearlove, Tesfaye Demissie, Stefania Di Marco, Claudio Di Maso, Danielle DiTirro, Claire Docksey, Tao Dong, Francesca R. Donnellan, Naomi Douglas, Charlotte Downing, Jonathan Drake, Rachael Drake-Brockman, Ruth E. Drury, Susanna J. Dunachie, Christopher J. Edwards, Nick J. Edwards, Omar El Muhanna, Sean C. Elias, Ryan S. Elliott, Michael J. Elmore, Marcus Rex English, Sally Felle, Shuo Feng, Carla Ferreira Da Silva, Samantha Field, Richard Fisher, Carine Fixmer, Karen J. Ford, Jamie Fowler, Emma Francis, John Frater, Julie Furze, Pablo Galian-Rubio, Celine Galloway, Harriet Garlant, Madita Gavrila, Felicity Gibbons, Karyna Gibbons, Ciaran Gilbride, Hardeep Gill, Kerry Godwin, Katherine Gordon-Quayle, Giacomo Gorini, Lyndsey Goulston, Caroline Grabau, Lara Gracie, Nichola Graham, Nicola Greenwood, Oliver Griffiths, Gaurav Gupta, Elizabeth Hamilton, Brama Hanumunthadu, Stephanie A. Harris, Tara Harris, Daisy Harrison, Thomas C. Hart, Birgit Hartnell, Louise Haskell, Sophia Hawkins, John Aaron Henry, Macarena Hermosin Herrera, David Hill, Jennifer Hill, Gina Hodges, Susanne H. C. Hodgson, Katie L. Horton, Elizabeth Howe, Nicola Howell, Jessica Howes, Ben Huang, Jonathan Humphreys, Holly E. Humphries, Poppy Iveson, Frederic Jackson, Susan Jackson, Sam Jauregui, Helen Jeffers, Bryony Jones, Christine E. Jones, Elizabeth Jones, Kathryn Jones, Amar Joshi, Reshma Kailath, Jade Keen, Dearbhla M. Kelly, Sarah Kelly, Debbie Kelly, David Kerr, Liaquat Khan, Baktash Khozoee, Annabel Killen, Jasmin Kinch, Lloyd D. W. King, Thomas B. King, Lucy Kingham, Paul Klenerman, Julian C. Knight, Daniel Knott, Stanislava Koleva, Gail Lang, Colin W. Larkworthy, Jessica P. J. Larwood, Rebecca Law, Arlene Lee, Kim Y. N. Lee, Emily A. Lees, Stephanie Leung, Yuanyuan Li, Amelia M. Lias, Aline Linder, Samuel Lipworth, Shuchang Liu, Xinxue Liu, Stephanie Lloyd, Lisa Loew, Raquel Lopez Ramon, Meera Madhavan, David O. Mainwaring, Garry Mallett, Kushal Mansatta, Spyridoula Marinou, Phedra Marius, Emma Marlow, Paula Marriott, Julia L. Marshall, Jane Martin, Shauna Masters, Joanne McEwan, Joanna L. McGlashan, Lorna McInroy, Nicky McRobert, Clare Megson, Alexander J. Mentzer, Neginsadat Mirtorabi, Celia Mitton, Maria Moore, Marni Moran, Ella Morey, Róisín Morgans, Susan J. Morris, Hazel Morrison Morrison, Gertraud Morshead, Richard Morter, Nathifa A. Moya, Ekta Mukhopadhyay, Jilly Muller, Claire Munro, Sarah Murphy, Philomena Mweu, Andrés Noé, Fay L. Nugent, Katie O'Brien, Daniel O'Connor, Blanché Oguti, Victoria Olchawski, Catarina Oliveira, Peter John O'Reilly, Piper Osborne, Lydia Owen, Nelly Owino, Panagiotis Papageorgiou, Helena Parracho, Karen Parsons, Bhumika Patel, Maia Patrick-Smith, Yanchun Peng, Elizabeth J. Penn, Marco Polo Peralta-Alvarez, James Perring, Christos Petropoulos, Daniel J. Phillips, Dimitra Pipini, Samuel Pollard, Ian Poulton, Danny Pratt, Laura Presland, Pamela C. Proud,

Samuel Provstgaard-Morys, Sophie Pueschel, David Pulido, Ria Rabara, Kajal Radia, Durga Rajapaska, Fernando Ramos Lopez, Helen Ratcliffe, Sara Rayhan, Byron Rees, Emilia Reyes Pabon, Hannah Roberts, Isla Robertson, Sophie Roche, Christine S. Rollier, Rossana Romani, Zoe Rose, Indra Rudiansyah, Sabeha Sabheha, Stephannie Salvador, Helen Sanders, Katherine Sanders, Iman Satti, Chloe Sayce, Annina B. Schmid, Ella Schofield, Gavin Screaton, Cynthia Sedik, Samiullah Seddiqi, Rameswara R. Segireddy, Beatrice Selby, Imam Shaik, Hannah R. Sharpe, Robert Shaw, Adam Shea, Sarah Silk, Laura Silva-Reyes, Donal T. Skelly, David J. Smith, Daniel C. Smith, Nicholas Smith, Alexandra J. Spencer, Louise Spoors, Elizabeth Stafford, Imogen Stamford, Lisa Stockdale, David Stockley, Lisa V. Stockwell, Matthew Stokes, Louise H. Strickland, Arabella Stuart, Sulaiman Sulaiman, Eloise Summerton, Zoe Swash, Anna Szigeti, Abdessamad Tahiri-Alaoui, Rachel Tanner, Iona Taylor, Keja Taylor, Ursula Taylor, Rebecca te Water Naude, Andreas Themistocleous, Merin Thomas, Tonia M. Thomas, Amber Thompson, Kevin Thompson, Viv Thornton-Jones, Lan Tinh, Adriana Tomic, Susan Tonks, James Towner, Nguyen Tran, Julian A. Tree, Adam Truby, Cheryl Turner, Richard Turner, Marta Ulaszewska, Rachel Varughese, Dennis Verbart, Marije K. Verheul, Iason Vichos, Laura Walker, Matthew E. Wand, Bridget Watkins, Jessica Welch, Alison J. West, Caroline White, Rachel White, Paul Williams, Mark Woodyer, Andrew T. Worth, Daniel Wright, Terri Wrin, Xin Li Yao, Diana-Andreea Zbarcea, and Dalila Zizi. Safety and immunogenicity of ChAdOx1 nCoV-19 vaccine administered in a prime-boost regimen in young and old adults (COV002): a single-blind, randomised, controlled, phase 2/3 trial. *The Lancet*, 396(10267):1979–1993, December 2020. doi: 10.1016/S0140-6736(20)32466-1. Publisher: Elsevier.

[135] Andreas Greinacher, Kathleen Selleng, Jan Wesche, Stefan Handtke, Raghavendra Palankar, Konstanze Aurich, Michael Lalk, Karen Methling, Uwe Völker, Christian Hentschker, Stephan Michalik, Leif Steil, Linda Schönborn, Martin Beer, Kati Franzke, Chandini Rangaswamy, Reiner K. Mailer, Thomas Thiele, Stefan Kochanek, Lea Krutzke, Florian Siegerist, Nicole Endlich, Theodore E. Warkentin, and Thomas Renné. Towards Understanding ChAdOx1 nCov-19 Vaccine-induced Immune Thrombotic Thrombocytopenia (VITT). Technical report, August 2021. ISSN: 2693-5015 Type: article.

[136] Andreas Greinacher, Thomas Thiele, Theodore E. Warkentin, Karin Weisser, Paul A. Kyrle, and Sabine Eichinger. Thrombotic Thrombocytopenia after ChAdOx1 nCov-19 Vaccination. *New England Journal of Medicine*, 0(0):null, April 2021. doi: 10.1056/NEJMoa2104840. Publisher: Massachusetts Medical Society _eprint: https://doi.org/10.1056/NEJMoa2104840.

[137] Keith R. McCrae. Thrombotic thrombocytopenia due to SARS-CoV-2 vaccination. *Cleveland Clinic Journal of Medicine*, May 2021. doi: 10.3949/ccjm.88a.ccc078. Publisher: Cleveland Clinic Journal of Medicine Section: COVID-19 Curbside Consults.

[138] Prakash Bhuyan, Jennie Medin, Hugo Gomes da Silva, Madhavi Yadavalli, Nirmal Kumar Shankar, Hana Mullerova, Matthew Arnold, and Magnus Nord. Very rare thrombosis with thrombocytopenia after second AZD1222 dose: a global safety

database analysis. *The Lancet*, 0(0), July 2021. doi: 10.1016/S0140-6736(21)01693-7. Publisher: Elsevier.

[139] Kate-Lynn Muir, Avyakta Kallam, Scott A. Koepsell, and Krishna Gundabolu. Thrombotic Thrombocytopenia after Ad26.COV2.S Vaccination. *New England Journal of Medicine*, 0(0):null, April 2021. doi: 10.1056/NEJMc2105869. Publisher: Massachusetts Medical Society _eprint: https://doi.org/10.1056/NEJMc2105869.

[140] Towards Understanding ChAdOx1 nCov-19 Vaccine-induced Immune Thrombotic Thrombocytopenia (VITT), April 2021.

[141] Maha Othman, Alexander T. Baker, Elena Gupalo, Abdelrahman Elsebaie, Carly M. Bliss, Matthew T. Rondina, David Lillicrap, and Alan L. Parker. To Clot or Not to Clot? Ad is the Question - Insights on Mechanisms Related to Vaccine Induced Thrombotic Thrombocytopenia. *Journal of Thrombosis and Haemostasis*, n/a(n/a). doi: 10.1111/jth.15485. _eprint: https://onlinelibrary.wiley.com/doi/pdf/10.1111/jth.15485.

[142] Ritu R. Bradley, Lori F. Maxfield, Diana M. Lynch, Mark J. Iampietro, Erica N. Borducchi, and Dan H. Barouch. Adenovirus Serotype 5-Specific Neutralizing Antibodies Target Multiple Hexon Hypervariable Regions. *Journal of Virology*, 86 (2):1267–1272, January 2012. doi: 10.1128/JVI.06165-11.

[143] Maha Othman, Andrea Labelle, Ian Mazzetti, Hisham S. Elbatarny, and David Lillicrap. Adenovirus-induced thrombocytopenia: the role of von Willebrand factor and P-selectin in mediating accelerated platelet clearance. *Blood*, 109(7):2832–2839, December 2006. doi: 10.1182/blood-2006-06-032524.

[144] A. L. Parker, S. N. Waddington, S. M. Buckley, J. Custers, M. J. Havenga, N. van Rooijen, J. Goudsmit, J. H. McVey, S. A. Nicklin, and A. H. Baker. Effect of neutralizing sera on factor x-mediated adenovirus serotype 5 gene transfer. *J Virol*, 83:479–83, January 2009. doi: 10.1128/JVI.01878-08.

[145] R. Alba, A. C. Bradshaw, N. Mestre-Francés, J.-M. Verdier, D. Henaff, and A. H. Baker. Coagulation factor X mediates adenovirus type 5 liver gene transfer in non-human primates (*Microcebus murinus*). *Gene Therapy*, 19(1):109–113, January 2012. doi: 10.1038/gt.2011.87.

[146] Hanni Uusi-Kerttula, Mateusz Legut, James Davies, Rachel Jones, Emma Hudson, Louise Hanna, Richard J. Stanton, John D. Chester, and Alan L. Parker. Incorporation of Peptides Targeting EGFR and FGFR1 into the Adenoviral Fiber Knob Domain and Their Evaluation as Targeted Cancer Therapies. *Human Gene Therapy*, 26(5):320–329, May 2015. doi: 10.1089/hum.2015.015.

[147] Jasenko Zivanov, Takanori Nakane, Björn O. Forsberg, Dari Kimanius, Wim Jh Hagen, Erik Lindahl, and Sjors Hw Scheres. New tools for automated high-resolution cryo-EM structure determination in RELION-3. *eLife*, 7, November 2018. doi: 10.7554/eLife.42166.

[148] J. Yang, R. Yan, A. Roy, D. Xu, J. Poisson, and Y. Zhang. The i-TASSER suite: protein structure and function prediction. 12(1):7–8. doi: 10.1038/nmeth.3213.

[149] Andrew Waterhouse, Martino Bertoni, Stefan Bienert, Gabriel Studer, Gerardo Tauriello, Rafal Gumienny, Florian T Heer, Tjaart A P de Beer, Christine Rempfer, Lorenza Bordoli, Rosalba Lepore, and Torsten Schwede. SWISS-MODEL: homology modelling of protein structures and complexes. *Nucleic Acids Research*, 46(W1):W296–W303, July 2018. doi: 10.1093/nar/gky427.

[150] Eric F. Pettersen, Thomas D. Goddard, Conrad C. Huang, Elaine C. Meng, Gregory S. Couch, Tristan I. Croll, John H. Morris, and Thomas E. Ferrin. UCSF ChimeraX: Structure visualization for researchers, educators, and developers. *Protein Science: A Publication of the Protein Society*, 30(1):70–82, January 2021. doi: 10.1002/pro.3943.

[151] Leonardo G. Trabuco, Elizabeth Villa, Kakoli Mitra, Joachim Frank, and Klaus Schulten. Flexible fitting of atomic structures into electron microscopy maps using molecular dynamics. *Structure (London, England: 1993)*, 16(5):673–683, May 2008. doi: 10.1016/j.str.2008.03.005.

[152] Kwok-Yan Chan, James Gumbart, Ryan McGreevy, Jean M. Watermeyer, B. Trevor Sewell, and Klaus Schulten. Symmetry-Restrained Flexible Fitting for Symmetric EM Maps. *Structure*, 19(9):1211–1218, September 2011. doi: 10.1016/j.str.2011.07.017. Publisher: Elsevier.

[153] James C. Phillips, David J. Hardy, Julio D. C. Maia, John E. Stone, João V. Ribeiro, Rafael C. Bernardi, Ronak Buch, Giacomo Fiorin, Jérôme Hénin, Wei Jiang, Ryan McGreevy, Marcelo C. R. Melo, Brian K. Radak, Robert D. Skeel, Abhishek Singharoy, Yi Wang, Benoît Roux, Aleksei Aksimentiev, Zaida Luthey-Schulten, Laxmikant V. Kalé, Klaus Schulten, Christophe Chipot, and Emad Tajkhorshid. Scalable molecular dynamics on CPU and GPU architectures with NAMD. *The Journal of Chemical Physics*, 153(4):044130, July 2020. doi: 10.1063/5.0014475. Publisher: American Institute of Physics.

[154] Robert B. Best, Xiao Zhu, Jihyun Shim, Pedro E. M. Lopes, Jeetain Mittal, Michael Feig, and Alexander D. MacKerell. Optimization of the Additive CHARMM All-Atom Protein Force Field Targeting Improved Sampling of the Backbone □, ψ and Side-Chain χ1 and χ2 Dihedral Angles. *Journal of Chemical Theory and Computation*, 8(9):3257–3273, September 2012. doi: 10.1021/ct300400x. Publisher: American Chemical Society.

[155] W. Humphrey, A. Dalke, and K. Schulten. VMD: visual molecular dynamics. 14 (1):33–8, 27–8. doi: 10.1016/0263-7855(96)00018-5.

[156] Eduard Schreiner, Leonardo G. Trabuco, Peter L. Freddolino, and Klaus Schulten. Stereochemical errors and their implications for molecular dynamics simulations. *BMC Bioinformatics*, 12(1):190, May 2011. doi: 10.1186/1471-2105-12-190.

[157] Eleanor J. Dodson, Martyn Winn, and Adam Ralph. [32] Collaborative computational project, number 4: Providing programs for protein crystallography.

In *Methods in Enzymology*, volume 277 of *Macromolecular Crystallography Part B*, pages 620–633. Academic Press, January 1997. doi: 10.1016/S0076-6879(97)77034-4.

[158] Di Xia, Lynda J. Henry, Robert D. Gerard, and Johann Deisenhofer. Crystal structure of the receptor-binding domain of adenovirus type 5 fiberprotein at 1.7 Å resolution. *Structure*, 2(12):1259–1270, December 1994. doi: 10.1016/S0969-2126(94)00126-X.

[159] P. Emsley and K. Cowtan. Coot: model-building tools for molecular graphics. *Acta Crystallographica Section D: Biological Crystallography*, 60(12):2126–2132, December 2004. doi: 10.1107/S0907444904019158.

[160] Elena Seiradake, Hugues Lortat-Jacob, Olivier Billet, Eric J. Kremer, and Stephen Cusack. Structural and Mutational Analysis of Human Ad37 and Canine Adenovirus 2 Fiber Heads in Complex with the D1 Domain of Coxsackie and Adenovirus Receptor. *Journal of Biological Chemistry*, 281(44):33704–33716, November 2006. doi: 10.1074/jbc.M605316200.

[161] Hongjie Wang, Yen-Chywan Liaw, Daniel Stone, Oleksandr Kalyuzhniy, Imameddin Amiraslanov, Sebastian Tuve, Christophe L. M. J. Verlinde, Dmitry Shayakhmetov, Thilo Stehle, Steve Roffler, and André Lieber. Identification of CD46 binding sites within the adenovirus serotype 35 fiber knob. *Journal of Virology*, 81(23):12785–12792, December 2007. doi: 10.1128/JVI.01732-07.

[162] LLC. Schrödinger. The PyMOL Molecular Graphics System, Version 2.0.

[163] P. Benjamin Stranges and Brian Kuhlman. A comparison of successful and failed protein interface designs highlights the challenges of designing buried hydrogen bonds. *Protein Science: A Publication of the Protein Society*, 22(1):74–82, January 2013. doi: 10.1002/pro.2187.

[164] Kyle A. Barlow, Shane Ó Conchúir, Samuel Thompson, Pooja Suresh, James E. Lucas, Markus Heinonen, and Tanja Kortemme. Flex ddG: Rosetta Ensemble-Based Estimation of Changes in Protein–Protein Binding Affinity upon Mutation. *The Journal of Physical Chemistry B*, 122(21):5389–5399, May 2018. doi: 10.1021/acs.jpcb.7b11367. Publisher: American Chemical Society.

[165] Alexander T. Baker, Alexander Greenshields-Watson, Lynda Coughlan, James A. Davies, Hanni Uusi-Kerttula, David K. Cole, Pierre J. Rizkallah, and Alan L. Parker. Diversity within the adenovirus fiber knob hypervariable loops influences primary receptor interactions. *Nature Communications*, 10(1):741, February 2019. doi: 10.1038/s41467-019-08599-y.

[166] Madeira F, Park Ym, Lee J, Buso N, Gur T, Madhusoodanan N, Basutkar P, Tivey Arn, Potter Sc, Finn Rd, and Lopez R. The EMBL-EBI search and sequence analysis tools APIs in 2019. *Nucleic Acids Research*, 47(W1):W636–W641, July 2019. doi: 10.1093/nar/gkz268.

[167] Chris Maffeo. Atomic Resolution Brownian Dynamics. 2016. doi: https://doi.org/10.4231/D3736M35T.

[168] A. Ortega, D. Amorós, and J. García de la Torre. Prediction of Hydrodynamic and Other Solution Properties of Rigid Proteins from Atomic- and Residue-Level Models. *Biophysical Journal*, 101(4):892–898, August 2011. doi: 10.1016/j.bpj.2011.06.046.

[169] J. Huang, S. Rauscher, G. Nawrocki, T. Ran, M. Feig, B. L. de Groot, H. Grubmuller, and A. D. MacKerell. CHARMM36m: an improved force field for folded and intrinsically disordered proteins. 14(1):71–73. doi: 10.1038/nmeth.4067.

[170] Emma C. Nilsson, Rickard J. Storm, Johannes Bauer, Susanne M. C. Johansson, Aivar Lookene, Jonas Ångström, Mattias Hedenström, Therese L. Eriksson, Lars Frängsmyr, Simon Rinaldi, Hugh J. Willison, Fatima Pedrosa Domellöf, Thilo Stehle, and Niklas Arnberg. The GD1a glycan is a cellular receptor for adenoviruses causing epidemic keratoconjunctivitis. *Nature Medicine*, 17(1):105–109, January 2011. doi: 10.1038/nm.2267.

[171] B. David Persson, Lijo John, Karim Rafie, Michael Strebl, Lars Frängsmyr, Monika Z. Ballmann, Katja Mindler, Menzo Havenga, Angelique Lemckert, Thilo Stehle, Lars-Anders Carlson, and Niklas Arnberg. Human species D adenovirus hexon capsid protein mediates cell entry through a direct interaction with CD46. *Proceedings of the National Academy of Sciences*, 118(3), January 2021. doi: 10.1073/pnas.2020732118. Publisher: National Academy of Sciences Section: Biological Sciences.

[172] Elena Ortiz-Zapater, George Santis, and Maddy Parsons. CAR: A key regulator of adhesion and inflammation. *The International Journal of Biochemistry & Cell Biology*, 89:1–5, August 2017. doi: 10.1016/j.biocel.2017.05.025.

[173] Tissue expression of DSG2 - Summary - The Human Protein Atlas, .

[174] Elena Gupalo, Liudmila Buriachkovskaia, and Maha Othman. Human platelets express CAR with localization at the sites of intercellular interaction. *Virology Journal*, 8:456, September 2011. doi: 10.1186/1743-422X-8-456.

[175] Robert C. Carlisle, Ying Di, Anna M. Cerny, Andreas F.-P. Sonnen, Robert B. Sim, Nicola K. Green, Vladimir Subr, Karel Ulbrich, Robert J. C. Gilbert, Kerry D. Fisher, Robert W. Finberg, and Leonard W. Seymour. Human erythrocytes bind and inactivate type 5 adenovirus by presenting Coxsackie virus-adenovirus receptor and complement receptor 1. *Blood*, 113(9):1909–1918, February 2009. doi: 10.1182/blood-2008-09-178459.

[176] Daniel Stone, Ying Liu, Dmitry Shayakhmetov, Zong-Yi Li, Shaoheng Ni, and André Lieber. Adenovirus-Platelet Interaction in Blood Causes Virus Sequestration to the Reticuloendothelial System of the Liver. *Journal of Virology*, 81(9): 4866–4871, May 2007. doi: 10.1128/JVI.02819-06. Publisher: American Society for Microbiology Journals Section: GENE DELIVERY.

[177] Jay N. Lozier, Gyorgy Csako, Traci H. Mondoro, D.m. Krizek, Mark E. Metzger, Rene Costello, Jaroslav G. Vostal, M.e. Rick, Robert E. Donahue, and Richard A. Morgan. Toxicity of a First-Generation Adenoviral Vector in Rhesus Macaques. *Human Gene Therapy*, 13(1):113–124, January 2002. doi: 10.1089/10430340152712665. Publisher: Mary Ann Liebert, Inc., publishers.

[178] Angela C. Bradshaw, Alan L. Parker, Margaret R. Duffy, Lynda Coughlan, Nico van Rooijen, Veli-Matti Kähäri, Stuart A. Nicklin, and Andrew H. Baker. Requirements for Receptor Engagement during Infection by Adenovirus Complexed with Blood Coagulation Factor X. *PLOS Pathogens*, 6(10):e1001142, October 2010. doi: 10.1371/journal.ppat.1001142.

[179] A Prothrombotic Thrombocytopenic Disorder Resembling Heparin-Induced Thrombocytopenia Following Coronavirus-19 Vaccination, March 2021.

[180] Tom Shimabukuro. Update: Thrombosis with thrombocytopenia syndrome (TTS) following COVID-19 vaccination, May 2021.

[181] Thi-Huong Nguyen, Nikolay Medvedev, Mihaela Delcea, and Andreas Greinacher. Anti-platelet factor 4/polyanion antibodies mediate a new mechanism of autoimmunity. *Nature Communications*, 8(1):14945, May 2017. doi: 10.1038/ncomms14945. Number: 1 Publisher: Nature Publishing Group.

[182] P. Chen, I. Kovesdi, and J. T. Bruder. Effective repeat administration with adenovirus vectors to the muscle. *Gene Therapy*, 7(7):587–595, April 2000. doi: 10.1038/sj.gt.3301137. Bandiera_abtest: a Cg_type: Nature Research Journals Number: 7 Primary_atype: Research Publisher: Nature Publishing Group.

[183] Leo Nicolai, Alexander Leunig, Kami Pekayvaz, Afra Anjum, Eva Riedlinger, Luke Eivers, Marie-Louise Hoffknecht, Dario Rossaro, Raphael Escaig, Rainer Kaiser, Vivien Polewka, Anna Titova, Karsten Spiekermann, Matteo Iannacone, Konstantin Stark, and Steffen Massberg. Thrombocytopenia and splenic platelet directed immune responses after intravenous ChAdOx1 nCov-19 administration. *bioRxiv*, page 2021.06.29.450356, June 2021. doi: 10.1101/2021.06.29.450356. Publisher: Cold Spring Harbor Laboratory Section: New Results.

[184] Tomohiro Kurosaki, Kohei Kometani, and Wataru Ise. Memory B cells. *Nature Reviews Immunology*, 15(3):149–159, March 2015. doi: 10.1038/nri3802. Number: 3 Publisher: Nature Publishing Group.

[185] Coronavirus vaccine - weekly summary of Yellow Card reporting, .

[186] Janssen COVID-19 Emergency Use Authorization (EUA) Official Website, .

[187] Guidance for clinical case management of thrombosis with thrombocytopenia syndrome(TTS) following vaccination to prevent coronavirus disease (COVID-19), .

[188] Lynda Coughlan, Angela C Bradshaw, Alan L Parker, Hollie Robinson, Katie White, Jerome Custers, Jaap Goudsmit, Nico Van Roijen, Dan H Barouch, Stuart A Nicklin, and Andrew H Baker. Ad5:Ad48 Hexon Hypervariable Region Substitutions Lead to Toxicity and Increased Inflammatory Responses Following Intravenous Delivery. *Molecular Therapy*, 20(12):2268–2281, December 2012. doi: 10.1038/mt.2012.162.

[189] Vahid Abrishami, Serban L. Ilca, Josue Gomez-Blanco, Ilona Rissanen, José Miguel de la Rosa-Trevín, Vijay S. Reddy, José-Maria Carazo, and Juha T. Huiskonen. Localized reconstruction in Scipion expedites the analysis of symmetry mismatches in cryo-EM data. *Progress in Biophysics and Molecular Biology*, 160:43–52, March 2021. doi: 10.1016/j.pbiomolbio.2020.05.004.

[190] M. Blank, A. Eldor, S. Tavor, L. Ziporen, D. B. Cines, G. Arepally, A. Afek, and Y. Shoenfeld. A mouse model for heparin-induced thrombocytopenia. 36(1):12–16.

[191] M. P. Reilly, S. M. Taylor, C. Franklin, B. S. Sachais, D. B. Cines, K. J. Williams, and S. E. Mckenzie. Prothrombotic factors enhance heparin-induced thrombocytopenia and thrombosis *in vivo* in a mouse model. 4(12):2687–2694. doi: 10.1111/j.1538-7836.2006.02201.x.

[192] J. M. Ostrem, U. Peters, M. L. Sos, J. A. Wells, and K. M. Shokat. K-ras(g12c) inhibitors allosterically control GTP affinity and effector interactions. 503(7477): 548–51. doi: 10.1038/nature12796.

[193] J. T. Snyder, D. K. Worthylake, K. L. Rossman, L. Betts, W. M. Pruitt, D. P. Siderovski, C. J. Der, and J. Sondek. Structural basis for the selective activation of rho GTPases by dbl exchange factors. 9(6):468–75. doi: 10.1038/nsb796.

[194] E. Sahai and C. J. Marshall. ROCK and dia have opposing effects on adherens junctions downstream of rho. 4(6):408–15. doi: 10.1038/ncb796.

[195] M. Jaiswal, R. Dvorsky, and M. R. Ahmadian. Deciphering the molecular and functional basis of dbl family proteins: a novel systematic approach toward classification of selective activation of the rho family proteins. 288(6):4486–500, . doi: 10.1074/jbc.M112.429746.

[196] J. E. Harlan, H. S. Yoon, P. J. Hajduk, and S. W. Fesik. Structural characterization of the interaction between a pleckstrin homology domain and phosphatidylinositol 4,5-bisphosphate. 34(31):9859–64, . doi: 10.1021/bi00031a006.

[197] J E Harlan, P J Hajduk, H S Yoon, and S W Fesik. Pleckstrin homology domains bind to phosphatidylinositol-4,5-bisphosphate. 371(6493):168–170, . doi: 10.1038/371168a0.

[198] Z. Chen, L. Guo, S. R. Sprang, and P. C. Sternweis. Modulation of a GEF switch: autoinhibition of the intrinsic guanine nucleotide exchange activity of p115-RhoGEF. 20(1):107–17. doi: 10.1002/pro.542.

[199] N. S. Roy, M. E. Yohe, P. A. Randazzo, and J. M. Gruschus. Allosteric properties of PH domains in arf regulatory proteins. 6(2):e1181700. doi: 10.1080/21592799.2016.1181700.

[200] X. Jian, J. M. Gruschus, E. Sztul, and P. A. Randazzo. The pleckstrin homology (PH) domain of the arf exchange factor brag2 is an allosteric binding site. 287(29): 24273–83, . doi: 10.1074/jbc.M112.368084.

[201] J. A. Bielnicki, A. V. Shkumatov, U. Derewenda, A. V. Somlyo, D. I. Svergun, and Z. S. Derewenda. Insights into the molecular activation mechanism of the RhoA-specific guanine nucleotide exchange factor, PDZRhoGEF. 286(40):35163–75. doi: 10.1074/jbc.M111.270918.

[202] M. Zheng, T. Cierpicki, K. Momotani, M. V. Artamonov, U. Derewenda, J. H. Bushweller, A. V. Somlyo, and Z. S. Derewenda. On the mechanism of autoinhibition of the RhoA-specific nucleotide exchange factor PDZRhoGEF. 9: 36. doi: 10.1186/1472-6807-9-36.

[203] J. Viaud, F. Gaits-Iacovoni, and B. Payrastre. Regulation of the DH-PH tandem of guanine nucleotide exchange factor for rho GTPases by phosphoinositides. 52(2): 303–14. doi: 10.1016/j.jbior.2012.04.001.

[204] P. Aspenstrom. Activated rho GTPases in cancer-the beginning of a new paradigm. 19(12). doi: 10.3390/ijms19123949.

[205] M. Qian, Z. Chen, S. Wang, X. Guo, Z. Zhang, W. Qiu, X. Gao, J. Xu, R. Zhao, H. Xue, and G. Li. PLEKHG5 is a novel prognostic biomarker in glioma patients. 24(11):1350–1358. doi: 10.1007/s10147-019-01503-0.

[206] M. Ernkvist, N. Luna Persson, S. Audebert, P. Lecine, I. Sinha, M. Liu, M. Schlueter, A. Horowitz, K. Aase, T. Weide, J. P. Borg, A. Majumdar, and L. Holmgren. The amot/patj/syx signaling complex spatially controls RhoA GTPase activity in migrating endothelial cells. 113(1):244–53. doi: 10.1182/blood-2008-04-153874.

[207] H. Jubb, A. P. Higueruelo, A. Winter, and T. L. Blundell. Structural biology and drug discovery for protein-protein interactions. 33(5):241–8. doi: 10.1016/j.tips.2012.03.006.

[208] P. Luningschror, B. Binotti, B. Dombert, P. Heimann, A. Perez-Lara, C. Slotta, N. Thau-Habermann, R. von Collenberg C, F. Karl, M. Damme, A. Horowitz, I. Maystadt, A. Fuchtbauer, E. M. Fuchtbauer, S. Jablonka, R. Blum, N. Uceyler, S. Petri, B. Kaltschmidt, R. Jahn, C. Kaltschmidt, and M. Sendtner. Plekhg5-regulated autophagy of synaptic vesicles reveals a pathogenic mechanism in motoneuron disease. 8(1):678. doi: 10.1038/s41467-017-00689-z.

[209] Structural Genomics Consortium, China Structural Genomics Consortium, Northeast Structural Genomics Consortium, S Graslund, P Nordlund, J Weigelt, B M Hallberg, J Bray, O Gileadi, S Knapp, U Oppermann, C Arrowsmith, R Hui, J Ming, S dhe Paganon, H W Park, A Savchenko, A Yee, A Edwards, R Vincentelli, C Cambillau, R Kim, S H Kim, Z Rao, Y Shi, T C Terwilliger, C Y Kim, L W Hung, G S Waldo, Y Peleg, S Albeck, T Unger, O Dym, J Prilusky, J L Sussman, R C Stevens, S A Lesley, I A Wilson, A Joachimiak, F Collart, I Dementieva, M I Donnelly, W H Eschenfeldt, Y Kim, L Stols, R Wu, M Zhou, S K Burley, J S Emtage, J M Sauder, D Thompson, K Bain, J Luz, T Gheyi, F Zhang, S Atwell, S C Almo,

J B Bonanno, A Fiser, S Swaminathan, F W Studier, M R Chance, A Sali, T B Acton, R Xiao, L Zhao, L C Ma, J F Hunt, L Tong, K Cunningham, M Inouye, S Anderson, H Janjua, R Shastry, C K Ho, D Wang, H Wang, M Jiang, G T Montelione, D I Stuart, R J Owens, S Daenke, A Schutz, U Heinemann, S Yokoyama, K Bussow, and K C Gunsalus. Protein production and purification. 5(2):135–146. doi: 10.1038/nmeth.f.202.

[210] D. W. A. Buchan and D. T. Jones. The PSIPRED protein analysis workbench: 20 years on. 47:W402–W407. doi: 10.1093/nar/gkz297.

[211] L. Goldschmidt, D. R. Cooper, Z. S. Derewenda, and D. Eisenberg. Toward rational protein crystallization: A web server for the design of crystallizable protein variants. 16(8):1569–76. doi: 10.1110/ps.072914007.

[212] L. Slabinski, L. Jaroszewski, L. Rychlewski, I. A. Wilson, S. A. Lesley, and A. Godzik. XtalPred: a web server for prediction of protein crystallizability. 23 (24):3403–5. doi: 10.1093/bioinformatics/btm477.

[213] K Katoh, J Rozewicki, and K D Yamada. MAFFT online service: multiple sequence alignment, interactive sequence choice and visualization. 20(4):1160–1166. doi: 10.1093/bib/bbx108.

[214] S. A. Combs, S. L. Deluca, S. H. Deluca, G. H. Lemmon, D. P. Nannemann, E. D. Nguyen, J. R. Willis, J. H. Sheehan, and J. Meiler. Small-molecule ligand docking into comparative models with rosetta. 8(7):1277–98. doi: 10.1038/nprot.2013.074.

[215] S. Lyskov and J. J. Gray. The RosettaDock server for local protein-protein docking. 36:W233–8. doi: 10.1093/nar/gkn216.

[216] E. Yamamoto, A. C. Kalli, K. Yasuoka, and M. S. P. Sansom. Interactions of pleckstrin homology domains with membranes: Adding back the bilayer via high-throughput molecular dynamics. 24(8):1421–1431. doi: 10.1016/j.str.2016.06.002.

[217] F. B. Naughton, A. C. Kalli, and M. S. P. Sansom. Modes of interaction of pleckstrin homology domains with membranes: Toward a computational biochemistry of membrane recognition. 430(3):372–388. doi: 10.1016/j.jmb.2017.12.011.

[218] E. Yamamoto. Computational and theoretical approaches for studies of a lipid recognition protein on biological membranes. 14:153–160. doi: 10.2142/biophysico.14.0153.

[219] S. DeLuca, K. Khar, and J. Meiler. Fully flexible docking of medium sized ligand libraries with RosettaLigand. 10(7):e0132508. doi: 10.1371/journal.pone.0132508.

[220] S. Kothiwale, J. L. Mendenhall, and J. Meiler. BCL::conf: small molecule conformational sampling using a knowledge based rotamer library. 7:47. doi: 10.1186/s13321-015-0095-1.

[221] M. A. Lomize, A. L. Lomize, I. D. Pogozheva, and H. I. Mosberg. OPM: orientations of proteins in membranes database. 22(5):623–5. doi: 10.1093/bioinformatics/btk023.

[222] E. L. Wu, X. Cheng, S. Jo, H. Rui, K. C. Song, E. M. Davila-Contreras, Y. Qi, J. Lee, V. Monje-Galvan, R. M. Venable, J. B. Klauda, and W. Im. CHARMM-GUI membrane builder toward realistic biological membrane simulations. 35(27): 1997–2004, . doi: 10.1002/jcc.23702.

[223] J. Lee, X. Cheng, J. M. Swails, M. S. Yeom, P. K. Eastman, J. A. Lemkul, S. Wei, J. Buckner, J. C. Jeong, Y. Qi, S. Jo, V. S. Pande, D. A. Case, C. L. Brooks, A. D. MacKerell, J. B. Klauda, and W. Im. CHARMM-GUI input generator for NAMD, GROMACS, AMBER, OpenMM, and CHARMM/OpenMM simulations using the CHARMM36 additive force field. 12(1):405–13. doi: 10.1021/acs.jctc.5b00935.

[224] S. Kim, J. Lee, S. Jo, C. L. Brooks, H. S. Lee, and W. Im. CHARMM-GUI ligand reader and modeler for CHARMM force field generation of small molecules. 38(21): 1879–1886. doi: 10.1002/jcc.24829.

[225] J. C. Phillips, R. Braun, W. Wang, J. Gumbart, E. Tajkhorshid, E. Villa, C. Chipot, R. D. Skeel, L. Kale, and K. Schulten. Scalable molecular dynamics with NAMD. 26(16):1781–802. doi: 10.1002/jcc.20289.

[226] A. Sethi, J. Eargle, A. A. Black, and Z. Luthey-Schulten. Dynamical networks in tRNA:protein complexes. 106(16):6620–5. doi: 10.1073/pnas.0810961106.

[227] P. Sormanni, F. A. Aprile, and M. Vendruscolo. The CamSol method of rational design of protein mutants with enhanced solubility. 427(2):478–90. doi: 10.1016/j.jmb.2014.09.026.

[228] Y. Liu and B. Kuhlman. RosettaDesign server for protein design. 34:W235–8. doi: 10.1093/nar/gkl163.

[229] K. E. Robertson, C. D. Truong, F. M. Craciunescu, J. H. Yang, P. L. Chiu, P. Fromme, and D. T. Hansen. Membrane directed expression in escherichia coli of BBA57 and other virulence factors from the lyme disease agent borrelia burgdorferi. 9(1):17606. doi: 10.1038/s41598-019-53830-x.

[230] N. J. Greenfield. Using circular dichroism spectra to estimate protein secondary structure. 1(6):2876–90, . doi: 10.1038/nprot.2006.202.

[231] A. Micsonai, F. Wien, L. Kernya, Y. H. Lee, Y. Goto, M. Refregiers, and J. Kardos. Accurate secondary structure prediction and fold recognition for circular dichroism spectroscopy. 112(24):E3095–103. doi: 10.1073/pnas.1500851112.

[232] C. Perez-Iratxeta and M. A. Andrade-Navarro. K2d2: estimation of protein secondary structure from circular dichroism spectra. 8:25. doi: 10.1186/1472-6807-8-25.

[233] A J Miles, S G Ramalli, and B A Wallace. DichroWeb, a website for calculating protein secondary structure from circular dichroism spectroscopic data. doi: 10.1002/pro.4153.

[234] L. Mavridis and R. W. Janes. PDB2cd: a web-based application for the generation of circular dichroism spectra from protein atomic coordinates. 33(1):56–63. doi: 10.1093/bioinformatics/btw554.

[235] J. Yang and Y. Zhang. Protein structure and function prediction using i-TASSER. 52:5 8 1–5 8 15. doi: 10.1002/0471250953.bi0508s52.

[236] D. T. Jones and D. Cozzetto. DISOPRED3: precise disordered region predictions with annotated protein-binding activity. 31(6):857–63. doi: 10.1093/bioinformatics/btu744.

[237] B. Ranjbar and P. Gill. Circular dichroism techniques: biomolecular and nanostructural analyses- a review. 74(2):101–20. doi: 10.1111/j.1747-0285.2009.00847.x.

[238] M. Hebditch and J. Warwicker. Web-based display of protein surface and pH-dependent properties for assessing the developability of biotherapeutics. 9(1):1969. doi: 10.1038/s41598-018-36950-8.

[239] P. Chan, R. A. Curtis, and J. Warwicker. Soluble expression of proteins correlates with a lack of positively-charged surface. 3:3333, . doi: 10.1038/srep03333.

[240] K. R. Abdul Azeez, S. Knapp, J. M. Fernandes, E. Klussmann, and J. M. Elkins. The crystal structure of the RhoA-AKAP-lbc DH-PH domain complex. 464(2):231–9. doi: 10.1042/BJ20140606.

[241] E. N. Kosobokova, K. A. Skrypnik, and V. S. Kosorukov. Overview of fusion tags for recombinant proteins. 81(3):187–200. doi: 10.1134/S0006297916030019.

[242] A. S. Pina, C. R. Lowe, and A. C. Roque. Challenges and opportunities in the purification of recombinant tagged proteins. 32(2):366–81. doi: 10.1016/j.biotechadv.2013.12.001.

[243] D. Esposito and D. K. Chatterjee. Enhancement of soluble protein expression through the use of fusion tags. 17(4):353–8. doi: 10.1016/j.copbio.2006.06.003.

[244] M. Lebendiker and T. Danieli. Production of prone-to-aggregate proteins. 588(2): 236–46. doi: 10.1016/j.febslet.2013.10.044.

[245] S. E. Bondos and A. Bicknell. Detection and prevention of protein aggregation before, during, and after purification. 316(2):223–31. doi: 10.1016/s0003-2697(03)00059-9.

[246] H. Chikumi, A. Barac, B. Behbahani, Y. Gao, H. Teramoto, Y. Zheng, and J. S. Gutkind. Homo- and hetero-oligomerization of PDZ-RhoGEF, LARG and p115rhogef by their c-terminal region regulates their in vivo rho GEF activity and transforming potential. 23(1):233–40. doi: 10.1038/sj.onc.1207012.

[247] J. I. Austerberry, A. Thistlethwaite, K. Fisher, A. P. Golovanov, A. Pluen, R. Esfandiary, C. F. van der Walle, J. Warwicker, J. P. Derrick, and R. Curtis. Arginine to lysine mutations increase the aggregation stability of a single-chain variable fragment through unfolded-state interactions. 58(32):3413–3421. doi: 10.1021/acs.biochem.9b00367.

[248] S. M. Garrard, K. L. Longenecker, M. E. Lewis, P. J. Sheffield, and Z. S. Derewenda. Expression, purification, and crystallization of the RGS-like domain from the rho nucleotide exchange factor, PDZ-RhoGEF, using the surface entropy reduction approach. 21(3):412–6. doi: 10.1006/prep.2001.1392.

[249] B. Zhang, Y. Zhang, Z. Wang, and Y. Zheng. The role of mg2+ cofactor in the guanine nucleotide exchange and GTP hydrolysis reactions of rho family GTP-binding proteins. 275(33):25299–307, . doi: 10.1074/jbc.M001027200.

[250] C. Wu, S. Agrawal, A. Vasanji, J. Drazba, S. Sarkaria, J. Xie, C. M. Welch, M. Liu, B. Anand-Apte, and A. Horowitz. Rab13-dependent trafficking of RhoA is required for directional migration and angiogenesis. 286(26):23511–20, . doi: 10.1074/jbc.M111.245209.

[251] G. E. Cozier, J. Carlton, D. Bouyoucef, and P. J. Cullen. Membrane targeting by pleckstrin homology domains. 282:49–88. doi: 10.1007/978-3-642-18805-33.

[252] S. Milhas, B. Raux, S. Betzi, C. Derviaux, P. Roche, A. Restouin, M. J. Basse, E. Rebuffet, A. Lugari, M. Badol, R. Kashyap, J. C. Lissitzky, C. Eydoux, V. Hamon, M. E. Gourdel, S. Combes, P. Zimmermann, M. Aurrand-Lions, T. Roux, C. Rogers, S. Muller, S. Knapp, E. Trinquet, Y. Collette, J. C. Guillemot, and X. Morelli. Protein-protein interaction inhibition (2p2i)-oriented chemical library accelerates hit discovery. 11(8):2140–8. doi: 10.1021/acschembio.6b00286.

[253] W. J. Nelson. Remodeling epithelial cell organization: transitions between front-rear and apical-basal polarity. 1(1):a000513. doi: 10.1101/cshperspect.a000513.

[254] L. D. Chong, A. Traynor-Kaplan, G. M. Bokoch, and M. A. Schwartz. The small GTP-binding protein rho regulates a phosphatidylinositol 4-phosphate 5-kinase in mammalian cells. 79(3):507–13. doi: 10.1016/0092-8674(94)90259-3.

[255] S W Chan, C J Lim, Y F Chong, A V Pobbati, C Huang, and W Hong. Hippo pathway-independent restriction of TAZ and YAP by angiomotin. 286(9): 7018–7026, . doi: 10.1074/jbc.C110.212621.

[256] J. L. Kam, K. Miura, T. R. Jackson, J. Gruschus, P. Roller, S. Stauffer, J. Clark, R. Aneja, and P. A. Randazzo. Phosphoinositide-dependent activation of the ADP-ribosylation factor GTPase-activating protein ASAP1. evidence for the pleckstrin homology domain functioning as an allosteric site. 275(13):9653–63. doi: 10.1074/jbc.275.13.9653.

[257] X. Jian, W. K. Tang, P. Zhai, N. S. Roy, R. Luo, J. M. Gruschus, M. E. Yohe, P. W. Chen, Y. Li, R. A. Byrd, D. Xia, and P. A. Randazzo. Molecular basis for cooperative binding of anionic phospholipids to the PH domain of the arf GAP ASAP1. 23(11): 1977–88, . doi: 10.1016/j.str.2015.08.008.

[258] X. Jian, P. Brown, P. Schuck, J. M. Gruschus, A. Balbo, J. E. Hinshaw, and P. A. Randazzo. Autoinhibition of arf GTPase-activating protein activity by the BAR domain in ASAP1. 284(3):1652–63, . doi: 10.1074/jbc.M804218200.

[259] N. J. Greenfield. Using circular dichroism collected as a function of temperature to determine the thermodynamics of protein unfolding and binding interactions. 1(6): 2527–35, . doi: 10.1038/nprot.2006.204.

[260] Cytoskeleton inc. GTP exchange factor (GEF) assays.

APPENDIX A

PERMISSIONS

Figure 1.1 reprinted from (Alexander T. Baker, Carmen Aguirre-Hernández, Gunnel Halldén, and Alan L. Parker. Designer Oncolytic Adenovirus: Coming of Age. Cancers, 10(6):201, June 2018. doi: 10.3390/cancers10060201. URL http://www.mdpi.com/2072-6694/10/6/201.) from MDPI under an open access CC BY license

Table 1.1 was adapted from (Brennetta J. Crenshaw, Leandra B. Jones, Courtnee' R. Bell, Sanjay Kumar, and Qiana L. Matthews. Perspective on adenoviruses: Epidemiology, pathogenicity, and gene therapy. 7(3):61. ISSN 2227-9059. doi: 10.3390/biomedicines7030061. URL https://www.mdpi.com/2227-9059/7/3/61.) from MDPI under an open access CC BY license

Figure 1.2 was adapted from (Jun Chang. Adenovirus vectors: Excellent tools for vaccine development. 21(1):e6. ISSN 1598-2629, 2092-6685. doi: 10.4110/in.2021.21.e6. URL https://immunenetwork.org/DOIx.php?id=10.4110/in.2021.21.e6.) from Immune Netw. under an open access CC BY-NC license

Figure 1.3 was adapted from (Urs F. Greber and Justin W. Flatt. Adenovirus entry: From infection to immunity. 6(1):177–197. ISSN 2327-056X, 2327-0578. doi: 10.1146/annurev-virology-092818-015550. URL https://www.annualreviews.org/doi/10.1146/annurev-virology-092818-015550.), with permission from Annual Review of Virology.

Figure 1.4 reprinted from (Tom Randall, Cedrick Sam, Andre Tartar, and Christopher Cannon. Covid-19 deals tracker: 9.6 billion doses under contract. URL https://www.bloomberg.com/graphics/covid-vaccine-tracker-global-distribution/contracts-purchasing-agreements.html.

Figure 1.5 adapted with permission from (Theodore E. Warkentin. Drug-induced immune-mediated thrombocytopenia — from purpura to thrombosis. 356(9):891–893. ISSN 0028-4793, 1533-4406. doi: 10.1056/NEJMp068309. URL http://www.nejm.org/doi/abs/10.1056/NEJMp068309.), Copyright Massachusetts Medical Society.

Figure 1.6A reprinted from (Eva Nogales and Sjors H.W. Scheres. Cryo-EM: A unique tool for the visualization of macromolecular complexity. 58(4):677–689. ISSN 10972765. doi: 10.1016/j.molcel.2015.02.019. URL https://linkinghub.elsevier.com/retrieve/pii/S1097276515001331.) with permission from Elsevier.

Figure 1.6B reprinted from (Rafael Fernandez-Leiro and Sjors H. W. Scheres. Unravelling biological macromolecules with cryo-electron microscopy. 537(7620):339–346. ISSN 0028-0836, 1476-4687. doi: 10.1038/nature19948. URL http://www.nature.com/articles/nature19948.) with permission from Macmillan Publishers Ltd.

Figure 1.7 reprinted from (K. L. Rossman, C. J. Der, and J. Sondek. GEF means go: turning on RHO GTPases with guanine nucleotide-exchange factors. 6(2):167–80. ISSN 1471-0072, 1471-0072. doi: 10.1038/nrm1587.) with permission from Macmillan Publishers Ltd.

Figure 1.8 adapted from (J. C. Dachsel, S. P. Ngok, L. J. Lewis-Tuffin, A. Kourtidis, R. Geyer, L. Johnston, R. Feathers, and P. Z. Anastasiadis. The rho guanine nucleotide exchange factor syx regulates the balance of dia and ROCK activities to promote polarized-cancer-cell migration. 33(24):4909–18. ISSN 1098-5549 0270-7306. doi: 10.1128/MCB.00565-13.), with permission from Molecular and Cellular Biology,

All published works were reproduced with the permission of all co-authors.